

Doctoral Dissertation

博士論文

**Generation of a p16 Reporter Mouse and Its Use to Characterize
and Target p16^{high} Cells *In Vivo***

(新規 p16 レポーターマウスを用いた生体内における p16 陽性細胞の一細胞解析)

A Dissertation Submitted for the Degree of Doctor of Philosophy

December 2022

令和 4 年 12 月 博士（理学）申請

Department of Biological Sciences, Graduate School of Science,

The University of Tokyo

東京大学大学院理学系研究科生物科学専攻

Satotaka Omori

大森 徳貴

Abstract

The cell is exposed to various stresses *in vivo*, and irreparable damage induces cellular senescence. Senescent cells express p16^{Ink4a} and exhibit an important characteristic, irreversible growth arrest. Recently, it is shown that senescent cells play a key role in age-associated organ dysfunction and lifespan. However, their involvement in pathological processes *in vivo* is still largely unknown. Here, I developed a p16-Cre^{ERT2}-tdTomato mouse model and examined the characteristics of p16^{high} cells *in vivo* at the single-cell level. It was found that p16^{high} cells are present in various organs and accumulate *in vivo* with aging. In addition, these cells did not proliferate and their half-life ranged from 2.6 to 4.2 months. I also performed single-cell transcriptomics analysis of the liver and kidney, which revealed that p16^{high} cells were found in various cell types and that these cells had a phenotype similar to senescent cells *in vitro*. In the liver, the dominant cell type was the liver sinusoidal endothelial cell and gene ontology analysis showed p16^{high} cells contributed to the chronic inflammatory microenvironment. Finally, the removal of p16^{high} cells ameliorated hepatic lipidosis and immune cell infiltration associated with nonalcoholic steatohepatitis. The new mouse model established in this study and the single-cell analysis enabled by this model may provide a powerful tool for uncovering previously unknown functions of senescent cells *in vivo*.

Table of contents

| | |
|---|----|
| Abstract..... | i |
| Table of contents..... | ii |
| Abbreviations | 1 |
| Chapter 1. Introduction | 3 |
| 1.1. Cellular senescence | 3 |
| 1.2. Senescent cells and aging..... | 4 |
| 1.3. p16 ^{Ink4a} reporter mouse model..... | 5 |
| 1.4. Aim of this research | 5 |
| Chapter 2. Materials and Methods..... | 7 |
| 2.1. Mouse Model..... | 7 |
| 2.2. MEF Experiments | 8 |
| 2.3. Virus Generation and Cell Infection..... | 8 |
| 2.4. SA- β -gal Staining..... | 9 |
| 2.5. Immunofluorescent Staining..... | 9 |
| 2.6. p16 ^{Ink4a} Antibody Production | 10 |

| | | |
|------------|---|----|
| 2.7. | Immunoblotting Analyses | 10 |
| 2.8. | Quantitative RT-PCR..... | 11 |
| 2.9. | Mouse Experiments | 12 |
| 2.10. | CUBIC Analysis..... | 13 |
| 2.11. | Histological Analysis..... | 13 |
| 2.12. | Tissue Dissociation and Flow Cytometry Analysis | 14 |
| 2.13. | Renal Cell Isolation for scRNA-seq Sample Preparation | 15 |
| 2.14. | Hepatic Non-parenchymal Cell Isolation for scRNA-seq Sample Preparation..... | 16 |
| 2.15. | Single-cell RNA Sequencing Data Analysis | 17 |
| 2.16. | Measurement of AST, ALT, and Hydroxyproline Levels | 18 |
| 2.17. | Statistics and Reproducibility | 19 |
| Chapter 3. | Results..... | 20 |
| 3.1. | Generation of a Mouse Model in which p16 ^{high} Cells Are Labeled with tdTomato | 20 |
| 3.2. | <i>In vivo</i> dynamics of p16 ^{high} cells in various tissues | 23 |
| 3.3. | scRNA-Seq of p16 ^{high} Cells in Normal Liver..... | 26 |

| | | |
|--|--|----|
| 3.4. | scRNA-Seq of p16 ^{high} Cells in NASH Liver..... | 30 |
| 3.5. | scRNA-Seq of p16 ^{high} Cells in Normal Kidney | 33 |
| 3.6. | Removal of p16 ^{high} Cells Ameliorates NASH-Induced Liver Steatosis and Inflammation..... | 36 |
| Chapter 4. Conclusion and Discussion | | 38 |
| Chapter 5. Figures and Tables | | 44 |
| Figure 1. | Mechanism of cellular senescence induction..... | 44 |
| Figure 2. | Senescent cells and aging..... | 45 |
| Figure 3. | Scheme of p16-Cre ^{ERT2} mice | 46 |
| Figure 4. | Scheme of p16-Cre ^{ERT2} -tdTomato mice | 47 |
| Figure 5. | Labeling efficiency in MEFs | 48 |
| Figure 6. | Immunostaining of MEFs | 49 |
| Figure 7. | SA-β-gal staining of MEFs..... | 50 |
| Figure 8. | Proportions of senescent cells marker positive cells in MEFs | 51 |
| Figure 9. | Validation of Ras-induced senescent MEFs | 52 |
| Figure 10. | Validation of Doxo-induced senescent MEFs | 53 |
| Figure 11. | Fluorescent imaging of senescent MEFs | 54 |

| | |
|--|-----------|
| Figure 12. Validation of Tom⁻ and Tom⁺ MEFs | 55 |
| Figure 13. Fluorescent image of p16-Cre^{ERT2}-tdTomato mice | 56 |
| Figure 14. Validation of Tom⁻ and Tom⁺ cells from p16-Cre^{ERT2}-tdTomato mice..... | 57 |
| Figure 15. Schematic representation of counting of Tom⁺ cell number..... | 58 |
| Figure 16. Validation of cluster formation in several organs | 59 |
| Figure 17. The number of Tom⁺ cells with aging by FACS..... | 60 |
| Figure 18. The number of Tom⁺ cells with aging by section analysis | 61 |
| Figure 19. Validation of turnover time in several organs | 62 |
| Figure 20. 3D fluorescent images in the lung | 63 |
| Figure 21. Clustering of normal liver cells..... | 64 |
| Figure 22. Composition of Tom⁺ cells in normal liver | 65 |
| Figure 23. Clustering of endothelial cells in normal liver..... | 66 |
| Figure 24. Validation of Tom⁺ and Tom⁻ LSECs in normal liver..... | 67 |
| Figure 25. Clustering of Kupffer cells in normal liver | 68 |
| Figure 26. Validation of Tom⁺ and Tom⁻ Kupffer cells in normal liver..... | 69 |

| | |
|---|-----------|
| Figure 27. Differential expression of marker genes in Kupffer cells | |
| subclusters | 70 |
| Figure 28. Clustering of Kupffer cells and LSECs merged | 71 |
| Figure 29. Pseudotime analysis of Kupffer cells and LSECs..... | 72 |
| Figure 30. Validation of NASH model..... | 73 |
| Figure 31. Clustering of NASH liver cells | 74 |
| Figure 32. Composition of Tom⁺ cells in NASH liver | 75 |
| Figure 33. Clustering of Macrophages in NASH liver..... | 76 |
| Figure 34. Validation of Tom⁺ and Tom⁻ Macrophages in NASH liver | 77 |
| Figure 35. Differential expression of marker genes in NASH liver Kupffer | |
| cells | 78 |
| Figure 36. Distribution of Tom⁺ Kupffer cells in NASH liver | 79 |
| Figure 37. Clustering of Kupffer cells and LSECs integrated with normal | |
| and Nash liver | 80 |
| Figure 38. Pseudotime analysis of Kupffer cells and LSECs integrated with | |
| normal and NASH liver | 81 |

| | |
|--|----|
| Figure 39. Pseudotime analysis of Kupffer cells integrated with normal and NASH liver data..... | 82 |
| Figure 40. Clustering of endothelial cells in NASH liver..... | 83 |
| Figure 41. Validation of Tom ⁺ and Tom ⁻ LSECs in NASH liver..... | 84 |
| Figure 42. Clustering of Kupffer cells in NASH liver | 85 |
| Figure 43. Clustering of kidney cells | 86 |
| Figure 44. Composition of Tom ⁺ cells in the kidney | 87 |
| Figure 45. Validation of Tom ⁺ and Tom ⁻ proximal tubular cells in the kidney..... | 88 |
| Figure 46. Validation of Tom ⁺ and Tom ⁻ distal tubular cells in the kidney . | 89 |
| Figure 47. Validation of Tom ⁺ and Tom ⁻ collecting duct cells in the kidney | 90 |
| Figure 48. Scheme of p16-Cre ^{ERT2} -DTR-tdTomato mice..... | 91 |
| Figure 49. Removal of Tom ⁺ cells in MEFs from p16-Cre ^{ERT2} -DTR-tdTomato mice <i>in vitro</i> | 92 |
| Figure 50. Inducing NASH model in p16-Cre ^{ERT2} -DTR-tdTomato mice | 93 |
| Figure 51. Validation of removal Tom ⁺ cells in p16-Cre ^{ERT2} -DTR-tdTomato mice | 94 |

| | |
|---|------------|
| Figure 52. Effect of removal p16^{high} cells in NASH model..... | 95 |
| Table 1. Top 10 genes upregulated in kidney Tom⁺ cells | 96 |
| Chapter 6. Reference | 97 |
| Acknowledgements..... | 109 |

Abbreviations

| | |
|---------|--|
| 4-OHT | 4-hydroxy tamoxifen |
| CDA-HFD | Choline-deficient L-amino acid, high-fat diet |
| CD-HFD | Choline-deficient, high-fat diet |
| CDK | cyclin-dependent kinase |
| CUBIC | Clear, unobstructed brain/body imaging cocktails and computational analysis |
| DEG | Differentially expressed gene |
| DMEM | Dulbecco's Modified Eagle Medium |
| DT | Diphtheria toxin |
| DTR | Diphtheria toxin receptor |
| Doxo | Doxorubicin |
| EC | Endothelial |
| Endo-pc | Pericentral endothelial cell |
| Endo-pp | Periportal endothelial cell |
| FACS | Fluorescence-activated cell sorting |
| FBS | Fetal bovine serum |
| GO | Gene ontology |
| GSEA | Gene Set Enrichment Analysis |

| | |
|------------------|---|
| LSEC | Liver sinusoidal endothelial cell |
| MEF | Mouse embryo fibroblast |
| NASH | Nonalcoholic steatohepatitis |
| NPC | Non-parenchymal cell |
| PBS | Phosphate-buffered saline |
| RISC | RNA-induced silencing complex |
| SA- β -gal | Senescence-associated beta-galactosidase |
| SASP | Senescence-associated secretory phenotype |
| scRNA-seq | Single-cell RNA sequencing |
| shRNA | short hairpin RNA |
| TAM | Tamoxifen |
| UMAP | Uniform manifold approximation and projection |
| UMI | unique molecular identifier |

Chapter 1. Introduction

1.1. Cellular senescence

Various studies have reported that senescent cells are closely implicated in aging and healthy life span (Childs et al., 2015; van Deursen, 2014; He and Sharpless, 2017). Senescence is induced in response to various genotoxic stresses, such as DNA damage, telomere shortening, oncogene activation, and oxidative stress (Figure 1) (Campisi and d'Adda di Fagagna, 2007; Collado et al., 2007; Kuilman et al., 2010). Senescent cells are characterized by irreversible growth arrest due to the expression of p16^{Ink4a}, a cell cycle arrest factor (Smith and Pereira-Smith, 1996), and p16^{Ink4a} is a well-known marker of senescent cells. p16^{INK4A} is a cyclin-dependent kinase (CDK) inhibitor molecule that blocks the binding of CDK4/6 to cyclin D. Thus, phosphorylation of RB by the cyclin D-CDK4/6 complex is inhibited, causing inhibition of the transcriptional regulator E2F by RB. As a result, the expression of genes involved in the transition from G1 to S phase, which is under the control of E2F, is suppressed and cell cycle progression is arrested. Also, senescent cells have been found to have a tumor-promoting aspect that non-autonomously forms a chronic inflammatory field in the surrounding tissue microenvironment via a specific property called senescence-associated secretory phenotypes (SASP) (Coppé et al., 2010), which secretes inflammatory cytokines and growth factors such as IL1, IL6, and IL8. In addition, senescent cells have other characteristics such as apoptosis resistance and mitochondrial

dysfunction (Correia-Melo and Passos, 2015; Fernandez-Marcos and Serrano, 2016). The analysis of these senescence-specific phenotypes has been performed primarily using *in vitro* culture systems because no suitable tools were enabling the identification and isolation of senescent cells *in vivo*.

1.2. Senescent cells and aging

So far, selective elimination of senescent cells (p16^{Ink4a}-positive cells) has been tried by a transgenic approach and drug administration and has been reported to extend the healthy lifespan and ameliorate various age-related disorders (Figure 2) (Aguayo-Mazzucato et al., 2019; Baar et al., 2017; Baker et al., 2011, 2016; Chang et al., 2016; Sessions et al., 2019; Xu et al., 2018; Yosef et al., 2016). This killing senescent cells approach is called senolysis. In particular, ameliorating previously untreatable diseases such as fibrosis and delaying progeria has also been reported. Also, the accumulation of senescent cells is found in age-related diseases from both mouse and human tissues and it is indicated that senescent cells are strongly associated with these diseases (Gorenne et al., 2006; Minamino and Komuro, 2007; Minamino et al., 2009; Tchkonina et al., 2010). Therefore, senescent cells seem to have an important role in triggering aging phenotypes and pathological conditions *in vivo*.

1.3. p16^{Ink4a} reporter mouse model

Although senescent cells have an important influence on aging, their localization in tissues, physiological function, and dynamics of them *in vivo* is still unclear. To visualize senescent cells *in vivo*, several mouse models have been generated. To analyze p16^{Ink4a}-positive senescent cells, mouse models were established in which the luciferase gene was knocked in at the endogenous mouse *Ink4a/Arf* locus (Burd et al., 2013) or inserted into a gene cassette containing a DNA segment from the human *Ink4a/Arf* locus (Yamakoshi et al., 2009). The following year, another group established p16-3MR mice (Demaria et al., 2014). This mouse model used BAC to insert into the genome a 3MR fusion gene that simultaneously expresses the Luciferase gene, the red fluorescent protein mRFP gene, and the herpes simplex virus-derived thymidine kinase gene in place of the second exon of the mouse *p16^{Ink4a}* gene. However, these mouse models using a luciferase reporter of *p16^{Ink4a}* expression are not suitable for characterizing the dynamics and features of p16^{Ink4a}-positive senescent cells *in vivo* at a single-cell level.

1.4. Aim of this research

In order to reveal the characteristics of senescent cells *in vivo*, analysis at the single-cell level is necessary. Single-cell RNA sequencing (scRNA-seq) is an optimal and very powerful tool for in-depth analysis of the genetic characteristics of different cell types in tissues (Grün

and van Oudenaarden, 2015; Kester and van Oudenaarden, 2018; Paolillo et al., 2019; Picelli, 2017; Stegle et al., 2015). However, since the *Ink4a* locus encodes p16^{Ink4a} and p19^{Arf}, it is difficult to detect the expression of the *p16^{Ink4a}* gene alone by scRNA-seq (Quelle et al., 1995). Therefore, a system that can report only the expression of *p16^{Ink4a}* is needed. Recently, two mouse models have been generated that monitor endogenous *p16^{Ink4a}* expression using a fluorescent protein as a reporter (Grosse et al., 2020; Liu et al., 2019). Nevertheless, due to the low efficiency of labeling caused by the weak expression of *p16^{Ink4a}*, the dynamics of senescent cells and their transcriptomics *in vivo* at the single-cell level have not yet been analyzed. In this study, I generated a mouse model in which *Cre^{ERT2}* was inserted at the endogenous *Ink4a* locus and crossed these mice with Rosa26-CAG-lsl-tdTomato mice (p16-*Cre^{ERT2}*-tdTomato mice) to establish a mouse model in which p16^{Ink4a}-positive senescent cells can be visualized at the single cell level. Using this new mouse tool, I showed that p16^{Ink4a}-positive senescent cells *in vivo* have the characteristics of previously known *in vitro* senescent cells. In addition, this mouse can be labeled at the single-cell level, making it possible to perform scRNA-seq. As a result of my analysis, I found that *in vivo* p16^{Ink4a}-positive senescent cells exhibit a high degree of cell type-specific heterogeneity.

Chapter 2. Materials and Methods

2.1. Mouse Model

The mice were housed in a temperature-controlled colony room (23-25°C) and humidity-controlled environment, with a 12-h light/dark cycle (08:00 to 20:00 light on), standard food (CA-1, CLEA Japan) and water provided ad libitum, as well as environmental enrichments.

All animal handling was conducted in accordance with the Guidelines for Animal Experiments of the Institute of Medical Science, the University of Tokyo, and the Institutional Laboratory Animal Care. The p16^{Ink4a}-Cre^{ERT2} mice were generated via homologous recombination in C57BL/6 embryonic stem cells, utilizing a targeting vector in which the firefly luciferase gene cassette was replaced by a Cre^{ERT2} gene cassette, as previously reported by Burd et al. (2013) (kindly provided by Dr. CE Burd and Dr. NE Sharpless, University of North Carolina). Germline transmission was confirmed, and the mice were maintained with C57BL/6 for further analysis unless otherwise described. The p16-Cre^{ERT2}-tdTomato mice were generated by crossing p16^{Ink4a}-Cre^{ERT2} mice with Rosa26-CAG-lsl-tdTomato mice (Jackson's Laboratory). p16-Cre^{ERT2}-DTR-tdTomato mice were generated by crossing p16^{Ink4a}-Cre^{ERT2} mice with Rosa26-SA-lsl-DTR-IRES-tdTomato mice (Iwasaki et al., 2018). In all experimental groups, age-matched and same-strain mice were used, as a result of in-house mating.

2.2. MEF Experiments

Embryos were dissected from the uterus and extraembryonic membranes between days E13.5 and E14.5. Following the dissection of the head and visceral organs for genotyping, the embryos were minced into pieces, trypsinized for 15 minutes at 37°C, and then rinsed with Dulbecco's Modified Eagle Medium (DMEM) supplemented with 10% Fetal Bovine Serum (FBS). The resulting cell aggregates were resuspended by pipetting, placed on culture dishes, and maintained in DMEM with 10% FBS for further experimentation. To induce DNA damage-induced senescence, cells were treated with 100 nM of Doxorubicin (Sigma) for 24 hours and then cultured in normal media for 10 days. Oncogene-induced senescent cells were generated by the expression of H-RAS^{Val12} for 10 days. Replicative senescent cells were generated by serial passages (P8). To label tdTomato, cells were treated with 4-Hydroxytamoxifen (4-OHT) at a concentration of 500 nM at the indicated time points.

2.3. Virus Generation and Cell Infection

The generation of lentiviruses and their subsequent infection of cells were performed as previously described (Johmura et al., 2014). Lentiviruses expressing *H-RAS^{Val12}* or the respective short hairpin RNAs (shRNAs) were generated by co-transfecting 293T cells with pCMV-VSV-G-RSV-RevB, pCAG-HIVgp, and the respective CS-RfA-ETBsd, CSII-CMV-H-

RASVal12-IRES2-Bsd, utilizing the calcium phosphate co-precipitation method. Cells infected with the indicated viruses were treated with 10 µg/mL of blasticidin for 2 days.

Luciferase shRNA target sequence: CGTACGCGGAATACTTCGA

mouse p16^{Ink4a} shRNA target sequence: GATTCAGGTGATGATGATGGG.

2.4. SA-β-gal Staining

The SA-β-gal staining protocol was executed in accordance with the method previously outlined by (Dimri et al., 1995). The cells were first rinsed with Phosphate-buffered saline (PBS) before being fixed for 5 minutes in a solution of 2% formaldehyde and 0.2% glutaraldehyde. They were then rinsed again and incubated at 37°C for 24 hours in a fresh stain solution consisting of 1 mg/mL X-gal, 40 mM citric acid/sodium phosphate at pH 6.0, 5 mM potassium ferrocyanide, 5 mM potassium ferricyanide, 150 mM NaCl, and 2 mM MgCl₂. Following the staining procedure, the cells were washed in PBS, fixed in methanol for 3 minutes, and rinsed one final time with PBS. Images were subsequently acquired using a BZ-9000 (Keyence).

2.5. Immunofluorescent Staining

For the purpose of fluorescence cytochemistry, cells that had been plated on coverslips or glass bottom dishes were fixed in 4% paraformaldehyde for a period of 10 minutes at room

temperature. Subsequently, the cells were permeabilized with 0.2% Triton X-100 in PBS for 5 minutes and incubated in a blocking buffer consisting of 5% Bovine serum albumin in PBS for 30 minutes. The samples were then incubated with lamin B1 rabbit antibody (1/100 dilution) at room temperature for 2 hours, followed by an additional incubation with anti-rabbit IgG conjugated with Alexa Fluor 488 (Life Technologies) secondary antibodies, which had been diluted in blocking buffer (1:200), for 1 hour at room temperature. The nuclei were counterstained with Hoechst 33342 (1:1000) before the images were acquired using a BZ-9000 (Keyence).

2.6. p16^{Ink4a} Antibody Production

Rabbits were immunized with a GST-tagged recombinant full-length mouse p16^{Ink4a} (Hokudo) in order to raise antibodies against mouse p16^{Ink4a}. The antisera were subsequently purified using an affinity purification technique, which employed FLAG-tagged p16^{Ink4a} immobilized with NHS-activated Sepharose 4 Fast Flow (GE Healthcare) and was used for subsequent immunoblotting analyses.

2.7. Immunoblotting Analyses

The immunoblotting analysis was conducted in accordance with the protocol previously described (Johmura et al., 2014). Whole cell lysates were obtained by directly lysing cells or

tissues with Laemmli buffer (2% SDS, 10% glycerol, 5% 2-mercaptoethanol, 0.002% bromophenol blue, and 62.5 mM Tris HCl at pH 6.8). The resulting whole cell lysates (20-50 μ g) were subsequently separated by SDS-PAGE, transferred to a PVDF (Immobilon-P; Millipore) membrane, and subjected to immunoblotting with the specified antibodies using an ECL detection system. β -actin antibody (C-4, Santa Cruz) was employed as a loading control. For Ruby staining, the gel was stained with Oriole Fluorescent Gel Stain (Bio-Rad) for 2 hours, and images were captured using a WSE-5400Printgraph Classic (ATTO) imaging system.

2.8. Quantitative RT-PCR

The quantitative RT-PCR assay was executed in accordance with the method previously outlined (Johmura et al., 2014). Total RNA was extracted from the samples using an RNeasy mini kit (QIAGEN) in accordance with the manufacturer's instructions. For qPCR analysis, cDNAs were synthesized using a ReverTra Ace qPCR RT kit (Toyobo). Real-time PCR amplifications were conducted in 96-well optical reaction plates with Power SYBR Green PCR Master Mix (Applied Biosystems). The relative expression levels of each gene were then calculated by normalizing to β -actin expression for each sample.

p16^{Ink4a} Forward primer: CCGCTGCAGACAGACTGG

p16^{Ink4a} Reverse primer: CCATCATCATCACCTGAATCG

Actb Forward primer: GGCTGTATTCCCCTCCATCG

Actb Reverse primer: CCAGTTGGTAACAATGCCATGT

2.9. Mouse Experiments

All p16-Cre^{ERT2}-tdTomato mice were sacrificed two weeks after the daily intraperitoneal injection with tamoxifen (TAM, 80 mg/kg body weight) for a period of five days at the designated time point, with the exception of the turnover experiment. For the turnover experiment, 10-week-old mice were labeled with tdTomato using TAM and sacrificed after either 2 or 14 weeks. The scRNA-seq sample for the NASH induction study was obtained from 6-week-old mice that had been maintained on a rodent diet with 45% kilocalories from fat, and without added choline (CD-HFD: D05010402, Research Diets) for 6 months. In order to eliminate p16^{high} cells in the NASH model, 6-week-old p16-Cre^{ERT2}-DTR-tdTomato mice were maintained on an L-amino acid diet with 60% kilocalories from fat, with 0.1% methionine and no added choline (CDA-HFD: A06071302, Research Diets) for 6 weeks. After 3 weeks of feeding, mice were intraperitoneally injected with TAM (80 mg/kg body weight) with vehicle control (equal volume of PBS) or diphtheria toxin (DT, 25 ug/kg body weight) on seven occasions over a 3-week period, and the organs were subsequently collected for further experimentation.

2.10. CUBIC Analysis

p16-Cre^{ERT2}-tdTomato mice were euthanized by means of an overdose of avertin and perfused with a solution of 20 mL of PBS and 30 mL of 4% (w/v) PFA in PBS via the left ventricle of the heart. The lung tissue was then post-fixed in 4% (w/v) PFA in PBS at 4°C for 24 hours, in accordance with the CUBIC organ clearing protocol as previously described (Matsumoto et al., 2019; Susaki et al., 2014; Tainaka et al., 2018). The lung tissue was subsequently stained with RedDot2 (40061, Biotium) and FITC-conjugated anti- α -SMA antibody (F3777, Sigma-Aldrich) for a period of 3 days at room temperature with shaking. The samples were then imaged using a light-sheet fluorescence microscope (MVX-ZB10, Olympus, Japan) equipped with an Olympus MVPLAPO 0.63 \times lens (Kubota et al., 2017; Tainaka et al., 2018), and the images were visualized with Imaris software (version 9.2.1, Bitplane).

2.11. Histological Analysis

To perform immunofluorescent staining, the kidney, lung, liver, heart, brain, intestine, and colon samples were preserved in OCT compound and subsequently cryo-sectioned. DAPI staining was performed to visualize the nuclei. Anti-RFP (Abcam, ab124754) staining was employed to detect the expression of tdTomato due to the low fluorescent signals observed in the p16-Cre^{ERT2}-DTR-tdTomato mice used in the experiments. The IN Cell Analyzer

2500HS (GE Healthcare) was utilized to acquire images of the fluorescent signals and to automatically count Tom⁺ cells and calculate the percentage for each field by recognizing DAPI signals as nuclei and Tom⁺ signals that were 10-fold greater than the background. To determine the presence of Tom⁺ cell clusters in the kidney, lung, and liver sections, the fields were first partitioned into 25x squares of the average area of targeted Tom⁺ cells and then the cell number in each square was calculated. To prevent cell composition bias, fields located in the renal cortex region of the kidney sections were primarily selected. Fields of other organ sections were randomly selected. For the purpose of immunohistochemical staining, the liver was fixed in paraffin, sectioned, and stained with H&E and anti-F4/80 (CST, D2S9R XP) using conventional immunostaining procedures and DAB (DAKO). The stained tissue sections were observed under bright-field illumination using a BZ-9000 analyzer (Keyence). To quantify the F4/80⁺ signals and the adipose content in the liver, the F4/80⁺ area and the lipid droplet area were measured in 10 fields for each sample using ImageJ software. Sirius red/Fast green FCF staining was performed according to a standard protocol (Kamimoto et al., 2020).

2.12. Tissue Dissociation and Flow Cytometry Analysis

Organs were initially minced with a sharp blade and subsequently underwent a digestion process. The liver was incubated in an HBSS solution containing 10 mM HEPES, 1 mg/mL

collagenase IV (GIBCO, 9001-12-1), 1 mg/mL pronase (Sigma, 359643001), and 12.5 kU DNase (Sigma, D4263) at 37°C for 30 minutes. The skin was incubated in a DMEM solution containing 1 mg/mL collagenase IV (GIBCO, 9001-12-1) and 12.5 kU DNase (Sigma, D4263) at 37°C for 90 minutes. The lung was incubated in RPMI1640 containing 10% FBS, 10 mM HEPES, 0.25 mg/mL Liberase TM (Roche 5401119001), and 2 kU DNase (sigma, D4263) at 37°C for 60 minutes. The kidney was incubated in RPMI1640 containing 10% FBS, 10mM HEPES, 0.25 mg/mL Liberase TH (Roche 5401135001), and 2 kU DNase (Sigma, D4263) at 37°C for 60 minutes. Following the incubation period, the cells were filtered through a 70 µm cell strainer and lysed in an ACK lysis buffer (150 mM NH₄Cl, 10 mM KHCO₃, 0.1 mM EDTA, pH7.3) at room temperature for 3 minutes, and subsequently washed with a wash buffer consisting of 4% FBS in PBS. The cells were then treated with an FcR blocking reagent, mouse (MACS), at 4°C for 10 minutes, stained with fluorescence-labeled CD45 antibody or isotype control at 4°C for 30 minutes, washed, and subsequently analyzed/sorted using a FACS Aria II (BD Biosciences) instrument.

2.13. Renal Cell Isolation for scRNA-seq Sample Preparation

The kidney tissue was minced with a sharp blade and further digested with a solution containing DMEM, 0.05 mg/mL Liberase DH (Roche, 5401054001), 2 mg/mL Collagenase IV (GIBCO, 9001-12-1), and 25 kU/mL DNase (Sigma, D4263) at 37°C for 60 minutes. After the

incubation period, the samples were washed with PBS containing 4% FBS and filtered through a 70 μ m cell strainer. The renal cells were then lysed of red blood cells with ACK buffer and subsequently treated with a mouse FcR blocking reagent (MACS, 130-092-575), before being stained with anti-mouse CD45-conjugated PerCP/Cy5.5 (Biolegend, 103131) in PBS containing 4% FBS. The renal cells were sorted using FACS Aria II (BD Bioscience) and their viability was confirmed through trypan blue staining.

2.14. Hepatic Non-parenchymal Cell Isolation for scRNA-seq Sample Preparation

To isolate the hepatic non-parenchymal cells (NPCs), a perfusion protocol was employed in which the liver was first perfused with pre-warmed calcium-free Hank's Balanced Salt Solution (HBSS) containing 0.5 mM EGTA and 10 mM HEPES. This was followed by a second perfusion with HBSS containing 0.5 mg/mL Collagenase D (Sigma, 11088866001) and 10 mM HEPES. The liver was then minced and passed through a 70 μ m cell strainer. The hepatic cell suspension was subsequently centrifuged at 50 g for 2 minutes to remove any remaining hepatocytes. After lysing red blood cells with ACK buffer, the NPCs were re-suspended in PBS containing 4% FBS and sorted using a FACS Aria II (BD Bioscience) instrument. The viability of the cells was confirmed by performing trypan blue staining.

2.15. Single-cell RNA Sequencing Data Analysis

The construction of the scRNA-seq library was accomplished using the 10 X Genomics Chromium Single Cell 3' Reagent Kit v3. The single-cell suspension, which was either comprised of non-separated cells or Tom⁺ cells, was obtained from liver and kidney samples of 7- or 5-month-old p16-Cre^{ERT2}-tdTomato mice that were maintained on either a normal diet or a NASH-induced diet. The libraries were then sequenced using the Illumina Novaseq 6000 system (Novogene) and resulted in approximately 600 million and 300 million reads for the kidney and liver samples, respectively. The sequence alignment process involved the recognition of unique molecular identifiers (UMIs) and barcodes, and the mapping of transcripts to a mm10 mouse reference genome via the Cell Ranger package (ver. 3.0.2). The Seurat package (ver. 4.0) on R (ver. 4.1.0) was utilized to process the single-cell RNAseq data (Hao et al., 2021). After eliminating cells of low sequencing quality (> 200 genes and > 800 UMI counts), cells with high levels of mitochondria (40%< for kidney and 10%< for liver), and doublet cells, a total of 3,042 and 11,448 kidney and liver cells, respectively, and 17,000 genes were available for further analysis. The UMI counts were normalized per cell after excluding highly expressed genes, and then log-transformed by computing $X = \log(X+1)$. The data visualization process employed the use of the Uniform Manifold Approximation and Projection (UMAP) method for dimensional reduction of the top 2,000 highly variable genes (McInnes et al., 2018). Following graph-based clustering

using the Leiden algorithm at resolution 2, the top 100 rank genes for each cluster were identified through the logistic regression method. The cell type of each cluster was further characterized based on the fitness between the rank genes and the cell type marker gene list provided by previous studies (Ransick et al., 2019; Xiong et al., 2019). The Kupffer cells were further recognized by Kupffer cell core genes (Cd5l and Clec4f) from macrophages in liver samples (Bonnardel et al., 2019). After graph-based clustering, the cell type of each cluster was characterized based on the marker genes previously described (Ransick et al., 2019; Xiong et al., 2019). Differentially expressed genes (DEGs) were defined as genes that had an FDR less than 0.05 and a log2-fold change greater than 0.1. To describe the network connectivity and relationship between Kupffer cells and LSECs, the Monocle 3 package was utilized to visualize and calculate the pseudotime (Cao et al., 2019).

2.16. Measurement of AST, ALT, and Hydroxyproline Levels

Blood was procured from the mice and allowed to sit at room temperature for a period of 30 minutes. In order to obtain serum, the samples were centrifuged at 4,000 revolutions per minute for 5 minutes at 4°C. The levels of AST and ALT in the serum were subsequently determined by utilizing AST Activity Assay Kit (FUJIFILM) and ALT Activity Assay Kit (FUJIFILM), respectively. The amount of hydroxyproline present in the liver was measured by using a Hydroxyproline Assay Kit (Abcam) according to the manufacturer's instructions.

2.17. Statistics and Reproducibility

In the animal experimentation, all mice of the same genotype were randomly assigned to each group, without a predetermined sample size through pilot studies. A blinded design was not implemented in this study due to the utilization of an image analyzer for automatic analysis utilizing the same criteria. Mice displaying a notably lower Cre recombination efficiency (less than 10% in comparison to the average) were excluded, with an approximate exclusion rate of 15%. The normality of the population distributions at the 0.05 level was determined using the Shapiro-Wilk normality test. Data is presented as means \pm SD unless otherwise specified. Comparisons between the two groups were performed through an unpaired two-tailed Student's t-test. Multi-comparisons were carried out through a one-way analysis of variance (ANOVA) following Tukey's posthoc test. To maintain consistency in comparisons, significance in all figures is denoted as follows: * $p < 0.05$, ** $p < 0.01$, *** $p < 0.001$, **** $p < 0.0001$. Representations of all findings were the result of triplicate experiments, which yielded similar results.

Chapter 3. Results

3.1. Generation of a Mouse Model in which p16^{high} Cells Are Labeled with tdTomato

In order to gain a comprehensive understanding of the *in vivo* dynamics of senescent cells at a single-cell level, I employed the p16^{Ink4a}-luciferase model (Burd et al., 2013) and utilized a Cre^{ERT2} system to regulate Cre activity. The Cre^{ERT2} system allows for the determination of not only the half-life of labeled cells, but also their long-term proliferative potential *in vivo*. Through the evaluation of various Cre-containing cassette genes, I discovered that the integration of a Cre^{ERT2} and a neo-resistant gene resulted in a significantly higher labeling efficacy in the *Ink4a* locus, as previously reported by Liu et al. (2019). This is likely due to the neo-resistant cassette acting as a local enhancer to augment reporter expression without compromising tissue reporter fidelity (Scarff et al., 2003; Schmidt-Supprian et al., 2007). Initially, I generated p16^{Ink4a}-Cre^{ERT2}neo (p16-Cre^{ERT2}) mice in which the endogenous *p16^{Ink4a}* gene's first exon was replaced with a Cre^{ERT2} and a neo-resistant gene (Figure 3). Subsequently, the p16-Cre^{ERT2} mice were intercrossed with the Rosa26-CAG-lsl-tdTomato line, resulting in p16^{Ink4a}-Cre^{ERT2}neo-tdTomato (p16-Cre^{ERT2}-tdTomato) mice, which facilitate the specific labeling of p16^{high} cells with tdTomato in the presence of Tamoxifen (TAM) (Figure 4).

The induction of senescence in mouse embryo fibroblasts (MEFs) from p16-Cre^{ERT2}-tdTomato mice was achieved via replicative stress. Elevated expression of the p16^{Ink4a} protein was observed in senescent cells (Figure 5A). Upon incubation with 4-hydroxy tamoxifen (4-OHT) for a period of three days, a significant proportion of senescent cells were labeled with tdTomato (tdTomato positive: Tom⁺) (Figure 5B). To verify the induction of senescence, co-staining with lamin B1 and senescence-associated beta-galactosidase (SA- β -gal) was performed (Figures 6 and 7). The loss of lamin B1 and the presence of SA- β -gal activity are widely accepted biomarkers of senescence (Freund et al., 2012; Dimri et al., 2012). A significant increase in the proportion of lamin B1-negative and SA- β -gal-positive cells was observed in replicative senescent MEFs, and nearly all Tom⁺ cells were found to be lamin B1-negative and SA- β -gal-positive (Figure 8). Similar results were obtained when MEFs underwent senescence through oncogene activation or DNA damage with Doxorubicin (Doxo) (Figures 9 and 10).

It is important to note that the level of tdTomato expression does not necessarily correspond to the intrinsic expression of p16^{Ink4a}, as it can indicate varying degrees of labeling. In order to gain a more accurate understanding of the level of p16^{Ink4a} expression in Tom⁺ cells, I employed mouse embryo fibroblasts (MEFs) from p16-Cre^{ERT2}-tdTomato mice that underwent DNA damage-induced senescence via Doxorubicin (Doxo) treatment and

incubated them with 4-OHT for a period of 12 days to fully activate Cre. The resultant cells were then sorted according to the tdTomato intensity (Figures 11 and 12A), and the levels of $p16^{Ink4a}$ mRNA and protein were determined in both Tom⁺ and Tom⁻ cells (Figure 12B). Doxo-treated Tom⁻ and Tom⁺ cells expressed 4-fold and near 8-fold higher $p16^{Ink4a}$ mRNA levels, respectively, compared to Doxo-untreated cells (Figure 12B). The protein p16^{Ink4a} level of Doxo-treated Tom⁺ cells was also found to be increased compared to Tom⁻ (Figure 2.10B). Despite the fact that the labeling efficiency of senescent cells with tdTomato does not appear to be 100%, Tom⁺ cells were found to be near 100% senescent cells (SA- β -gal-positive and lamin B1-negative) *in vitro* (Figure 8), thereby avoiding false-positive labeling. These results suggest that cells with high p16^{Ink4a} expression can be accurately labeled in p16-Cre^{ERT2}-tdTomato mice.

3.2. *In vivo* dynamics of p16^{high} cells in various tissues

Subsequently, I conducted an investigation into the distribution of cells with high levels of p16^{Ink4a} expression in various tissues of 7-month-old mice. Through the use of histological sections, I identified Tom⁺ cells in all tissues examined (Figure 13). Furthermore, Tom⁺ cells were also detected through fluorescence-activated cell sorting (FACS) in the kidney, lung, and liver (Figure 14). The cells were stratified according to the intensity of tdTomato expression, and the level of p16^{Ink4a} protein was quantified in both Tom⁺ and Tom⁻ cells. The p16^{Ink4a} protein was only detected in Tom⁺⁺ cells (Figure 14).

In order to evaluate the long-term proliferative potential of p16^{high} cells, I first labeled these cells in 10-week-old mice through TAM treatment for a period of 5 days and then analyzed them at 2 and 14 weeks post-treatment. As previous cell tracing experiments have demonstrated that proliferating cells tend to congregate in tissue clusters (Boone et al., 2019; El-Nachef et al., 2020; Ueno and Weissman, 2006), I examined whether p16^{high} cells formed clusters in the kidney, lung, and liver. To accomplish this, I partitioned all fields into squares with an average area 25-fold larger than that of a targeted single Tom⁺ cell and then calculated the number of Tom⁺ cells within each square (Figure 15). The distribution of cell numbers in each square of mouse tissues 2 and 14 weeks after TAM treatment was found to be nearly identical (Figure 16), suggesting that p16^{high} cells did not form a

proliferative cell cluster during this experimental period.

I sought to investigate the correlation between aging and the number of p16^{high} cells in various tissues. To accomplish this, I labeled p16^{high} cells in 2-month-old and 12-month-old mice (the latter being early middle-aged mice) with tdTomato and quantified the number of labeled cells using FACS. I observed a significantly higher number of Tom⁺ cells in the kidney, lung, liver, and skin of 12-month-old mice compared to 2-month-old mice (Figure 17). Furthermore, I determined the number of labeled cells in sections of the kidney, lung, and liver collected at five different time points, 3, 6, 9-12, 15-18, and 21-24 months old. The number of Tom⁺ cells increased with age in all organs, with the peak time-varying for each organ (Figure 18). These results are consistent with previous findings using p16^{Ink4a}-luciferase models (Burd et al., 2013; Yamakoshi et al., 2009).

I sought to determine the half-life of p16^{high} cells *in vivo* by administering TAM to 10-week-old mice and analyzing the tissues at 2 or 14 weeks post-treatment. My analysis revealed that the number of Tom⁺ cells was notably lower after 14 weeks of TAM administration as compared to 2 weeks. The half-life was calculated to be 2.9 months in the kidneys, 4.2 months in the lungs, and 2.6 months in the liver (Figure 19).

I employed a 3-dimensional imaging technique utilizing the Clear, Unobstructed Brain/Body Imaging Cocktails and Computational Analysis (CUBIC) system, a highly effective tissue-clearing method (Susaki et al., 2014; Tainaka et al., 2018) to visualize the distribution of p16^{high} cells in the lungs. The analysis revealed that Tom⁺ cells were primarily located in the hilum of the lung in a 2-month-old mouse, while significantly increased numbers of Tom⁺ cells were distributed throughout all regions of the lung in a 10-month-old mouse (Figure 20).

3.3. scRNA-Seq of p16^{high} Cells in Normal Liver

The senescence of non-parenchymal cells (NPCs) has been implicated in the etiology of chronic liver diseases (Aravinthan and Alexander, 2016). As such, I carried out a mapping and characterization of p16^{high} cells in normal NPCs at the single-cell level. To minimize enzymatic damage to senescent cells, a mild, short-term digestion with collagenase alone was employed to separate liver tissue into single cells, which presumably resulted in a relatively high proportion of endothelial cells among the total NPCs (Figure 21) (Xiong et al., 2019). Two distinct cell sorting approaches were utilized to perform single-cell RNA sequencing (scRNA-seq) of NPCs. In order to evaluate the Tom⁺ population size in each cell type, non-separated cells were directly collected. However, since the *in vivo* conditions yielded only an extremely low proportion of senescent cells, Tom⁺ cells were also sorted to enrich the cell number for further analyses.

I obtained a total of 4,387 single-cell transcriptomes from the p16-Cre^{ERT2}-tdTomato mouse, comprising 1,859 cells from the non-separated sample and 2,528 cells from the Tom⁺ sorted sample. Through unsupervised graph-based clustering, cell types were identified based on the pattern fitness between the top 100 cluster rank genes and a cell-type gene list from a previously reported scRNA-seq dataset (Figure 21A) (Xiong et al., 2019) utilizing uniform manifold approximation and projection (UMAP). Representative genes of each type in the

violin plot were also matched with previous studies (Figure 21B) (Bäumer et al., 2006; Bonnardel et al., 2019; Clausen et al., 1999; Faure-André et al., 2008; Scholzen and Gerdes, 2000; Xiong et al., 2019). Tom⁺ cells were dispersed in each cell type with the exception of Cholangiocyte (Figure 22). Based on the expression level of marker genes (Rspo3 and Adgrg6), endothelial cell types were further classified into three subtypes, including pericentral (Endo-pc), periportal (Endo-pp), and liver sinusoidal endothelial cell (LSEC) (Figure 23). The actual numbers of Tom⁺ cells in each endothelial subtype from the non-separated sample were 3/47 (Endo-pc), 4/21 (Endo-pp), and 77/1359 (LSEC). Differentially expressed genes (DEGs) analysis revealed that 47 genes were upregulated and 25 genes were downregulated in Tom⁺ compared to Tom⁻ LSECs (Figure 24A). Gene ontology (GO) analysis indicated that protein catalytic-related terms were enriched in the downregulated genes of Tom⁺ LSECs, suggesting proteolytic dysfunction, as previously described in the aging liver (Figure 24B) (Marongiu et al., 2016).

My scRNA-seq analysis revealed the identification of Kupffer cells as two distinct, previously uncharacterized clusters, with the majority of Tom⁺ cells found in one of them (Figure 25). Through differential expression gene (DEG) analysis, I identified 231 genes that were upregulated and 316 genes that were downregulated in Tom⁺ cells compared to Tom⁻ Kupffer cells (Figure 26A). Additionally, Tom⁺ cells displayed increased resistance to

apoptosis, a characteristic commonly associated with cellular senescence properties (Figure 26B). Furthermore, a positive correlation was observed between Tom⁺ cells and an endothelial cell phenotype, and a loss of immune cell identity was also noted (Figure 26B), a phenomenon previously reported in aged tissue-resident macrophages (Oishi and Manabe, 2016; Solana et al., 2012).

Subsequently, I focused on identifying the distinctions between the two clusters of Kupffer cells. The Tom⁺-predominant Kupffer cluster exhibited expression of typical LSEC markers (Ptprb, Eng, Igfbp7, Clec4g, Kdr) as well as markers specific to Kupffer cells (C1qc, C1qb, Ctss, C1qa, Cd5l), albeit at lower levels than those observed in classical Kupffer cells (Figure 27A). Gene Set Enrichment Analysis (GSEA) also revealed that the Tom⁺-predominant Kupffer cluster possessed more LSEC signatures and lacked Kupffer cell signatures in comparison to classical Kupffer cells (Figure 27B). As such, I provisionally classified the Tom⁺-predominant Kupffer cluster as an endothelial-like Kupffer cell (EC-like Kupffer cell) and partitioned it into two subtypes - classical Kupffer cells and EC-like Kupffer cells - for further differential gene comparisons.

The transcriptomic state of EC-like Kupffer cells was found to be intermediate between that of traditional Kupffer cells and liver sinusoidal endothelial cells (LSECs)

(Figure 28). In order to establish the relationship network of EC-like Kupffer cells, a trajectory analysis was conducted to demonstrate the connectivity strength (Cao et al., 2019). When LSECs were designated as the starting point, the pseudotime analysis revealed that the transcriptome of the EC-like Kupffer cells was situated between Kupffer cells and LSECs, and closer to Kupffer cells (Figure 29).

3.4. scRNA-Seq of p16^{high} Cells in NASH Liver

The association between cellular senescence and hepatic steatosis *in vivo* remains uncertain, despite the presence of indications of a mutual relationship (Ogrodnik et al., 2017; Papatheodoridi et al., 2020). In order to obtain a more comprehensive understanding of this relationship at the single-cell level, I performed the scRNA-seq analysis of the liver from nonalcoholic steatohepatitis (NASH) mouse model induced by a 6-month feeding regimen of a choline-deficient, high-fat diet (CD-HFD) (Wolf et al., 2014) (Figure 30).

I obtained 7,061 cells from the liver of a mouse with NASH, and ten cell types were identified as normal liver (Figure 31). A markedly higher number of macrophages was observed in the liver of the NASH mouse as compared to the liver of a healthy mouse (Figure 31A) and a greater number of Tom⁺ cells were detected in other cell types than endothelial cells (Figures 22 and 32) (Kazankov et al., 2019).

The macrophage fraction was classified into two clusters, with Tom⁺ cells primarily concentrated within one cluster (Figure 33), similar to the Kupffer cells fraction of the normal liver (Figure 25). Gene ontology analysis revealed an enrichment of genes related to response to cytokines and cytokine production in upregulated genes in Tom⁺ macrophages, which have been implicated in the progression of steatohepatitis (Figure 34) (Zhang et al.,

2019). Furthermore, resistance to apoptosis was found to be augmented (Figure 34).

EC-like Kupffer cells were also identified in the NASH sample (Figure 35). I observed a higher proportion of Tom⁺ cells in NASH-induced Kupffer cells as compared to normal Kupffer cells (Figures 25 and 36). In order to establish the transcriptomic relationship between Kupffer cells, EC-like Kupffer cells, and LSECs, the merging of normal and NASH samples was employed to explore the effects of NASH induction (Figure 37A). As in a normal liver, the EC-like Kupffer cells in the liver of the NASH mouse expressed both Kupffer and LSEC markers (Figure 37B). In the trajectory inference, EC-like Kupffer cells exhibited stronger connectivity to Kupffer cells than to LSECs (Figure 38).

In order to clarify the effects of NASH on Kupffer cells, I also merged the Kupffer cells and endothelial-like Kupffer cells of normal and NASH samples (Figure 39A). Trajectory analysis revealed that the position of NASH-induced Kupffer cells migrated toward the endothelial-like Kupffer cells (Figures 39B and 39C), which supports my hypothesis regarding the normal liver in which the immune cell identity of Tom⁺ Kupffer cells was compromised.

The endothelial cells present in the liver of the NASH mouse were classified into three

subtypes: Endo-pc, Endo-pp, and LSEC (Figure 40). The actual numbers of Tom⁺ cells in each endothelial subtype from the non-separated sorted NASH sample were 12/146 (Endo-pc), 19/74 (Endo-pp), and 337/2922 (LSEC). The Tom⁺ population was observed to be higher in NASH LSECs when compared to that of normal LSECs. These cells could be characterized by their higher mitochondrial activity, which has been associated with cellular senescence properties (Figure 41) (Kaplon et al., 2013). The defective neutrophil aggregation phenotype might be correlated with unresolved inflammation in the liver, which could be a risk factor for hepatic injury and various liver diseases (Figure 41) (Calvente et al., 2019). However, the relatively few numbers of enriched GO terms implied a slight variation between Tom⁺ and Tom⁻ NASH LSECs. Thus, it is proposed that Tom⁻ LSECs might also respond to the chronic inflammatory microenvironment in NASH liver to a lesser but significant extent than Tom⁺ LSECs. To verify this, DEG analysis was performed separately on the NASH Tom^{+/-} and normal Tom^{+/-} LSECs (Figure 42A). A Venn diagram illustrated that NASH-induced DEGs were more associated with Tom⁺ than Tom⁻ LSECs. After the ranking of 1808 NASH-induced DEGs by their fold change ratio, 93 genes were assumed to be more induced in Tom⁺ LSECs (Figure 42B). These genes participated in cytokine production and the immune response (Figure 42C). My results suggest that Tom⁺ LSECs contribute to the chronic inflammatory niche, which may also affect the immune response transcriptomes of Tom⁻ LSECs.

3.5. scRNA-Seq of p16^{high} Cells in Normal Kidney

Previous studies have suggested that cellular senescence plays a crucial role in the pathogenesis of age-related renal diseases (Docherty et al., 2019). Therefore, I conducted a single-cell mapping of p16^{high} cells within the normal kidney. Utilizing a 5-month-old mouse as a model organism, I obtained 3,042 cells and successfully identified 6 distinct cell types through the use of markers, as previously described (Figure 43) (Ransick et al., 2019). Notably, Tom⁺ cells were found to be dispersed across all cell types (Figure 44).

GO analysis of the genes downregulated in Tom⁺ proximal tubular cells identified pathways related to RNA processing, the RNA-induced silencing complex (RISC), and H3-K4 methylation (Figure 45), which are consistent with the characterization of senescence as reported in previous studies (Johnson et al., 2013; Leon and Aird, 2019; Min et al., 2018; Pluquet et al., 2015). Furthermore, the analysis revealed that Tom⁺ proximal tubular cells displayed increased resistance to apoptosis (Figure 45).

The Tom⁺ distal tubular cells exhibited elevated activity in RNA biosynthesis (Figure 46). mRNA and protein synthesis were activated in senescent cells (Johmura et al., 2021). Additionally, terms related to purine were enriched in the downregulation of Tom⁺ distal tubular cells (Figure 46). It is well established that the purine pathway is robustly

suppressed in senescent cells (Delfarah et al., 2019).

GO analysis, activation of the calcium ion response was observed in Tom⁺ collecting duct cells, which was associated with the induction of the AP-1 transcription factor (Figure 47).

Recent studies have demonstrated that AP-1 plays a critical role in the transcriptional network during early senescence (Martínez-Zamudio et al., 2020). Additionally, robust activation of the p53 signaling pathway was observed (Figure 47), which has been identified as a key factor in the induction of senescent cells (Rufini et al., 2013).

Furthermore, terms related to the wound response were also found to be upregulated in Tom⁺ collecting duct cells (Figure 47). It has been reported that senescent cells accumulate around wounds and accelerate wound closure (Demaria et al., 2014). The GO analysis of downregulated genes revealed that homeostasis of metal ions and pH were altered in Tom⁺ collecting duct cells (Figure 47). This homeostasis is known to be drastically altered during the senescence process (Johmura et al., 2021; Nakamura et al., 2019).

The analysis of the top 10 genes upregulated in Tom⁺ cells across various cell types revealed that Lars2 was consistently the most highly expressed among all cell types (Table 1). As a mitochondrial leucyl tRNA synthase, Lars2 plays a role in the translation of genes encoded within the mitochondria (Huang et al., 2021). Despite the lack of a clear understanding of

its specific function in senescent cells, it is hypothesized that Lars2 may contribute to the alteration of mitochondrial function within these cells and may serve as a novel marker for senescence.

3.6. Removal of p16^{high} Cells Ameliorates NASH-Induced Liver Steatosis and Inflammation

Previous research has established that senolysis, or the elimination of senescent cells, can improve various age-related diseases and extend a healthy lifespan (Baker et al., 2011, 2016). To further investigate this phenomenon, I employed a genetic model in which p16^{Ink4a}-Cre^{ERT2} mice were crossed with Rosa26-SA-lsl-DTR-IRES-tdTomato mice that encoded the diphtheria toxin receptor (DTR). This system enabled the complete ablation of Tom⁺ cells through diphtheria toxin (DT) administration (Figure 48) (Buch et al., 2005; Iwasaki et al., 2018). This allowed me to simultaneously evaluate the removal of p16^{high} cells and the improvement in senescence-related tissue dysfunction. To confirm that DT treatment effectively removed p16^{high} cells, I treated MEFs from p16-Cre^{ERT2}-DTR-tdTomato mice with Ras-induced senescence, followed by DT treatment. This resulted in a significant reduction in the total cell number (Figure 49A), Tom⁺ cells (Figure 49B), and the expression of p16^{Ink4a} (Figures 49C and 49D). For *in vivo* experiments, to eliminate p16^{high} cells, I implemented intraperitoneal injections of TAM and DT during NASH induction. To prevent irreversible NASH-induced liver dysfunction and tumor formation, I induced a short-term NASH by feeding mice a choline-deficient L-amino acid, high-fat diet (CDA-HFD) for 6 weeks, resulting in mild liver damage and fibrosis (Figures 50) (Matsumoto et al., 2013). Tom⁺ cells were significantly diminished in several organs including the kidney, lung, and liver

(Figure 51). The abnormal physical structure and the accumulation of lipid droplets were rescued by DT introduction (Figure 52). The decline in F4/80⁺ macrophages implied the alleviation of liver inflammation, consistent with the observation that Tom⁺ macrophages showed the development of SASP (Figure 34). Although recent studies have reported certain deleterious consequences as a result of the long-term and continuous elimination of p16^{high} cells or the acute removal of them in aged mice, my results suggest that short-term (3 weeks) elimination of p16^{high} cells had remarkable beneficial effects on liver steatosis. Therefore, my findings suggest that the judicious use of senolytic compounds may ameliorate various age- or senescence-associated disorders without compromising overall health.

Chapter 4. Conclusion and Discussion

A more detailed understanding of the dynamics and characteristics of senescent cells *in vivo* is needed to elucidate the role of senescent cells in aging. Although the exact definition of senescent cells remains controversial, the most definitive feature of senescent cells *in vitro* is a permanent loss of proliferative capacity. Quantitative distribution analysis of Tom⁺ cells suggested that p16^{high} cells in these tissues do not divide for long periods and lost their proliferative potential. As previously reported, the numbers of p16^{high} cells in the kidney, lung, liver, and skin significantly increased with age (Grosse et al., 2020). According to a recent simulation analysis, the half-life of p16^{high} cells was predicted to be very short, a few days in young mice and a few weeks in old mice (Karin et al., 2019). However, my analysis suggests that the half-life ranges from 2.6 to 4.2 months, depending on the tissue. This study is presumed to be more reasonable in that the cell counts were measured *in vivo*. The reason for the rather large difference from the simulation results is unclear, but it should be mentioned that other studies using 53BP1 foci after non-lethal irradiation (Le et al., 2010) and *p16^{Ink4a}* mRNA expression (De Cecco et al., 2019) have predicted half-lives comparable to those of this study.

Recent studies have reported conflicting results, with one study reporting that p16^{Ink4a}-positive cells were detected in the lungs shortly after birth (Mochel et al, 2020) and the

other reporting that they were barely detected in any tissue, even at two months of age (Grosse et al, 2020). In my model, I detected p16^{high} cells in all tissues of 2-month-old mice. These differences may be due to sensitivity, and I suspect that my established mice may be able to analyze more essential p16^{Ink4a}-positive cells.

I successfully performed scRNA-seq of p16^{high} cells from the liver of normal and NASH mice, as well as the kidney. Most importantly, Tom⁺ cells were not exclusively found in certain clusters but were distributed among various cell types in all tissues. In other words, the p16^{high} cells did not represent any one particular cell type. In normal liver, it has been previously reported that the majority of Tom⁺ cells are LSECs and a small number are Kupffer cells (Grosse et al., 2020). Kupffer cells were classified into two subtypes, Kupffer cells, and EC-like Kupffer cells. EC-like Kupffer cells express both Kupffer and LSEC markers simultaneously, which was also confirmed in another data set (Consortium et al., 2020). However, to solidify the existence of this unique subtype, histological evidence using Kupffer and LSEC markers is needed.

GO analysis showed that Tom⁺ cells had highly heterogeneous senescent features that show proteolytic dysfunction in LSECs from the normal liver (Marongiu et al., 2016), the loss of immune cell identity and higher apoptosis resistance in Kupffer cells from the normal liver

(Oishi and Manabe, 2016; Solana et al., 2012; Sasaki et al., 2001), augmentation of cytokine signaling and higher apoptosis resistance in macrophages from the NASH liver (Zhang et al., 2019; Sasaki et al., 2001), and higher mitochondrial activity in LSECs from the NASH liver (Kaplun et al., 2013). DEGs comparing Tom⁺ cells from the normal liver with Tom⁺ cells from the NASH liver were more numerous than those comparing Tom⁻ cells with each other.

In particular, the group of genes involved in inflammation was variable, suggesting that chronic inflammatory field formation in NASH is induced by Tom⁺ LSECs. Furthermore, short-term removal of p16^{high} cells ameliorated fat deposition and inflammation, confirming the contribution of p16^{high} cells to the development of NASH.

In the kidney, Tom⁺ cells also had heterogeneous senescent features like the liver showing the activation of RNA processing, the RISC, and H3-K4 methylation in proximal tubular cells (Johnson et al., 2013; Leon and Aird, 2019; Min et al., 2018; Pluquet et al., 2015), the activation of RNA biosynthesis (Johmura et al., 2021) and the downregulation of purine pathway in distal tubular cells (Delfarah et al., 2019), and the activation of AP-1 and p53 signal pathway (Martínez-Zamudio et al., 2020, Rufini et al., 2013) and the collapse of homeostasis of metal ions and pH (Johmura et al., 2021; Nakamura et al., 2019) in collecting

duct cells. Also, Tom⁺ collecting duct cells are highly related to hypertension and injury-induced renal fibrosis (Kang et al., 2015; Wang et al., 2009), which are involved in age-associated renal dysfunction.

Although the existence of endothelial cells with high expression of $p16^{Ink4a}$ has been proposed previously (Kan et al., 2012), my *in vivo* study showed the presence of $p16^{high}$ cells in almost all types of endothelial cells in the liver and kidney. These results suggest that cellular senescence in endothelial cells contributes to the aging process. In addition, since mice with double deficiency of $p16^{Ink4a}$ and $p53$ are more prone to endothelium-derived angiosarcoma (Sharpless et al., 2002) and $p16^{Ink4a}$ mutations are frequently found in human angiosarcoma (Megquier et al., 2019), $p16^{high}$ cells in endothelial cells may be due to an antitumor function, one of the biological significances of cellular senescence.

As described above, this study has revealed many previously unknown issues related to the dynamics and properties of senescent cells *in vivo*, including the following: (1) $p16^{high}$ cells are present in all tissues; (2) $p16^{high}$ cells permanently lose proliferative capacity; (3) the number of $p16^{high}$ cells increases with age; (4) the half-life of $p16^{high}$ cells is about several months and varies depending on the tissue; (5) this is the first study to analyze the transcriptome of $p16^{high}$ cells *in vivo* at the single cell level; (6) $p16^{high}$ cells are highly

heterogeneous across tissues and cell types, many of which are strongly associated with age-related tissue dysfunction; and (7) removal of p16^{high} cells ameliorates lipidosis and inflammation in the liver of NASH model mice. Although adverse health effects of senolytic treatment on health have been reported (Grosse et al., 2020; de Mochel et al., 2020), my results suggest that an appropriate senolytic treatment could be beneficial in the treatment of various age-related diseases.

The mouse model developed in this study can be a powerful tool for analyzing the dynamics and characteristics of p16^{high} cells *in vivo*. Analysis of sections revealed that p16^{high} cells accumulate *in vivo* with aging. However, it is not clear whether the properties of p16^{high} cells change with aging. In this study, scRNA-seq analysis was performed using mice that were not yet in the aging state (7-month-old). By comparing scRNA-seq of p16^{high} cells from middle-aged and aged mice, it becomes clear whether the properties of p16^{high} cells can change with aging.

Furthermore, p16^{Ink4a} is the most used marker of senescent cells, it is not a completely specific marker of this process (Gorgoulis et al., 2019; Sharpless and Sherr, 2015). Therefore, to develop a deeper understanding of senescent cells related to aging, it is necessary to explore other markers of senescent cells. Performing scRNA-seq on my mouse model of the

aging state could be used to identify such markers. Furthermore, although the contribution of senescent cells to pathology and aging in the liver is being studied (Krizhanovsky et al., 2008; Lujambio et al., 2013; Yoshimoto et al., 2013), the role in the kidney has not yet been validated. Therefore, it is necessary to conduct a more detailed analysis using mouse models of different ages to elucidate the contribution of senescent cells to pathology and aging in the kidney. Finally, it is known that the dynamics of senescent cells, including the half-life, are influenced by diet and disease state. Therefore, analysis of the function and dynamics of senescent cells and senescent cell removal *in vivo* under a variety of conditions, including severe NASH, will also be important in the future.

Chapter 5. Figures and Tables

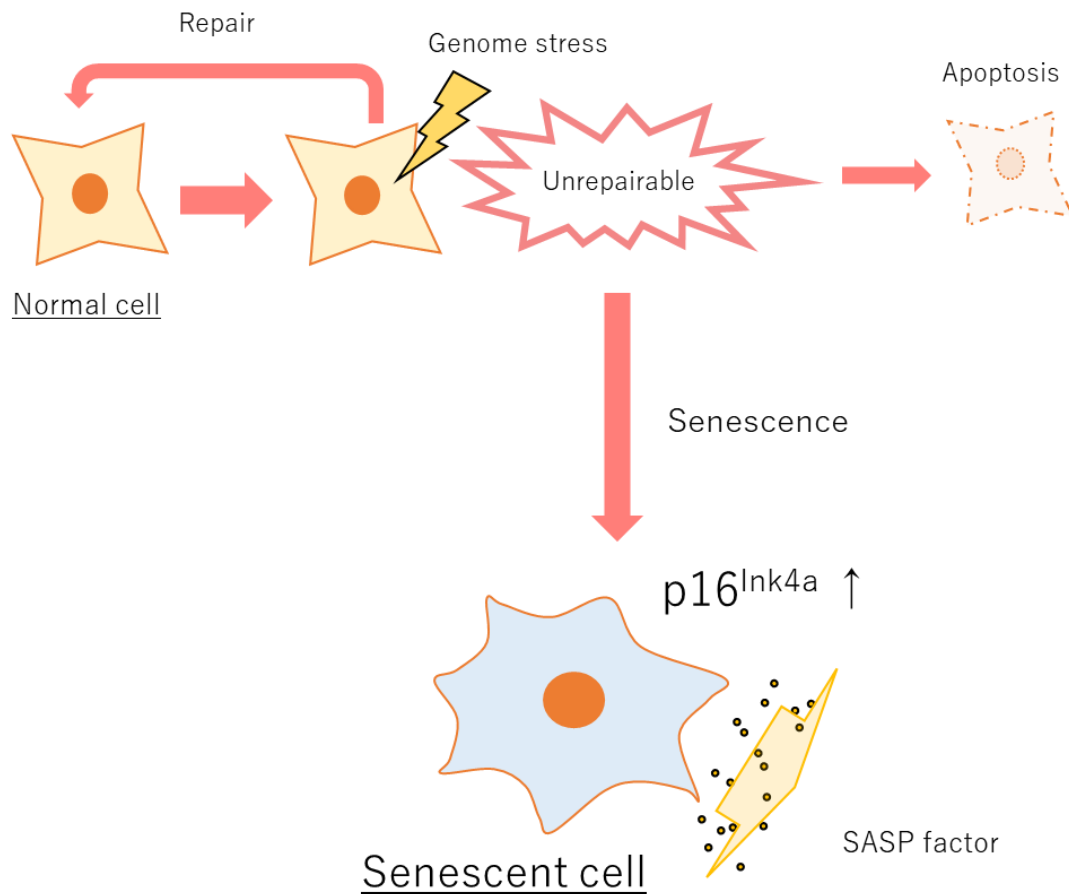


Figure 1. Mechanism of cellular senescence induction.

Cells are normally exposed to a variety of genomic stresses. If the damage is severe and unrepairable, apoptosis or cellular senescence is induced. Senescent cells express $p16^{Ink4a}$ which causes irreversible growth arrest. They also exhibit the SASP phenotype and secrete cytokines and other substances.

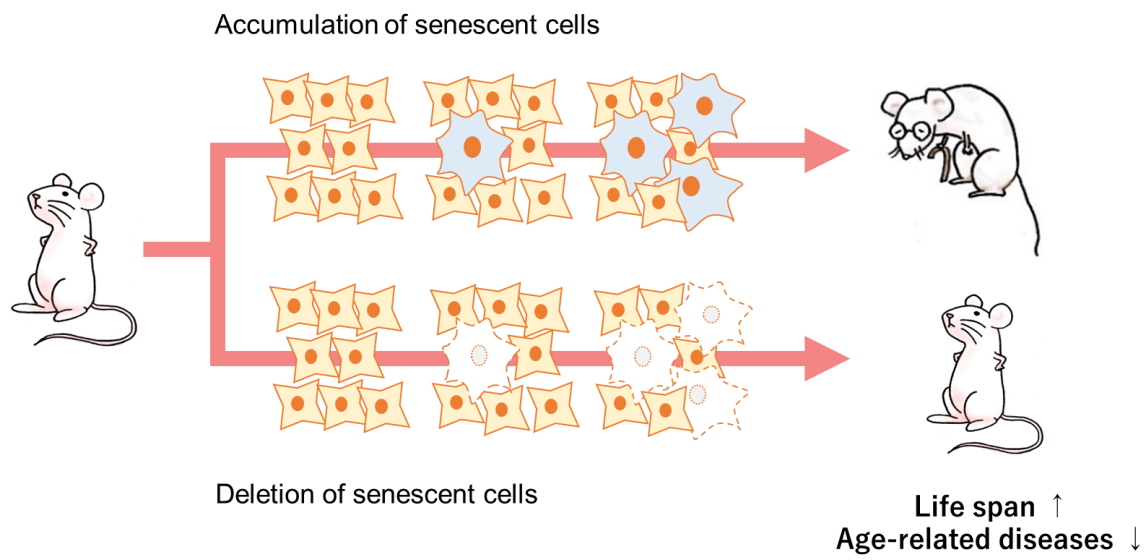


Figure 2. Senescent cells and aging.

Senescent cells accumulate *in vivo* with aging. Eliminating senescent cells reduces age-related diseases and extends lifespan.

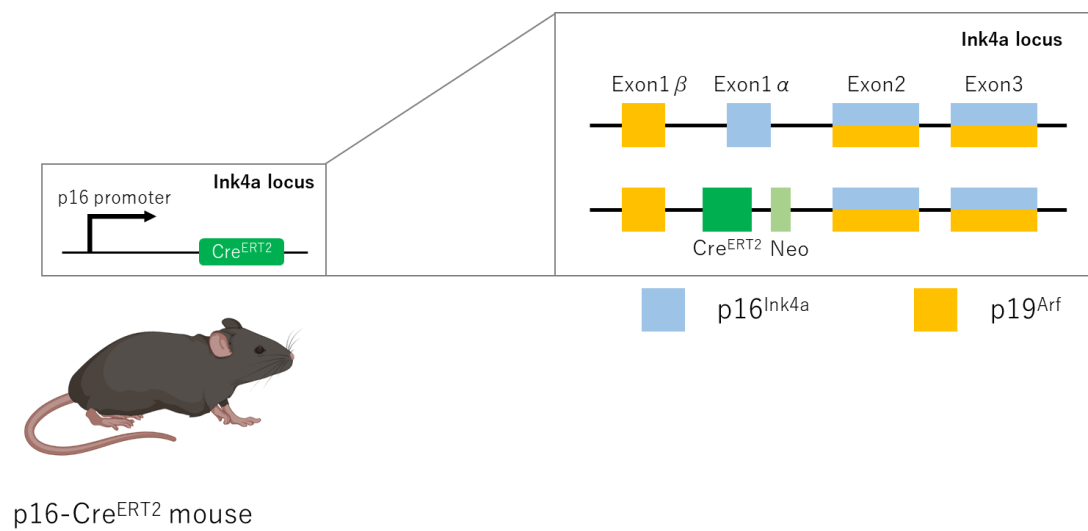


Figure 3. Scheme of p16-Cre^{ERT2} mice.

The first exon of the endogenous *p16^{Ink4a}* gene (Exon1 α) was substituted for a Cre^{ERT2} and a neo-resistant gene.

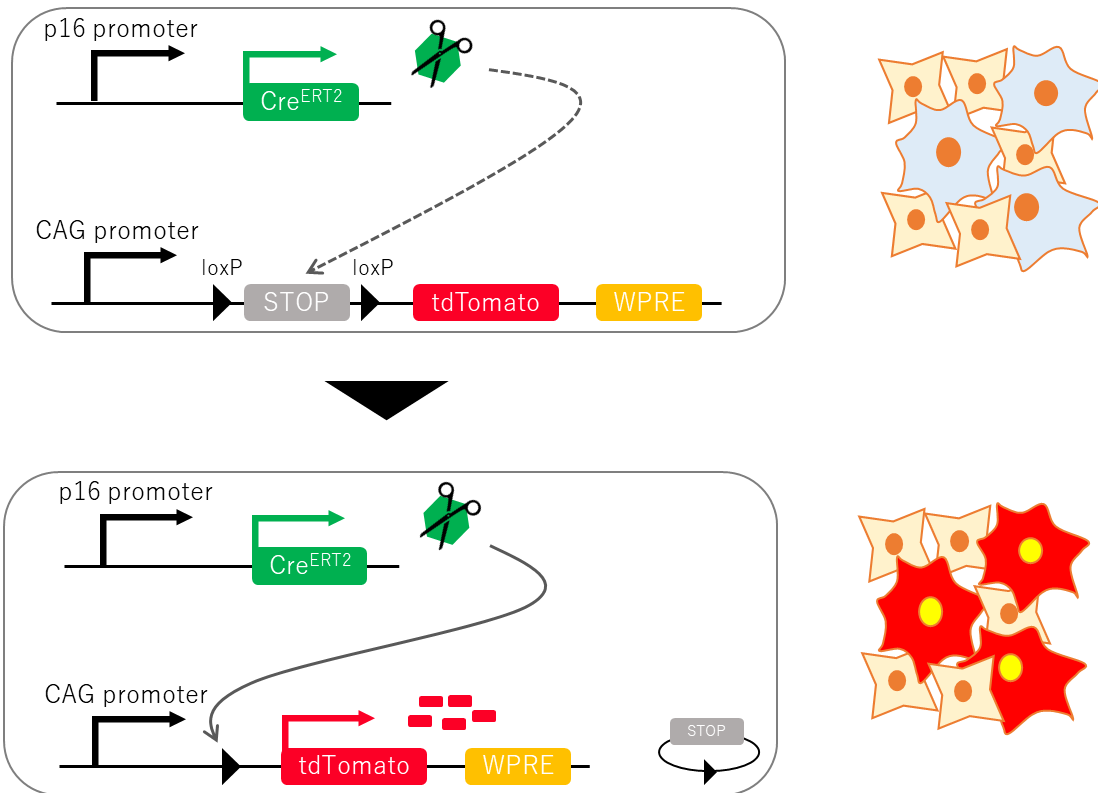


Figure 4. Scheme of p16-Cre^{ERT2}-tdTomato mice.

Tamoxifen treatment causes Cre^{ERT2} to be transported into the nucleus, where it recognizes the loxP sequence and removes the STOP sequence. This allows tdTomato to be expressed.

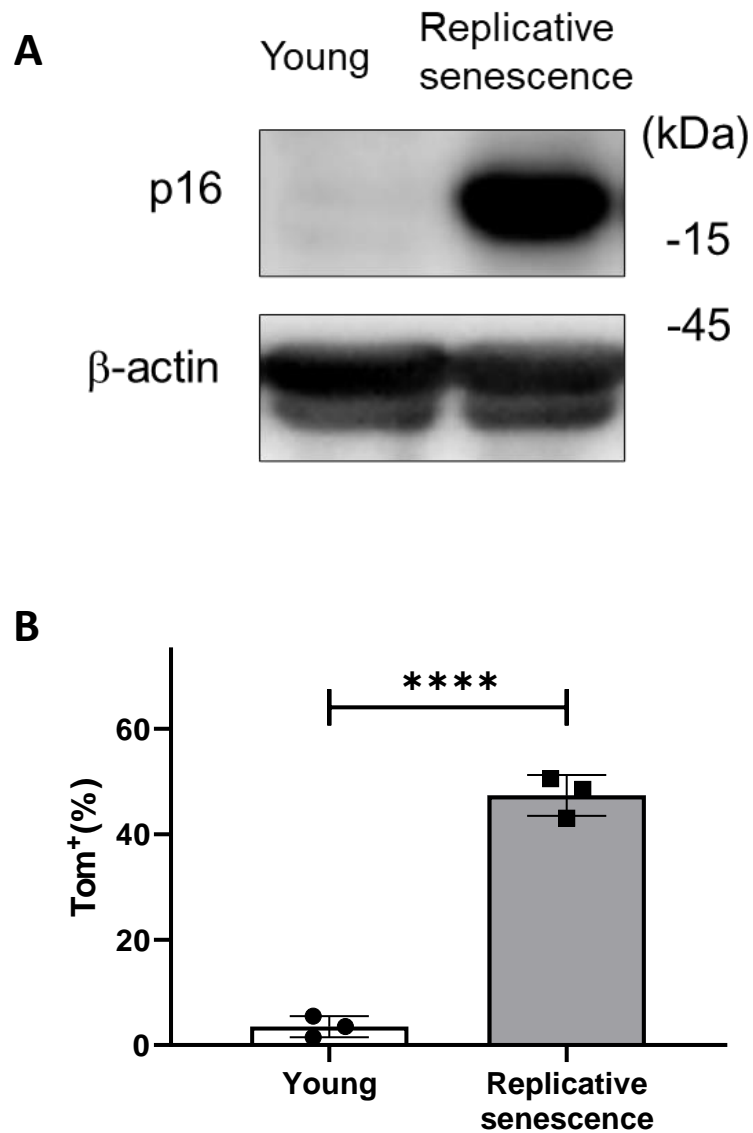


Figure 5. Labeling efficiency in MEFs.

- (A) Young (Passage 2) and replicative senescent MEFs (Passage 8) treated with 4-OHT for 3 days were immunoblotted using the indicated antibodies.
- (B) The proportion of Tom⁺ cells was measured in MEFs treated as in (A). Data are presented as means \pm SD of independent experiments and analyzed with an Unpaired two-tailed Student's t-test. ****p < 0.0001.

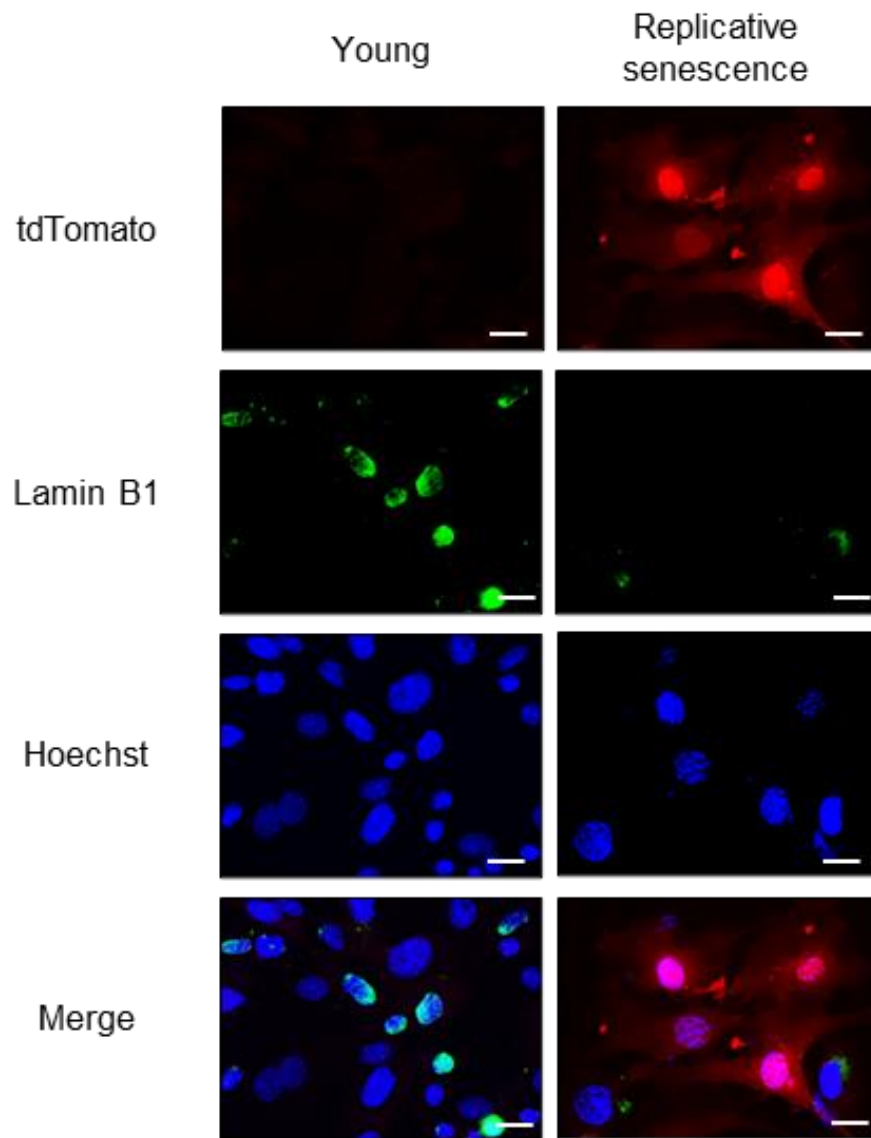


Figure 6. Immunostaining of MEFs.

MEFs treated as in Figure 5 were immunostained with the indicated antibodies (Lamin B1 and Hoechst). Scale bar, 10 μ m.

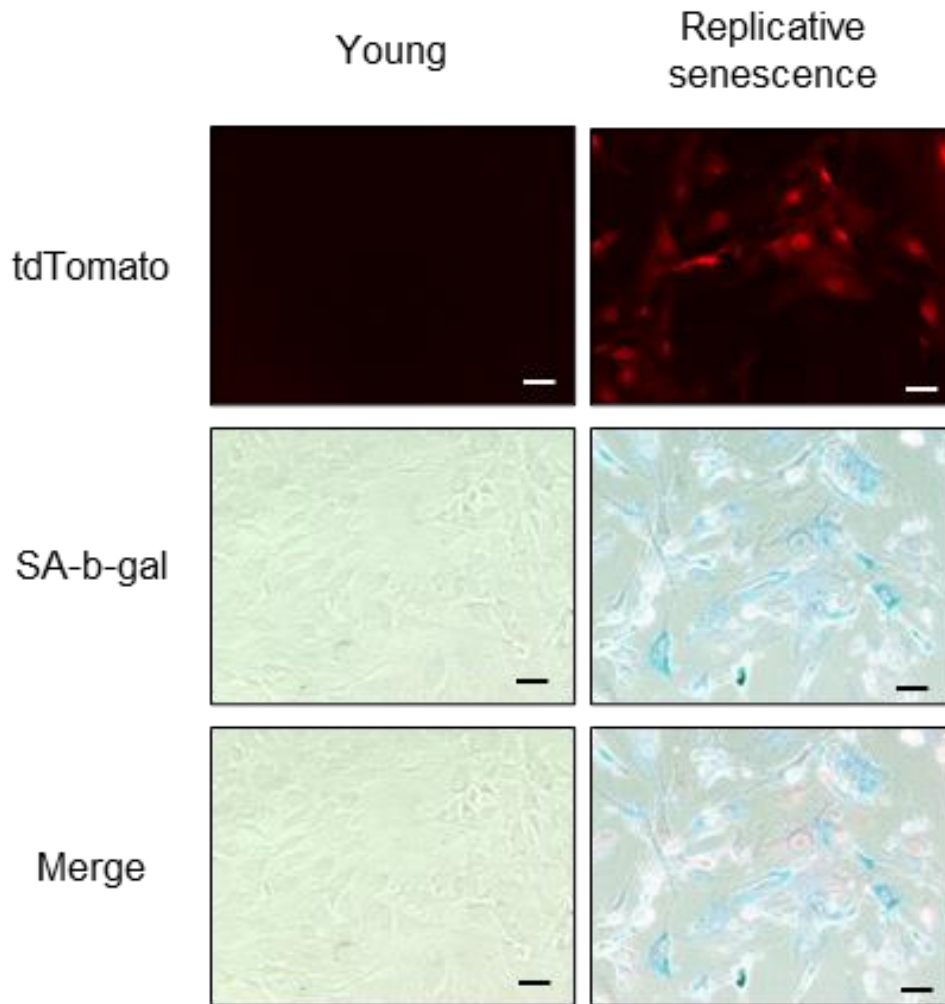


Figure 7. SA- β -gal staining of MEFs.

MEFs treated as in Figure 5 were stained with SA- β -gal. The SA- β -gal positive area is dyed blue. Scale bar, 20 μ m.

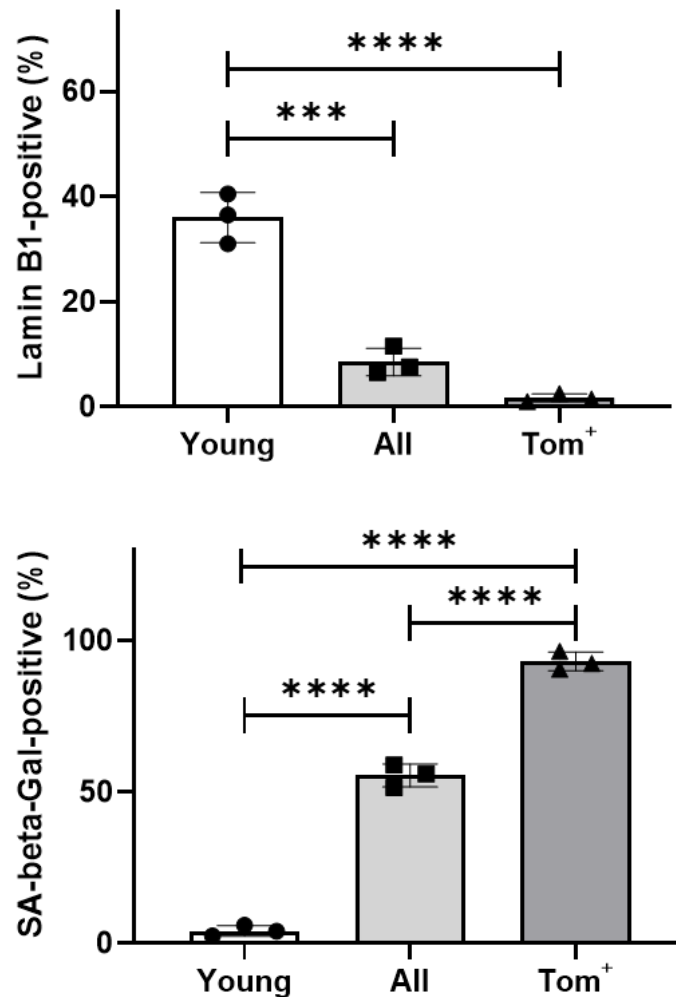


Figure 8. Proportions of senescent cells marker positive cells in MEFs.

Proportions of lamin B1- or SA- β -gal-positive cells were measured in young, total (all), and Tom⁺ replicative senescent cells. Data are presented as means \pm SD of independent experiments and analyzed with one-way ANOVA with Tukey's multiple comparisons post hoc test. ***p < 0.001, ****p < 0.0001.

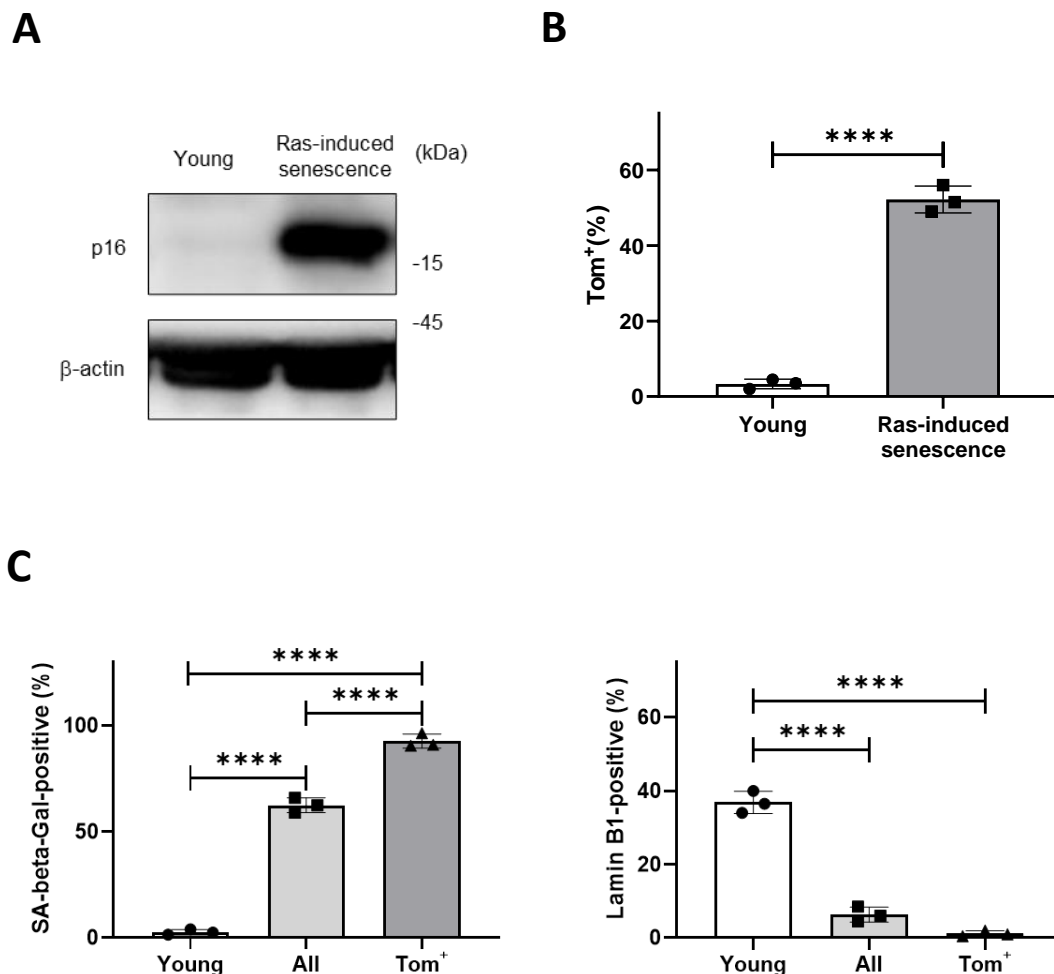


Figure 9. Validation of Ras-induced senescent MEFs.

- (A) Young and oncogenic Ras-induced senescent MEFs treated with 4-OHT for 3 days were immunoblotted using the indicated antibodies.
- (B) The proportion of Tom⁺ cells was measured in MEFs treated as in (A). Data are presented as means \pm SD of independent experiments and analyzed with an Unpaired two-tailed Student's t-test. ****p < 0.0001.
- (C) Proportions of lamin B1- or SA-β-gal-positive cells were measured in young, total (all), and Tom⁺ Ras-induced senescent cells. Data are presented as means \pm SD of independent experiments and analyzed with one-way ANOVA with Tukey's multiple comparisons post hoc test. ****p < 0.0001.

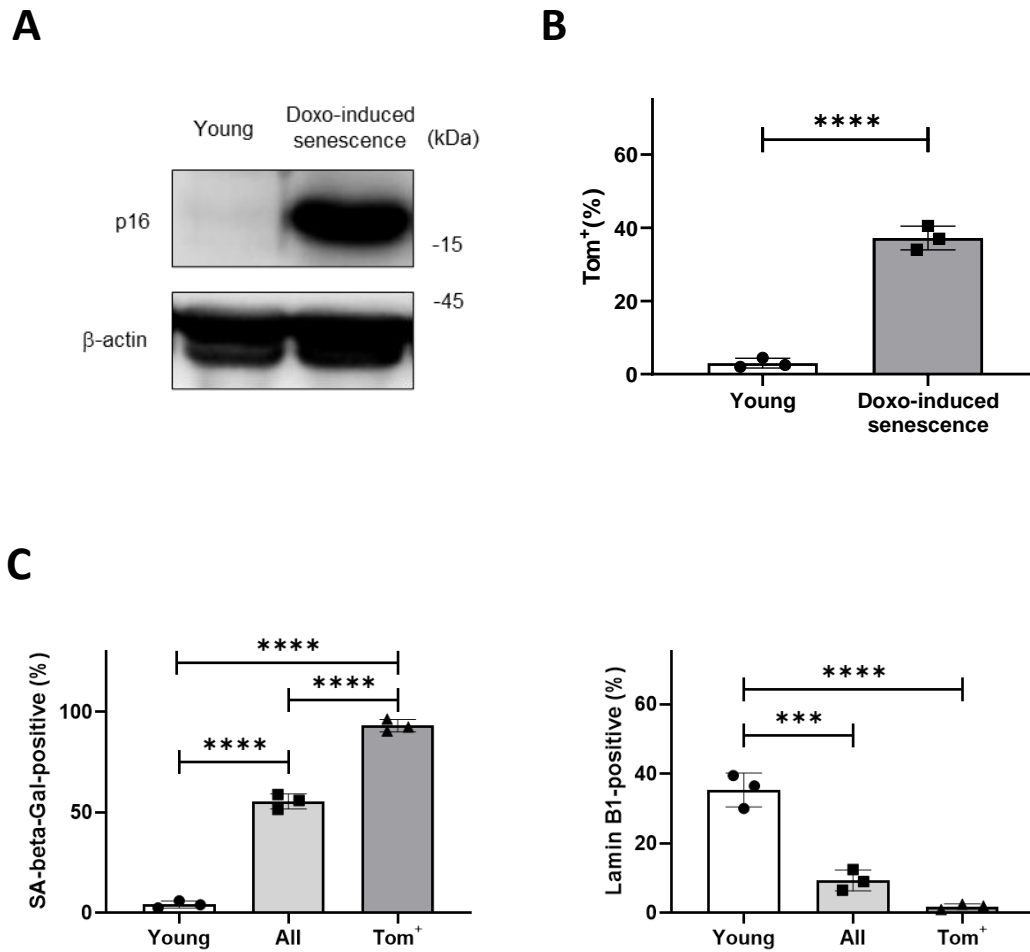


Figure 10. Validation of Doxo-induced senescent MEFs.

- (A) Young and Doxo-induced senescent MEFs treated with 4-OHT for 3 days were immunoblotted using the indicated antibodies.
- (B) The proportion of Tom⁺ cells was measured in MEFs treated as in (A). Data are presented as means \pm SD of independent experiments and analyzed with an Unpaired two-tailed Student's t-test. ****p < 0.0001.
- (C) Proportions of lamin B1- or SA-β-gal-positive cells were measured in young, total (all), and Tom⁺ Doxo-induced senescent cells. Data are presented as means \pm SD of independent experiments and analyzed with one-way ANOVA with Tukey's multiple comparisons post hoc test. ***p < 0.001, ****p < 0.0001.

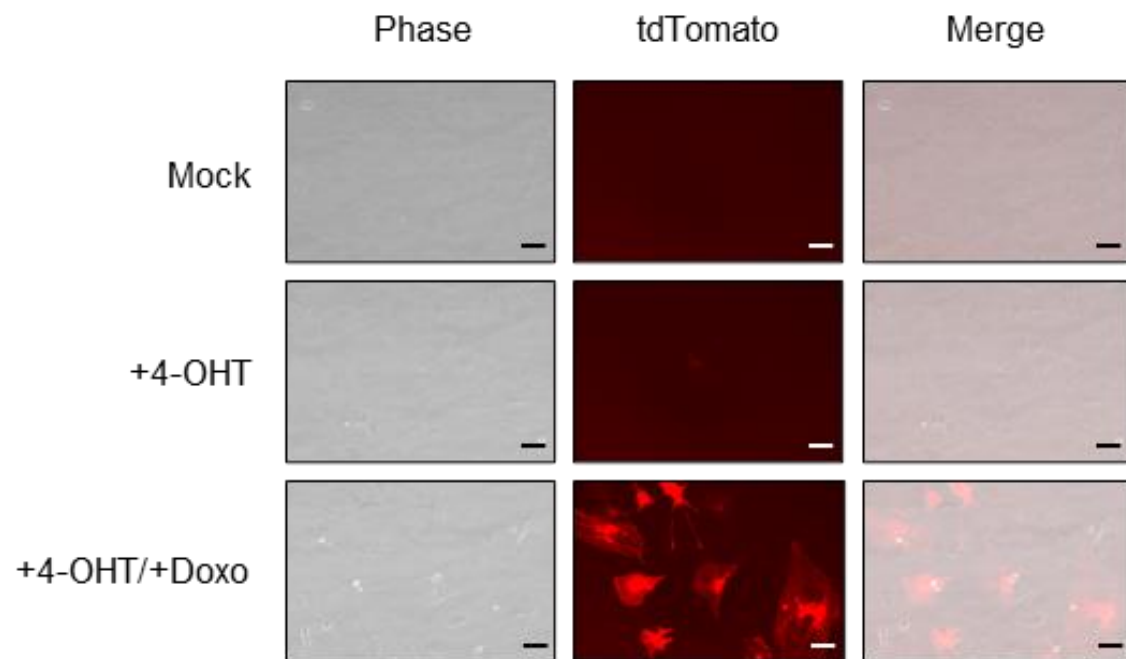


Figure 11. Fluorescent imaging of senescent MEFs.

Fluorescent imaging of mock-treated or doxorubicin (100 nM)-treated MEFs (10 days after induction) with or without 4-OHT treatments. Scale bar, 10 μ m.

MEFs were treated with mock and doxorubicin (100 nM). 10 days after induction, MEFs were treated with or without 4-OHT treatments and fluorescent images and brightfield were taken. Scale bar, 10 μ m.

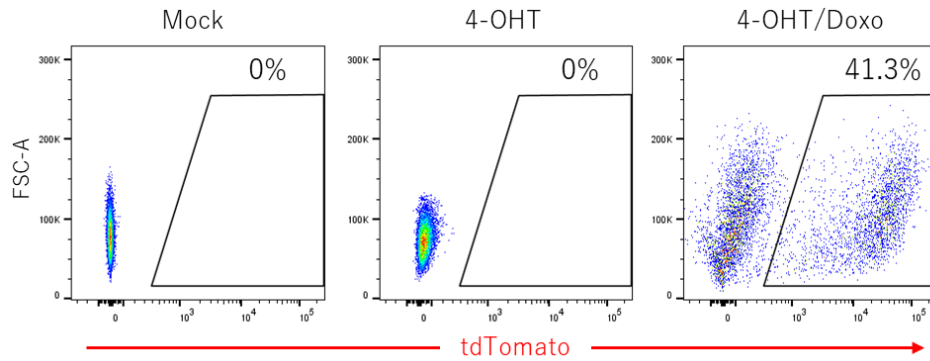
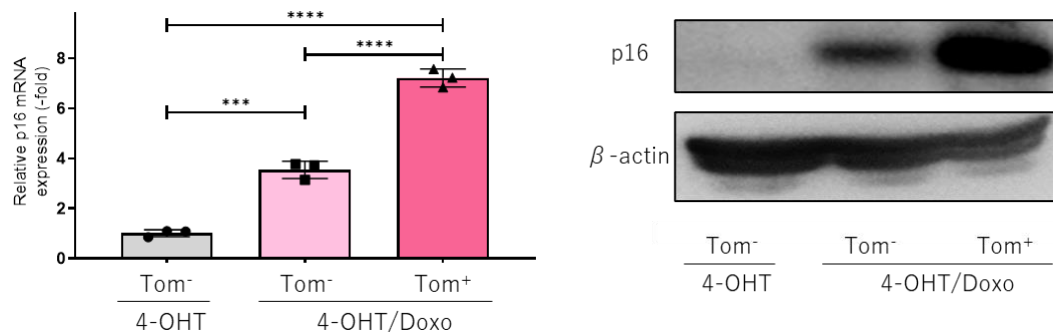
A**B**

Figure 12. Validation of Tom⁻ and Tom⁺ MEFs.

- (A) MEFs treated as in Figure 11 were sorted by FACS.
- (B) qPCR analysis and immunoblotting were performed on FACS-sorted MEFs treated as in Figure 11 using the indicated primers and antibodies, respectively. Data are presented as means \pm SD of independent experiments and analyzed with one-way ANOVA with Tukey's multiple comparisons post hoc test. ***p < 0.001, ****p < 0.0001.

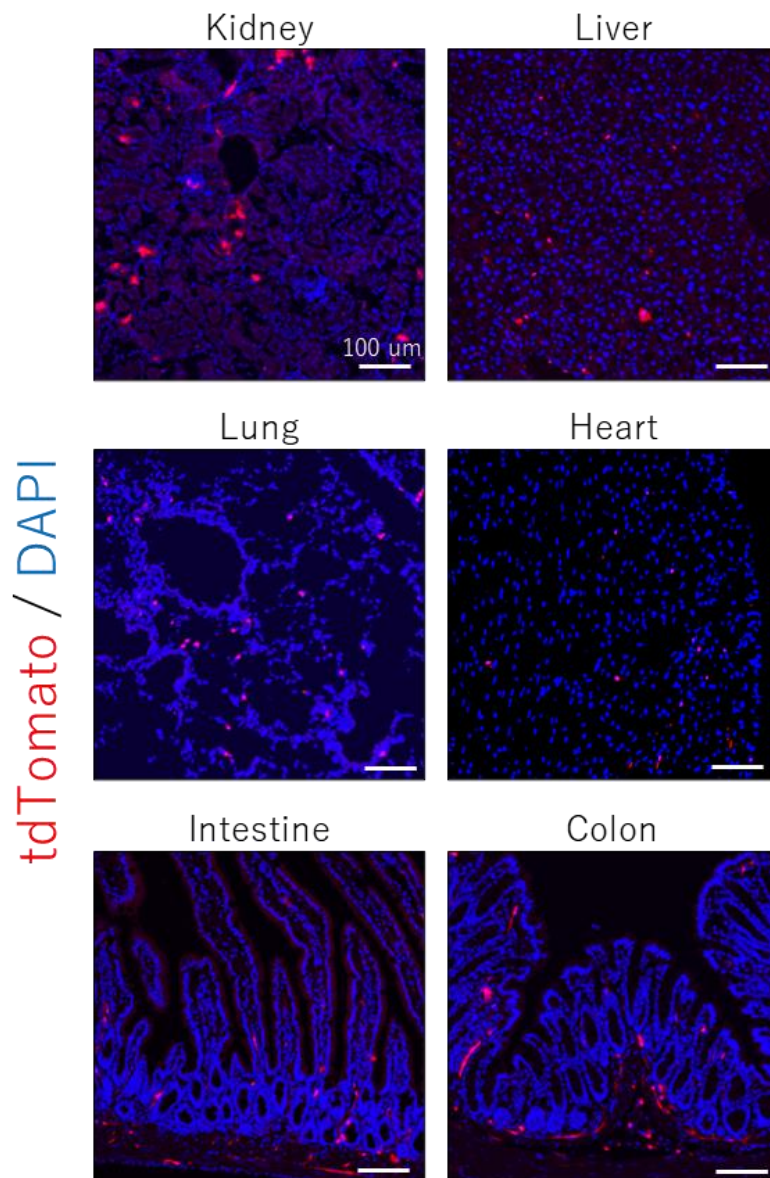


Figure 13. Fluorescent image of p16-Cre^{ERT2}-tdTomato mice.

7-month-old p16-Cre^{ERT2}-tdTomato mice were injected with TAM and fluorescent images of the indicated organs from them were taken. Scale bar, 100 μm.

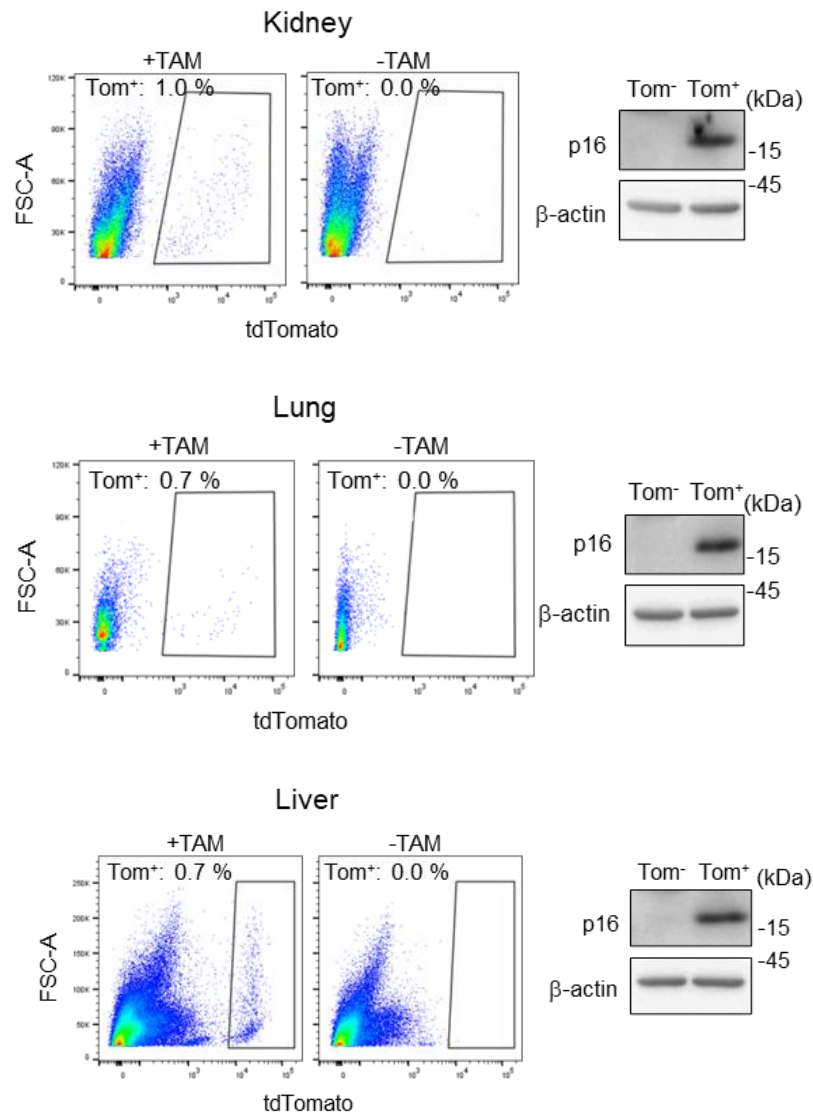


Figure 14. Validation of Tom⁻ and Tom⁺ cells from p16-Cre^{ERT2}-tdTomato

mice.

Tom⁺ cells of kidney, lung, and liver from p16-Cre^{ERT2}-tdTomato mice treated with or without TAM were identified by FACS analysis and sorted into Tom⁻ and Tom⁺ fractions. Each fraction cell was immunoblotted using the indicated antibodies.

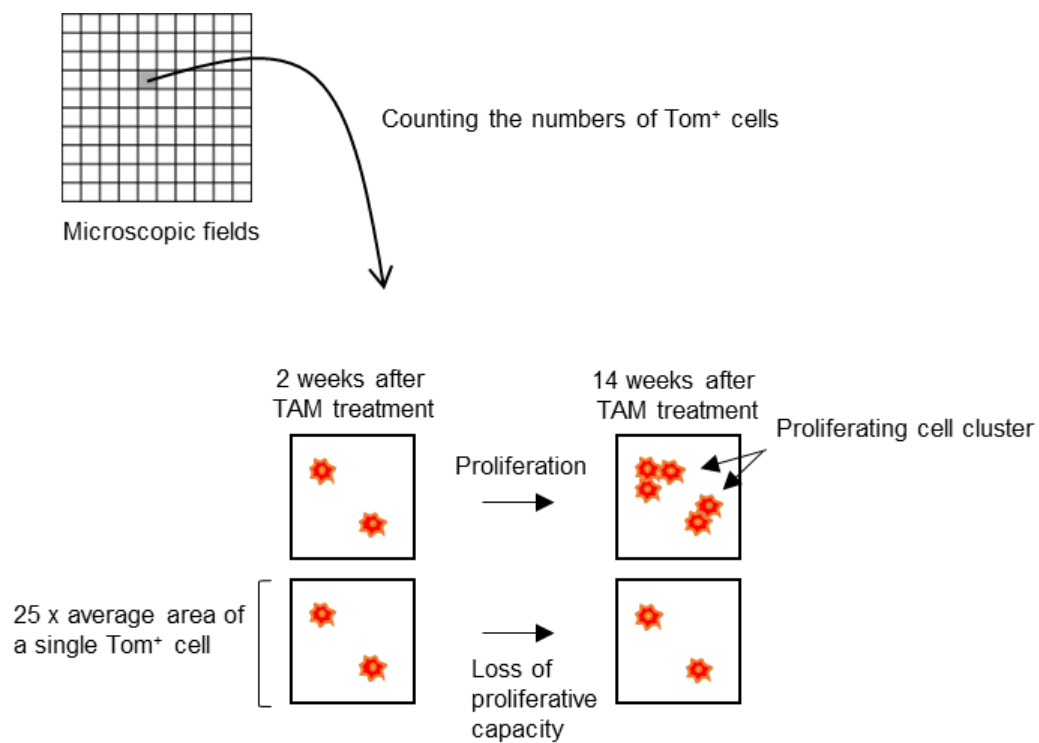


Figure 15. Schematic representation of counting of Tom⁺ cell number.

The fluorescent images were first partitioned into squares with a 25 x average area for the targeted single Tom⁺ cell (kidney: 50 mm x 50 mm, lung: 30 mm x 30 mm, liver: 30 mm x 30 mm), and the cell numbers in each square were counted.

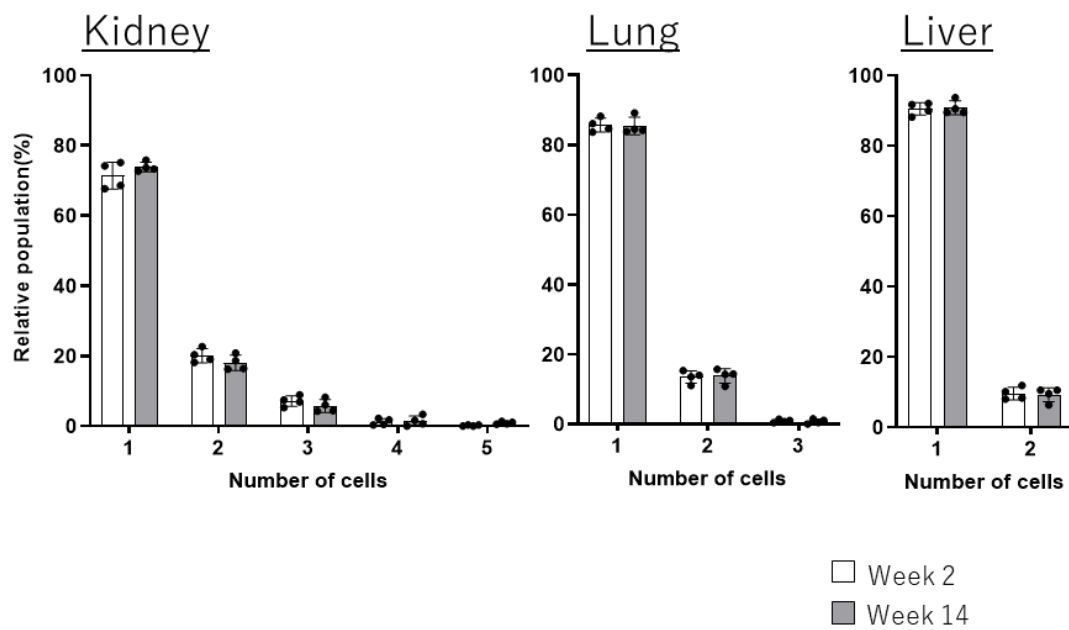


Figure 16. Validation of cluster formation in several organs.

Tom⁺ cells in each assigned square of the indicated tissues from p16-Cre^{ERT2}-tdTomato mice sacrificed 2 (n = 4) or 14 weeks (n = 4) after TAM injection were counted for quantitative distribution.

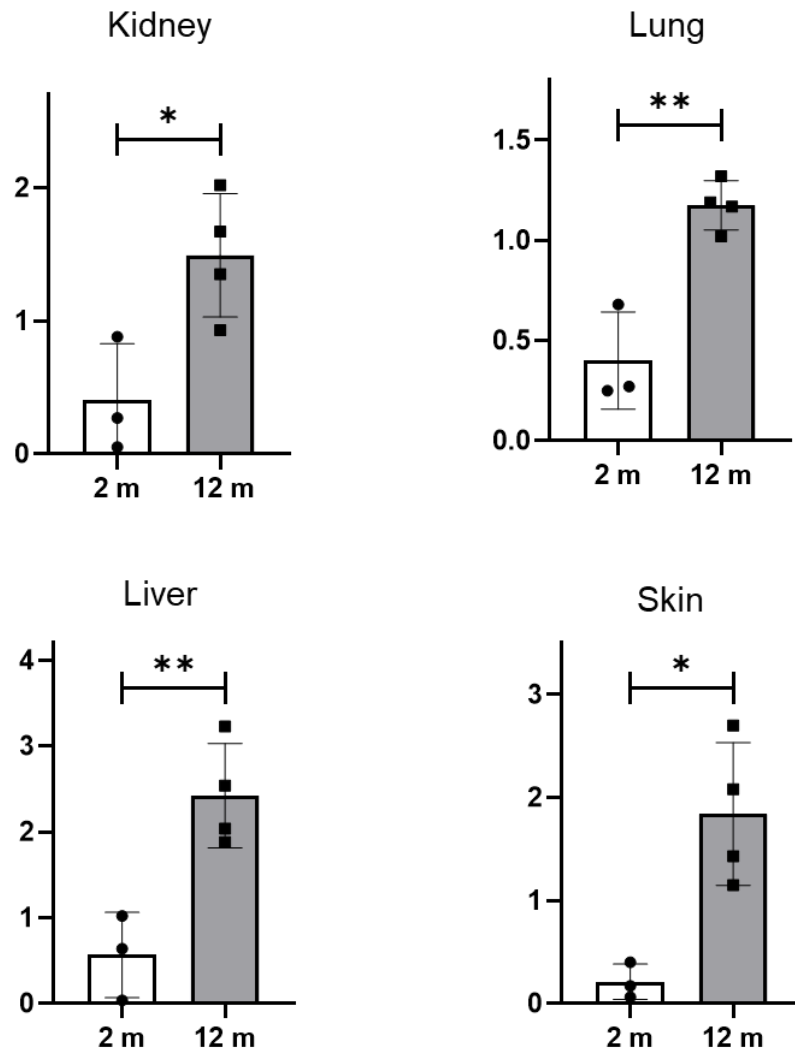


Figure 17. The number of Tom⁺ cells with aging by FACS.

The percentage of Tom⁺ cells in the indicated organs (n = 3 for 2 months and n = 4 for 12 months) was measured by FACS. p16-Cre^{ERT2}-tdTomato mice were treated as in Figure 14. Data are presented as means \pm SD of independent experiments and analyzed with an Unpaired two-tailed Student's t-test. *p < 0.05, **p < 0.01.

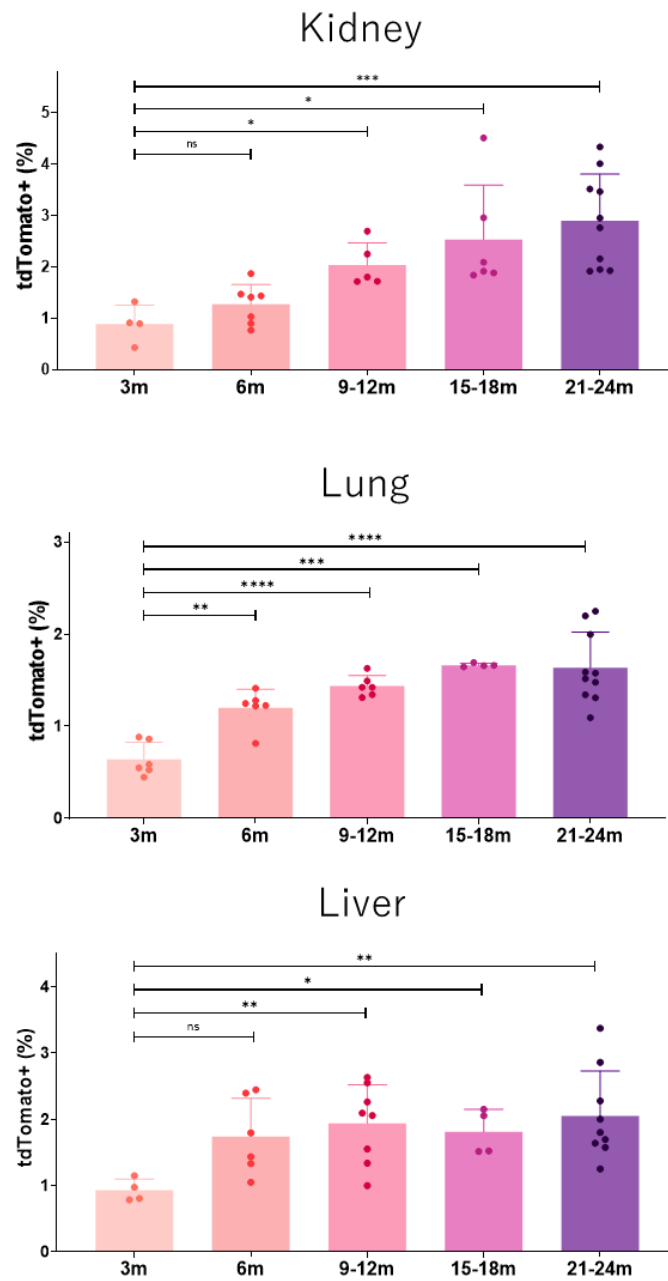


Figure 18. The number of Tom⁺ cells with aging by section analysis.

The percentage of Tom⁺ cells in the indicated organs was measured by section analysis in 5-time points. p16-Cre^{ERT2}-tdTomato mice were treated as in Figure 14. Data are presented as means \pm SD of independent experiments and analyzed with one-way ANOVA with Tukey's multiple comparisons post hoc test. * $p < 0.05$, ** $p < 0.01$, *** $p < 0.001$, **** $p < 0.0001$.

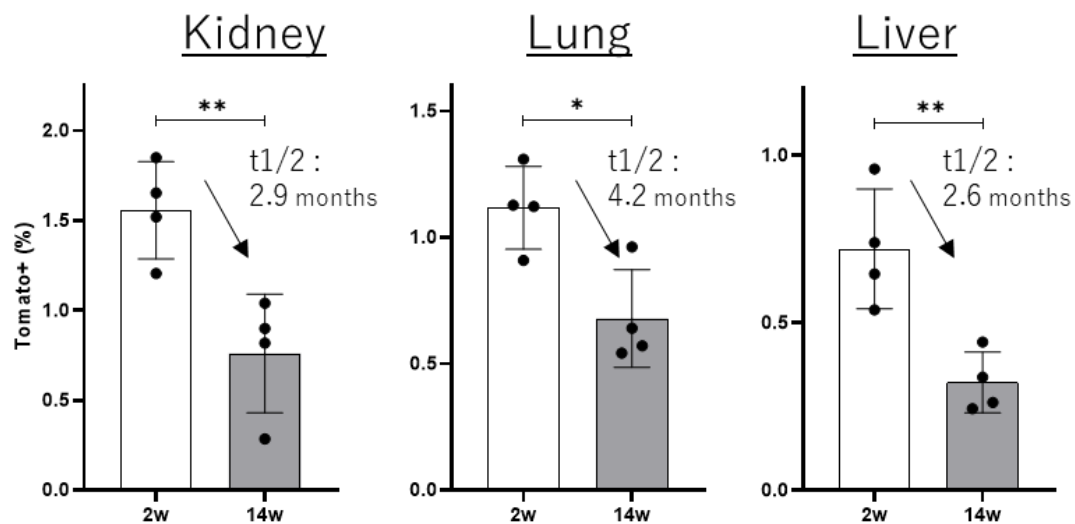


Figure 19. Validation of turnover time in several organs.

The percentage of Tom⁺ cells was counted in the indicated organs from the mice treated as in Figure 16. The half-life ($t_{1/2}$) of the Tom⁺ cells was determined. Data are presented as means \pm SD of independent experiments and analyzed with an Unpaired two-tailed Student's t-test. * $p < 0.05$, ** $p < 0.01$.

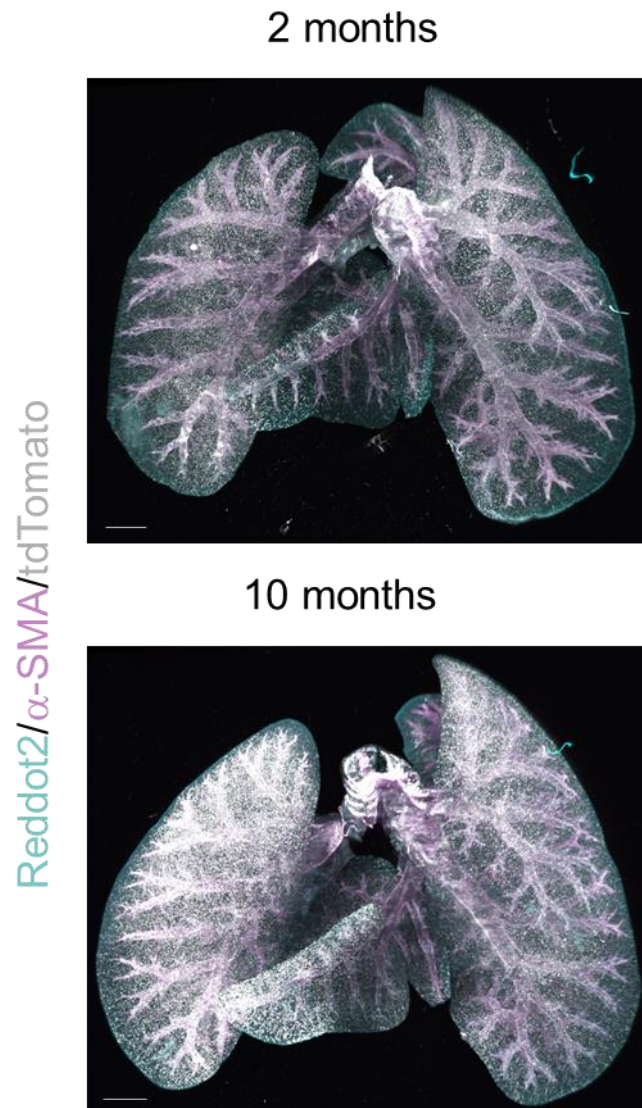


Figure 20. 3D fluorescent images in the lung.

A whole lung of 2- and 10-month-old p16-Cre^{ERT2}-tdTomato mice treated as in Figure 13 were transparent by CUBIQ. Lungs were immunostained with the indicated antibodies. Scale bar, 200 μ m.

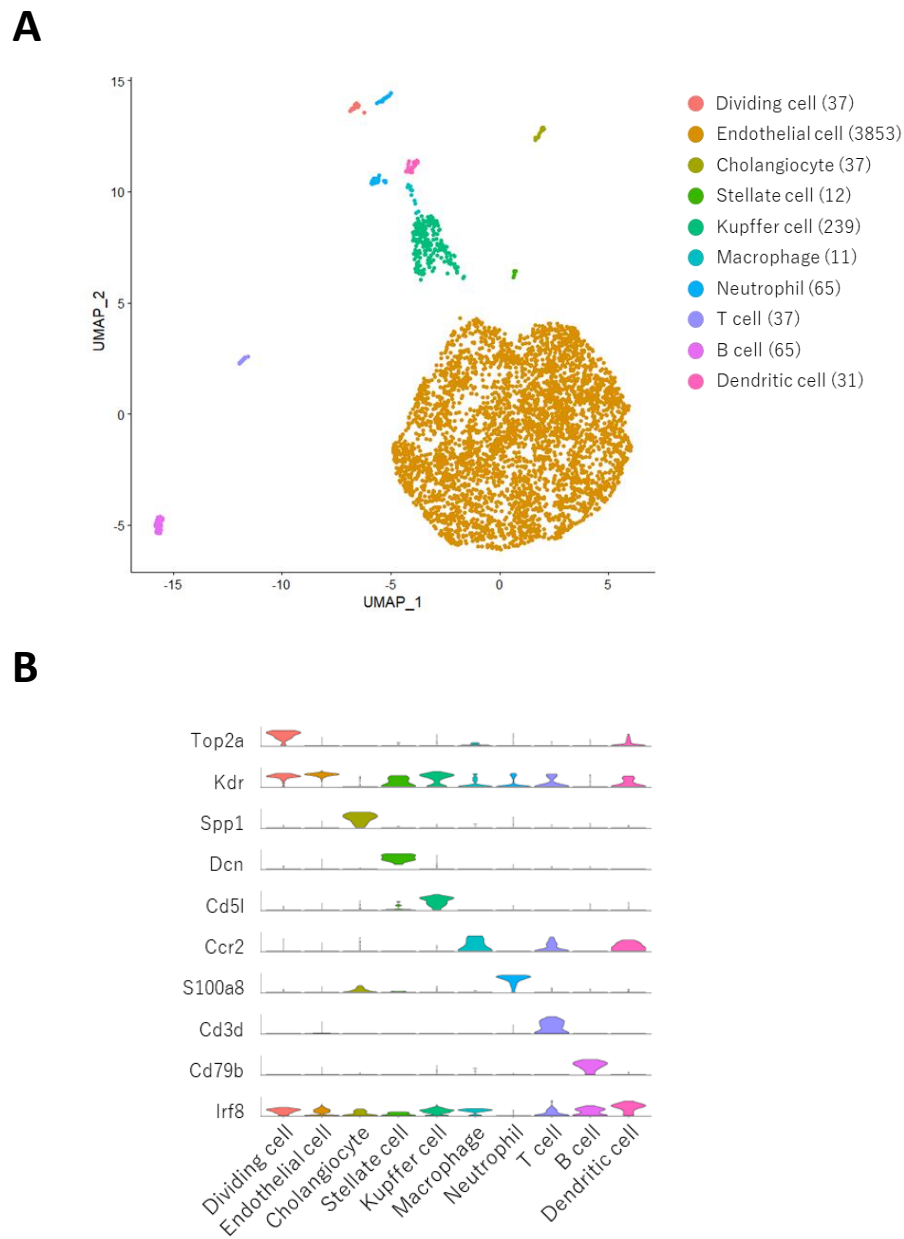


Figure 21. Clustering of normal liver cells.

- (A) UMAP of normal liver cell clusters containing 4,387 single NPC transcriptomes combined the non-separated sorted sample and the Tom⁺ sorted sample.
- (B) The violin plot for the expression level of representative genes in each cell type.

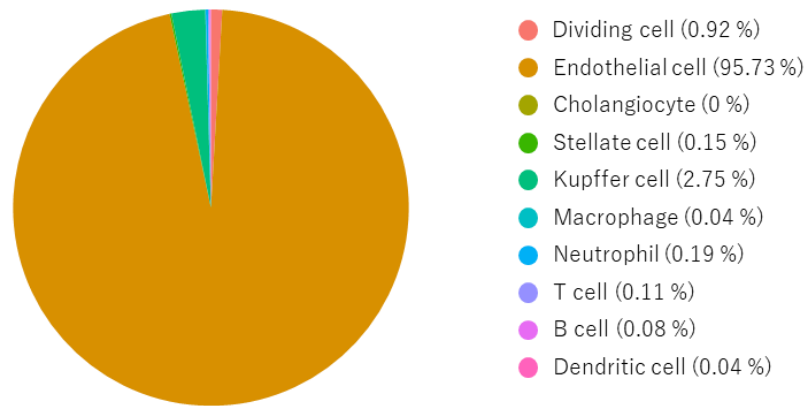
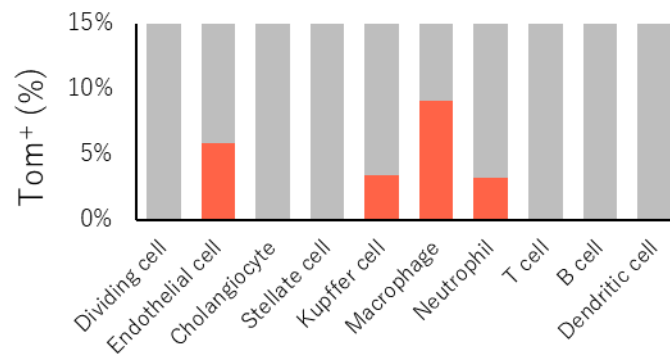
A**B**

Figure 22. Composition of Tom⁺ cells in normal liver.

(A) The cell-type composition of Tom⁺ NPCs sorted from the normal liver.

(B) The percentage of Tom⁺ cells in each cell type was calculated on a non-separated sorted sample.

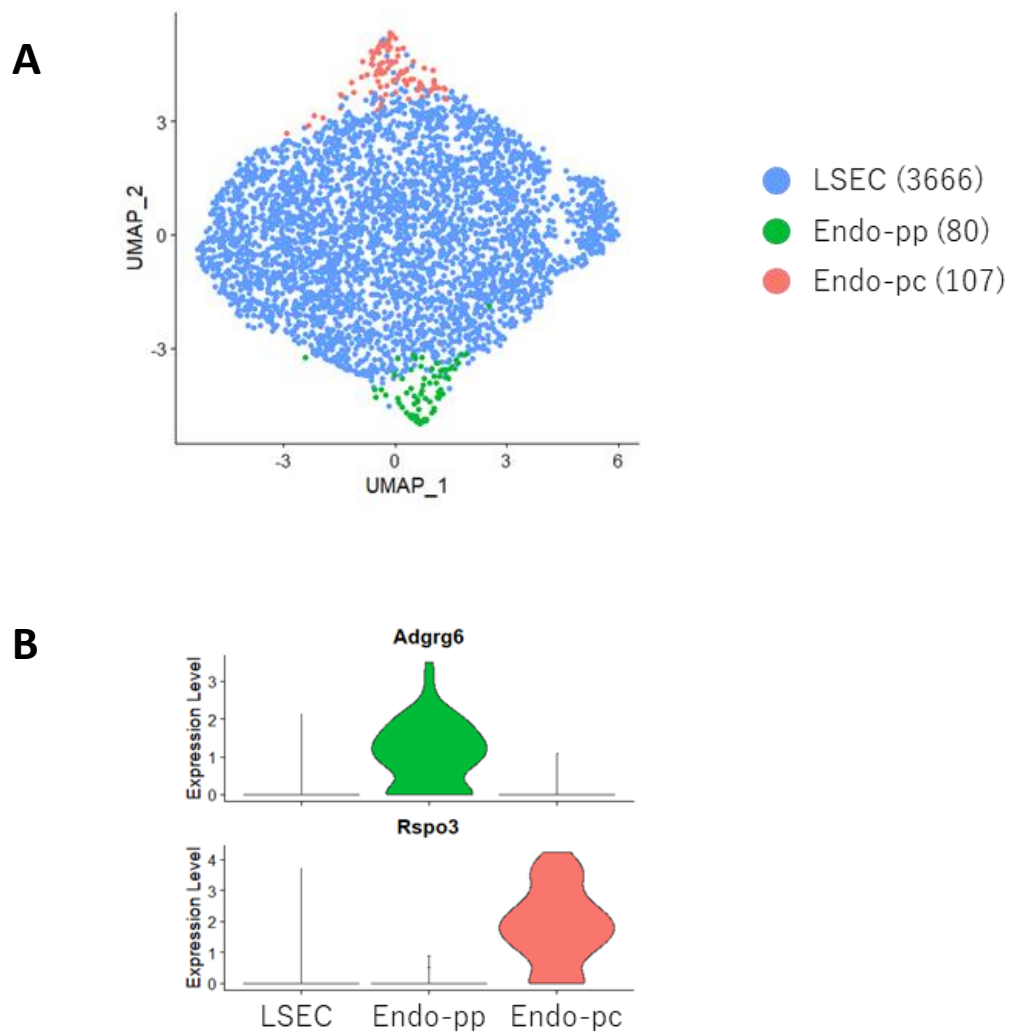


Figure 23. Clustering of endothelial cells in normal liver.

- (A) UMAP of endothelial cells in normal liver combined the non-separated sorted sample and the Tom⁺ sorted sample. LSEC: liver sinusoidal endothelial cell, Endo-pp: pericentral endothelial cell, Endo-pc: periportal endothelial cell.
- (B) The violin plot for the expression level of representative genes in each subtype.

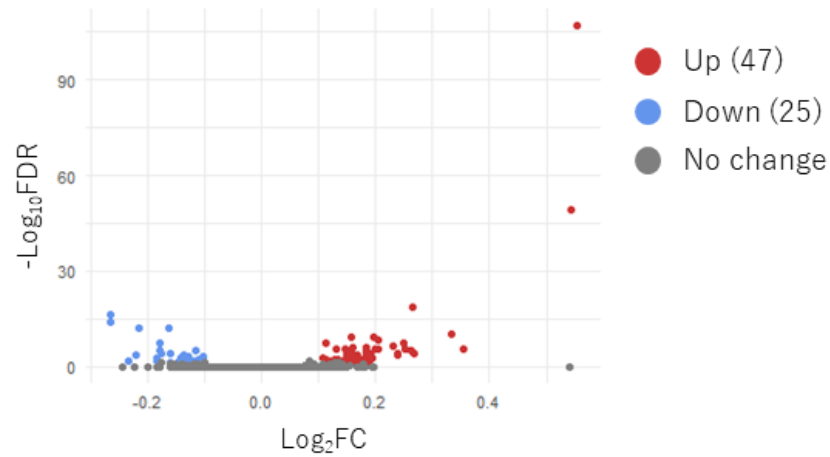
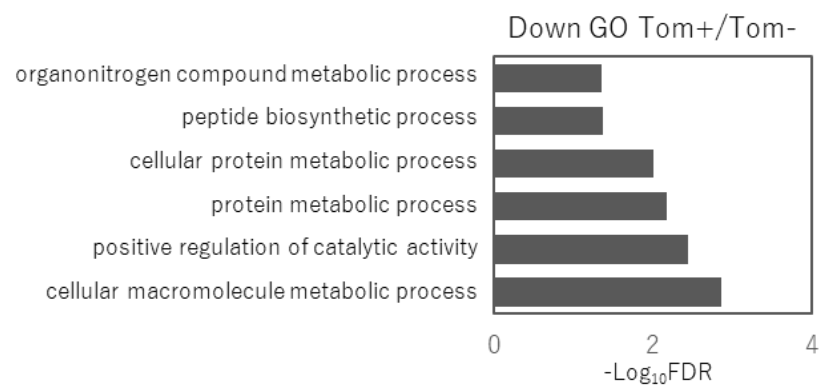
A**B**

Figure 24. Validation of Tom⁺ and Tom⁻ LSECs in normal liver.

(A) DEGs of Tom⁺ compared with Tom⁻ LSECs using volcano map. Red dots represent upregulated DEGs, blue dots represent downregulated DEGs, and gray dots represent non-DEGs. The DEGs were identified by FDR < 0.05 and Log₂FC > 0.1 or < -0.1.

(B) The enriched GO terms in downregulated DEGs.

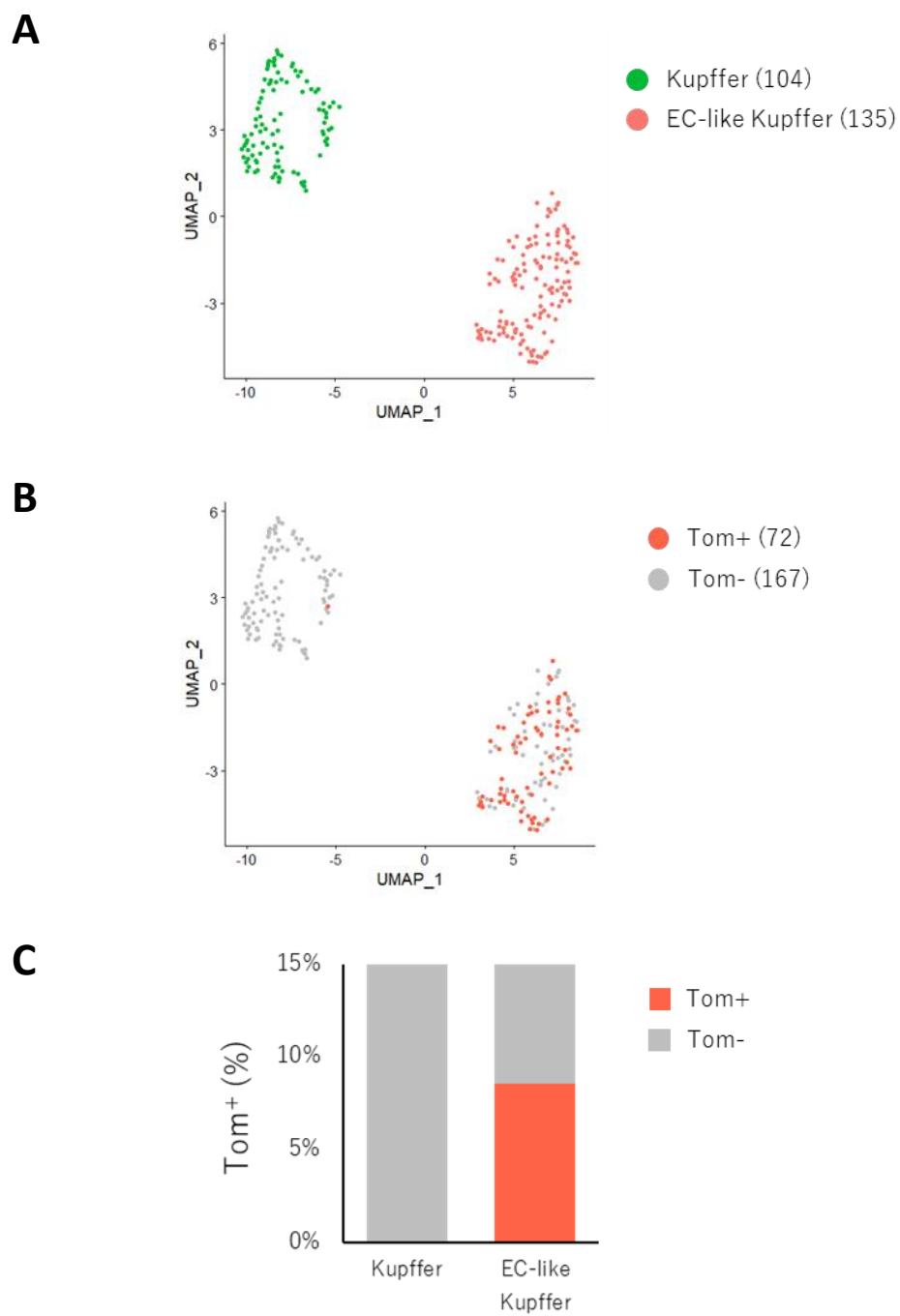
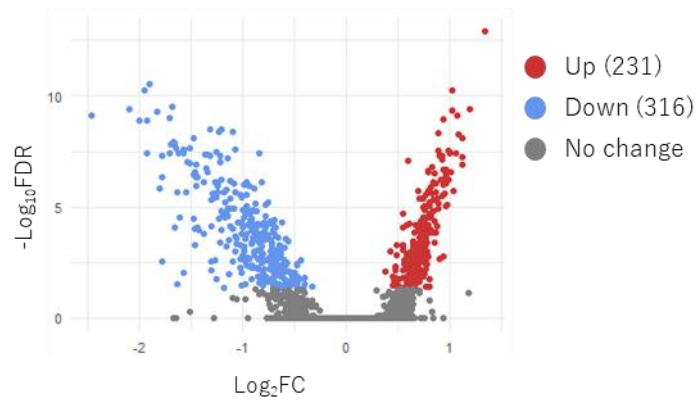


Figure 25. Clustering of Kupffer cells in normal liver.

- (A) UMAP for subtype classification of Kupffer cells.
 (B) UMAP for distribution of Tom⁺ cells in Kupffer cells.
 (C) Percentage of Tom⁺ cells for Kupffer cell subtypes calculated by the non-separated sorted sample.

A



B

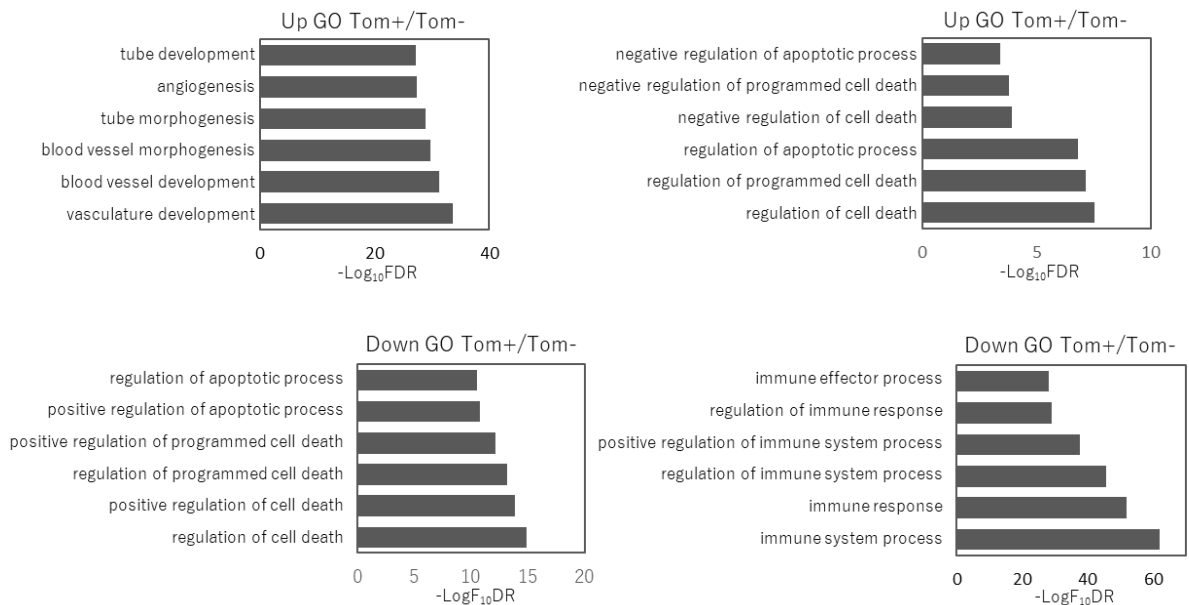
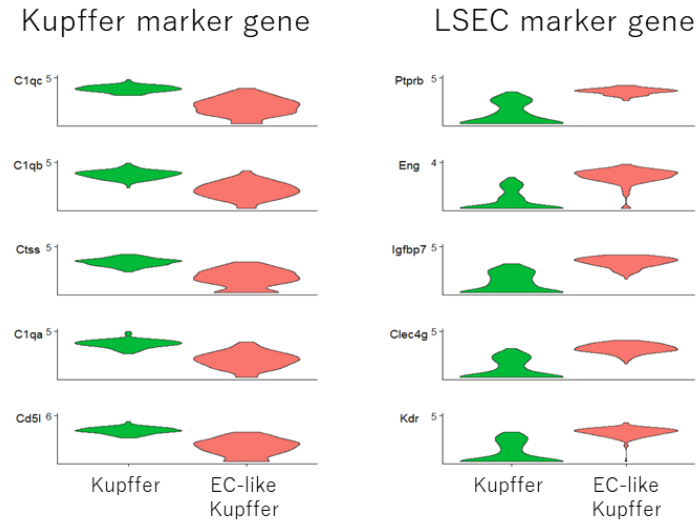


Figure 26. Validation of Tom⁺ and Tom⁻ Kupffer cells in normal liver.

(A) DEGs of Tom⁺ compared with Tom⁻ Kupffer cells using volcano map. Red dots represent upregulated DEGs, blue dots represent downregulated DEGs, and gray dots represent non-DEGs. The DEGs were identified by FDR < 0.05 and Log₂FC > 0.1 or < -0.1.

(B) The enriched GO terms in upregulated or downregulated DEGs.

A



B

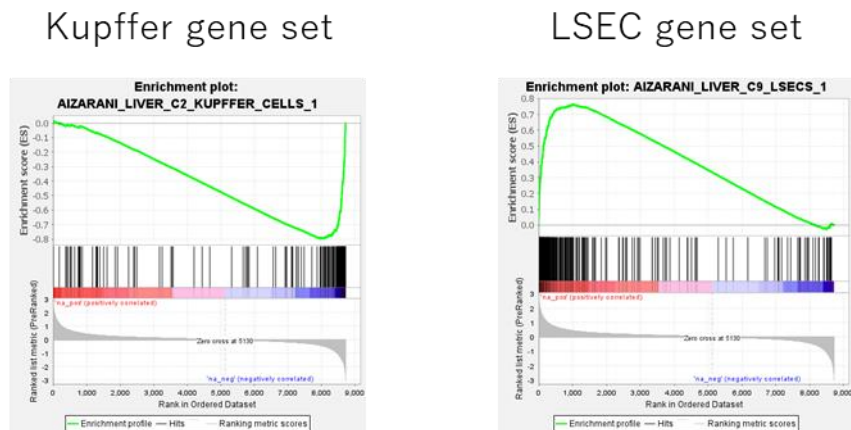


Figure 27. Differential expression of marker genes in Kupffer cells subclusters.

- (A) Violin plot of the expression level of the top five marker genes of Kupffer cells or LSECs.
- (B) GSEA enrichment plots of cell type signature gene set of Kupffer cells or LSECs.

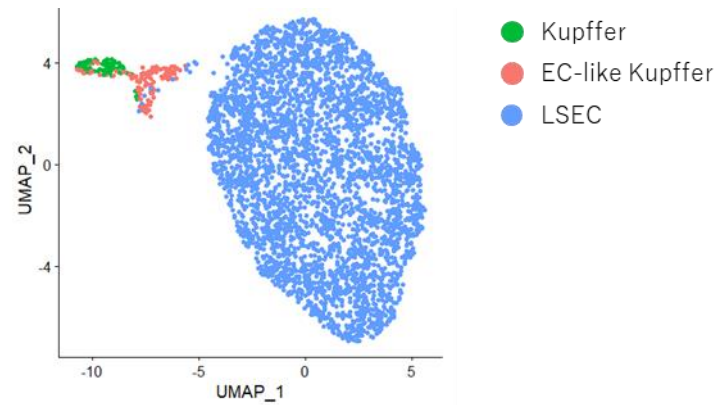
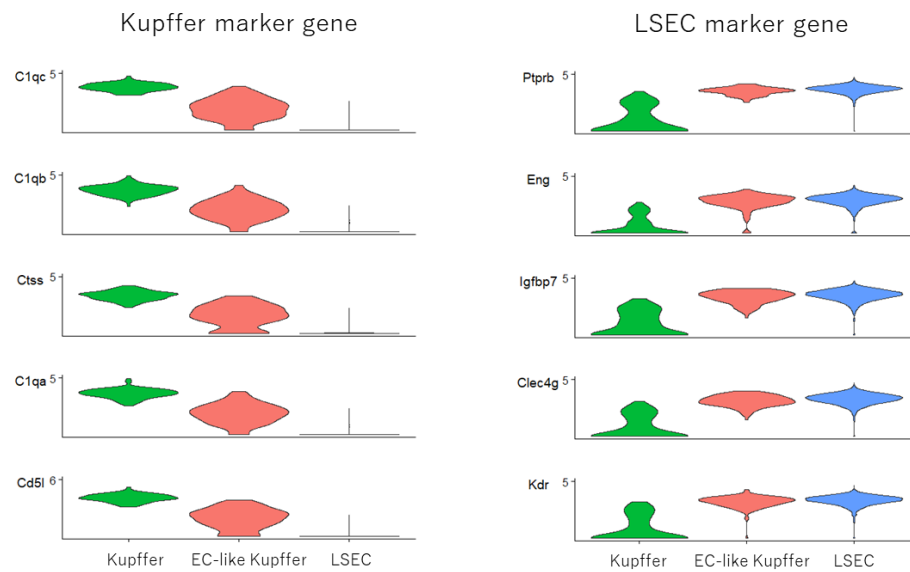
A**B**

Figure 28. Clustering of Kupffer cells and LSECs merged.

(A) UMAP for cell subtypes of merging Kupffer cells and LSECs data.

(B) Violin plot of the expression level of the top five marker genes of Kupffer cells or LSECs.

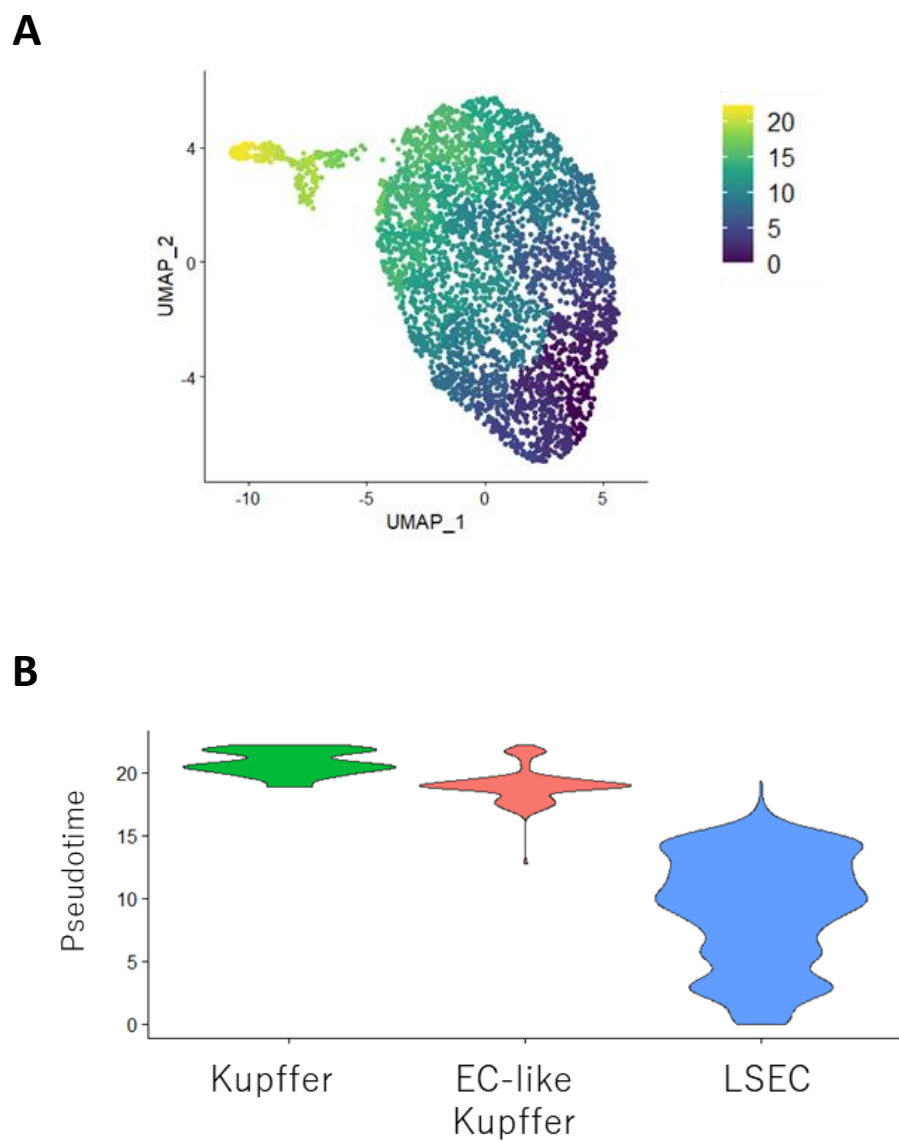


Figure 29. Pseudotime analysis of Kupffer cells and LSECs.

(A) The graph layout for pseudotime in trajectory inference.

(B) The violin plot of pseudotime.

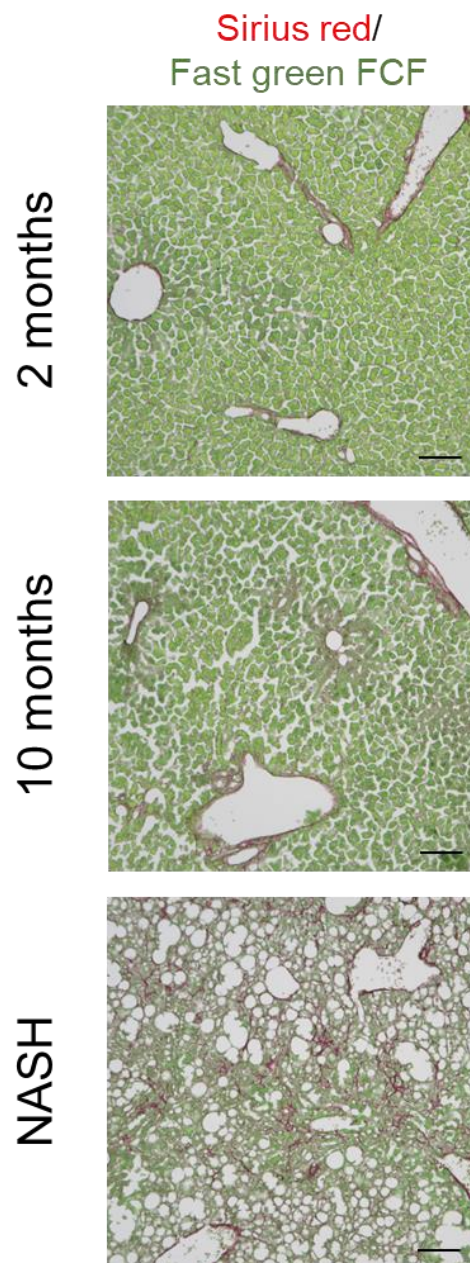


Figure 30. Validation of NASH model.

Sirius red/Fast green FCF staining for NASH as well as normal (2 months and 10 months) liver sections. scale bars: 100 mm.

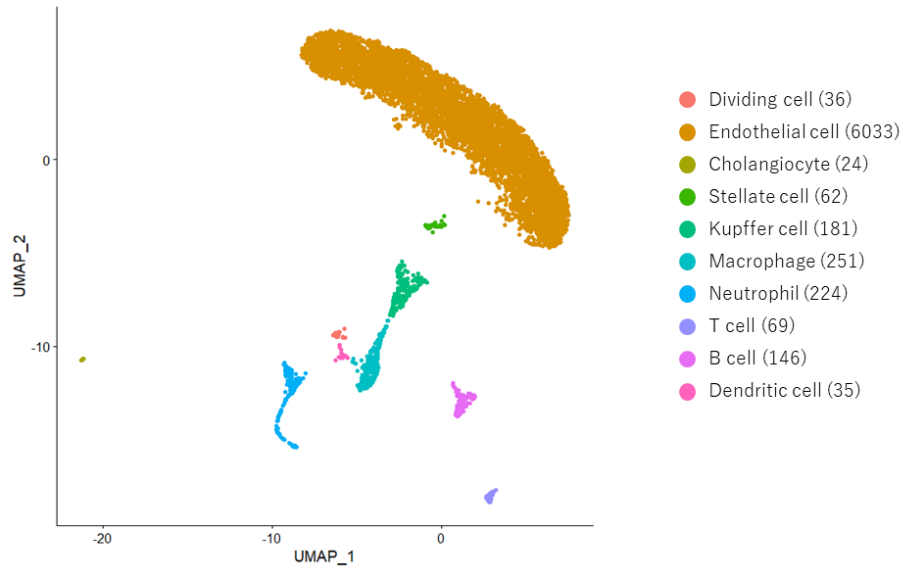
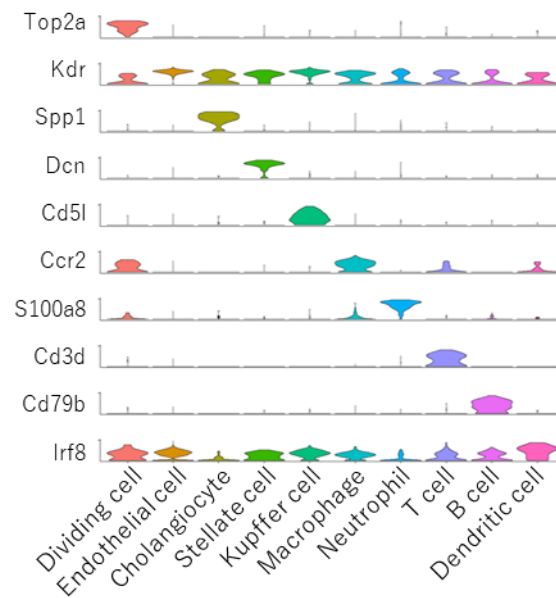
A**B**

Figure 31. Clustering of NASH liver cells.

(A) UMAP of NASH liver cell clusters containing 7,061 single NPC transcriptomes combined the non-separated sorted sample and the Tom⁺ sorted sample.

(B) The violin plot for the expression level of representative genes in each cell type.

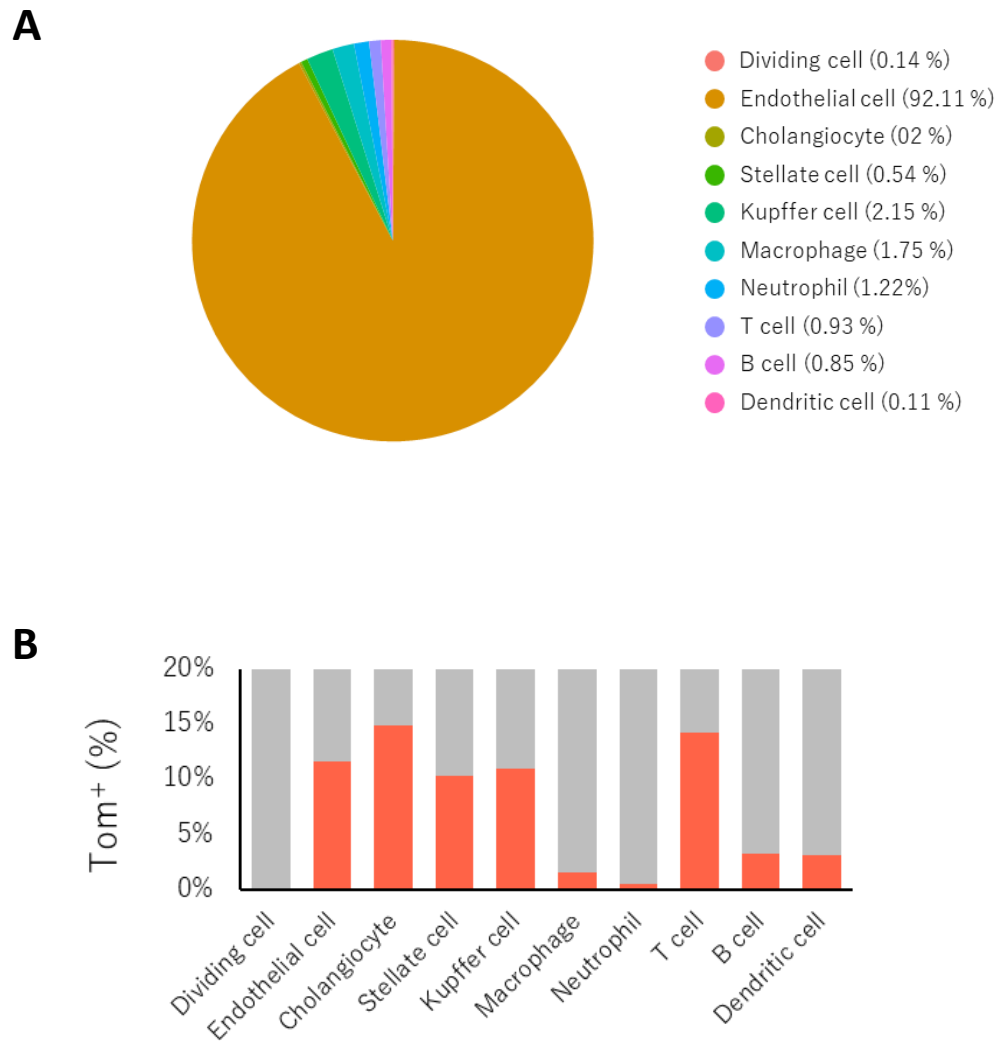


Figure 32. Composition of Tom⁺ cells in NASH liver.

(A) The cell-type composition of T Tom⁺ NPCs sorted from NASH liver.

(B) The percentage of Tom⁺ cells in each cell type was calculated on a non-separated sorted sample.

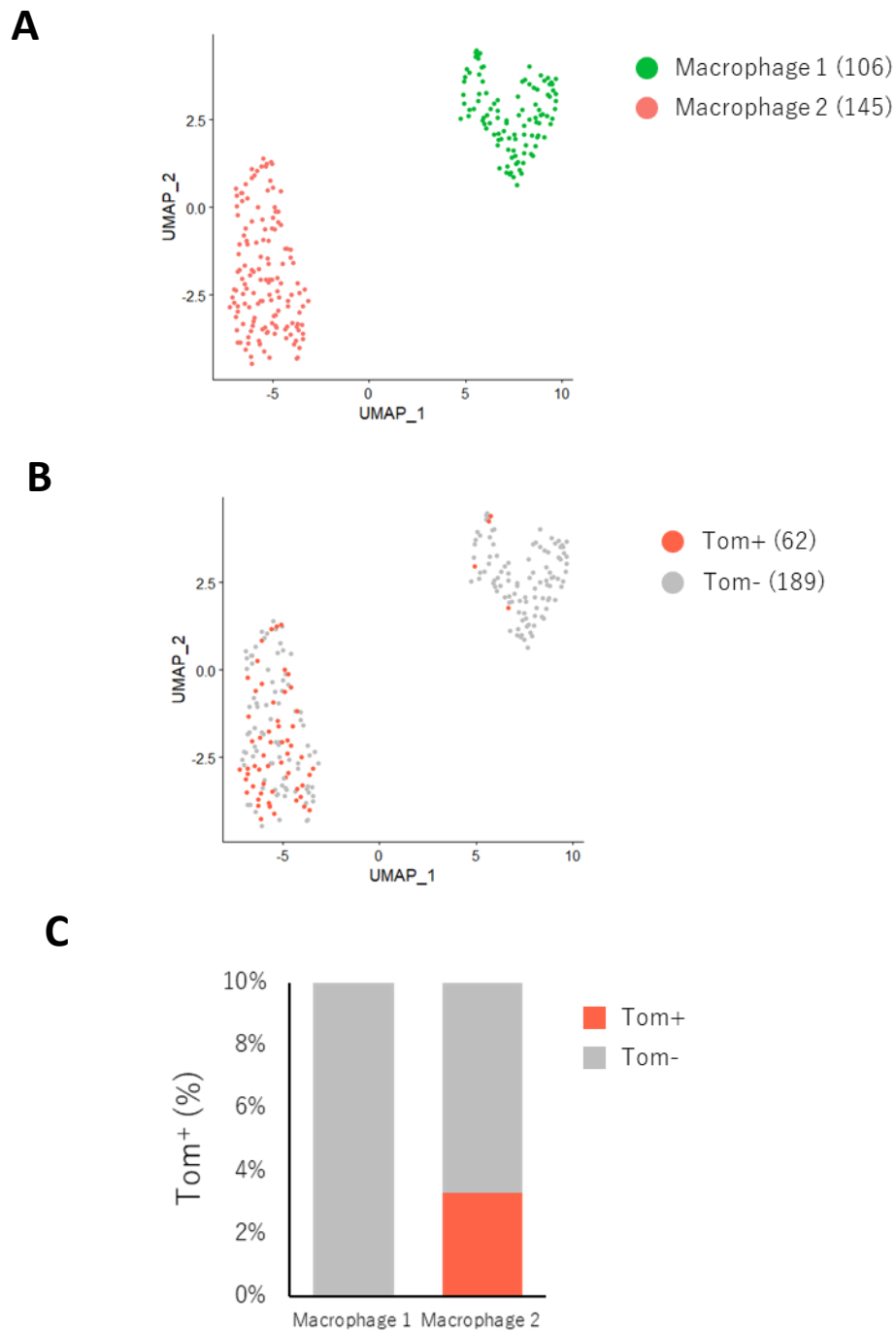
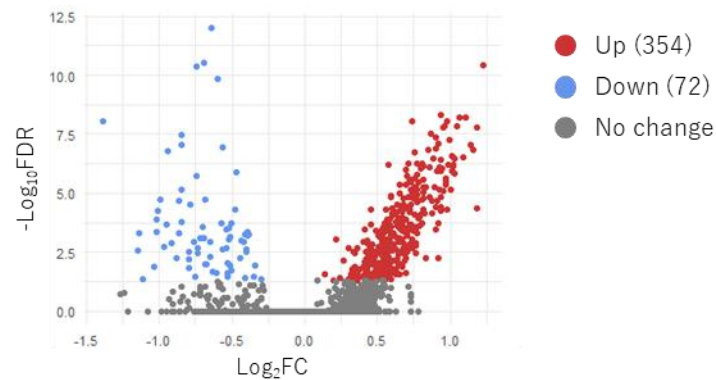


Figure 33. Clustering of Macrophages in NASH liver.

- (A) UMAP for subtype classification of Macrophages.
 (B) UMAP for distribution of Tom⁺ cells in Macrophages.
 (C) Percentage of Tom⁺ cells for Macrophage subtypes calculated by the non-separated sorted sample.

A



B

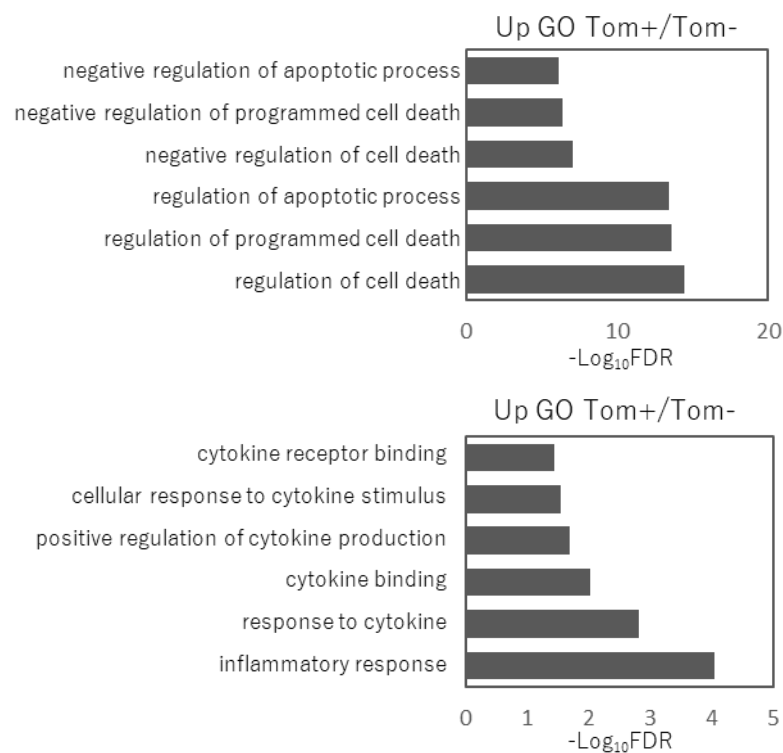


Figure 34. Validation of Tom⁺ and Tom⁻ Macrophages in NASH liver.

(A) DEGs of Tom⁺ compared with Tom⁻ Macrophages using volcano map. Red dots represent upregulated DEGs, blue dots represent downregulated DEGs, and gray dots represent non-DEGs. The DEGs were identified by FDR < 0.05 and Log₂FC > 0.1 or < -0.1.

(B) The enriched GO terms in upregulated DEGs.

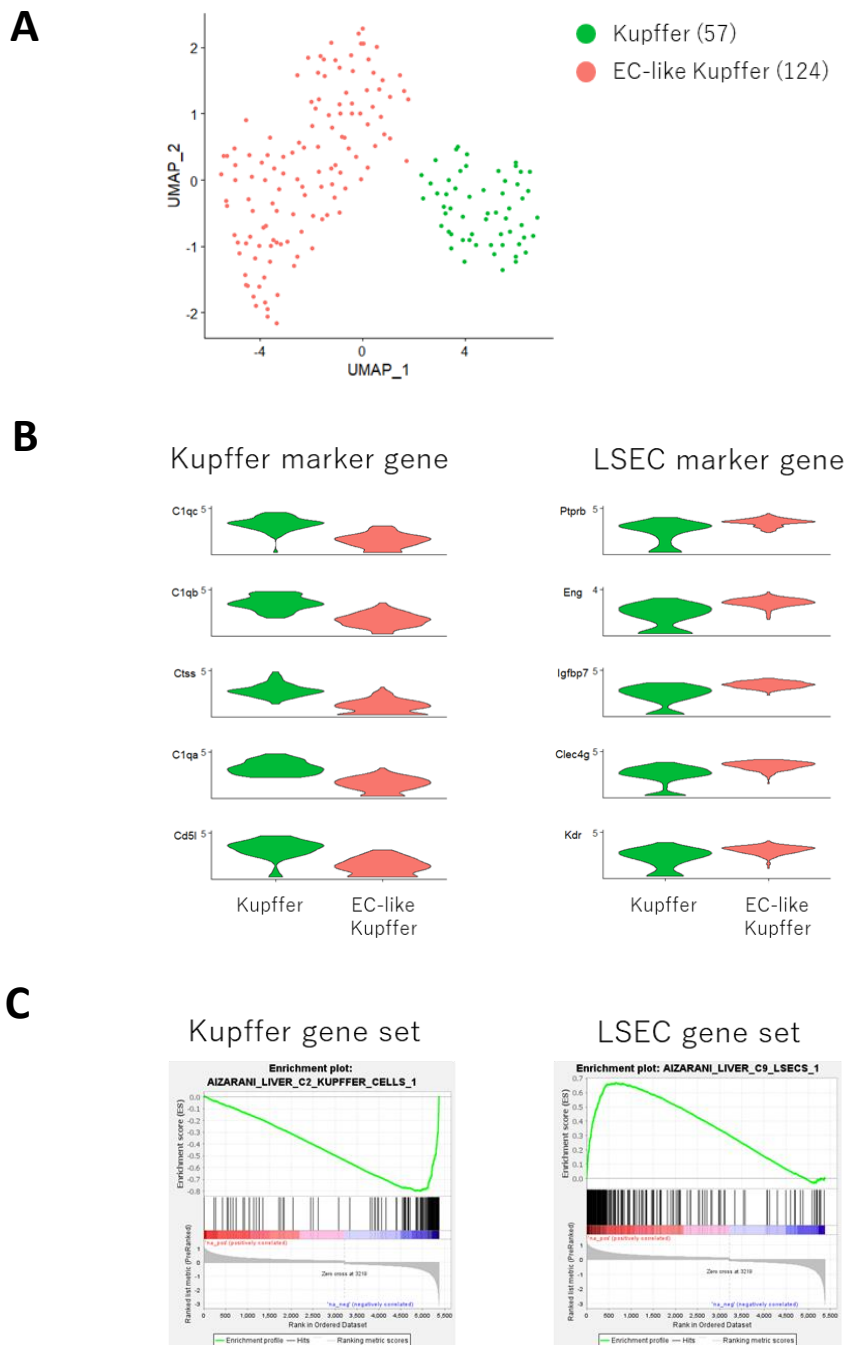


Figure 35. Differential expression of marker genes in NASH liver Kupffer cells.

- (A) UMAP for subtype classification of Kupffer cells.
- (B) Violin plot of the expression level of the top five marker genes of Kupffer cells or LSECs.
- (C) GSEA enrichment plots of cell type signature gene set of Kupffer cells or LSECs.

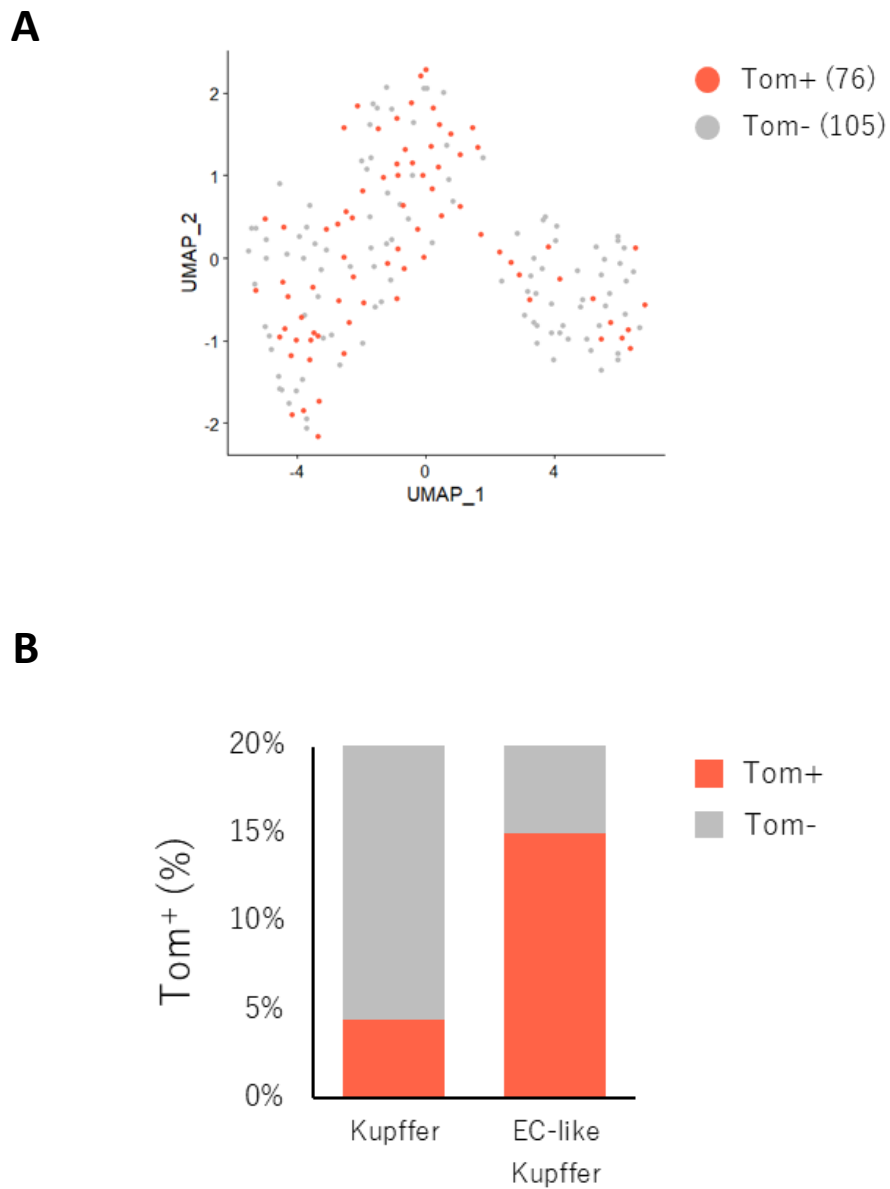


Figure 36. Distribution of Tom⁺ Kupffer cells in NASH liver.

(A) UMAP for distribution of Tom⁺ cells in Kupffer cells.

(B) Percentage of Tom⁺ cells for Kupffer cell subtypes calculated by the non-separated sorted sample.

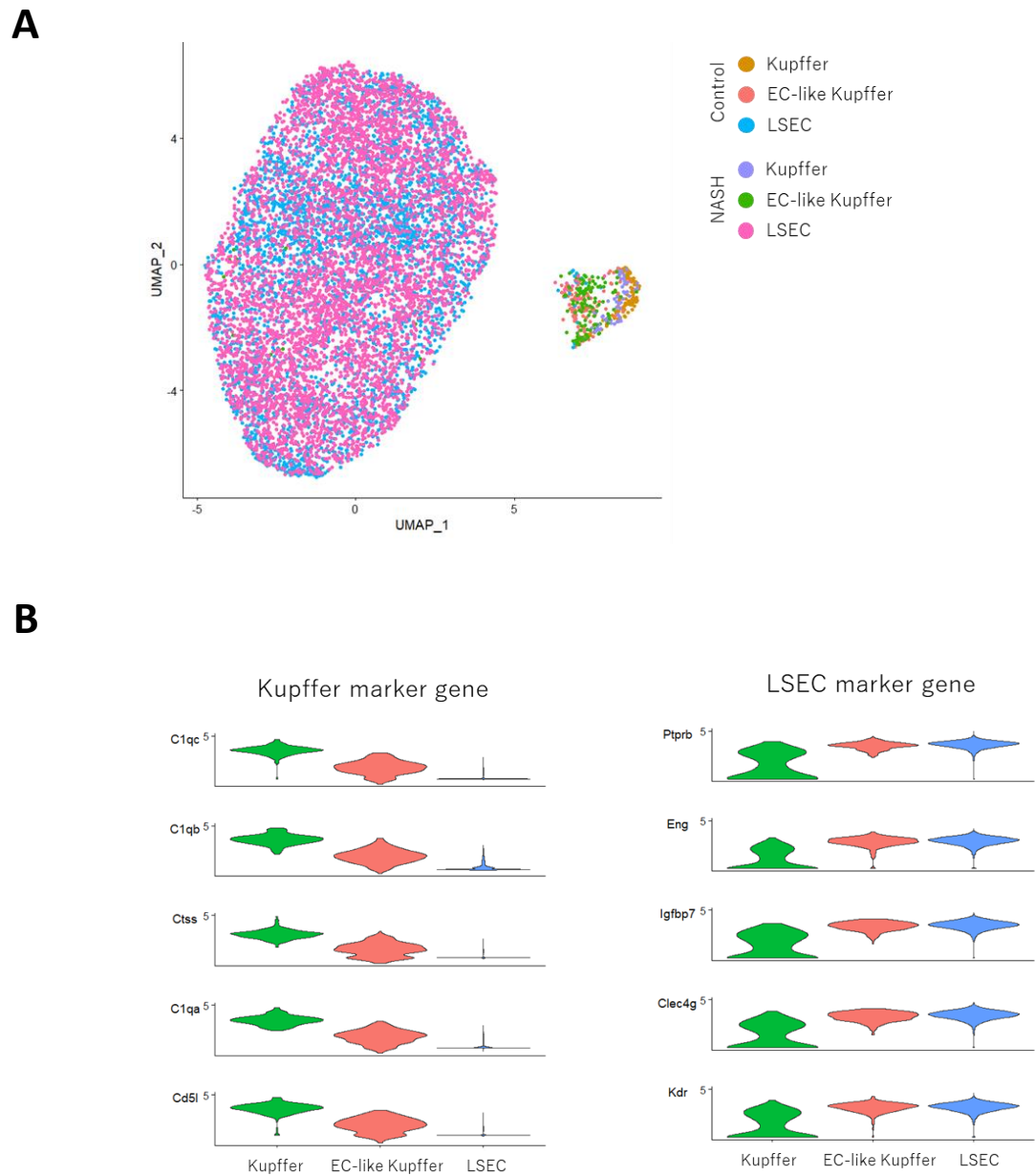


Figure 37. Clustering of Kupffer cells and LSECs integrated with normal and Nash liver.

- (A) UMAP for cell subtypes of merging Kupffer cells and LSECs data.
- (B) Violin plot of the expression level of the top five marker genes of Kupffer cells or LSECs.

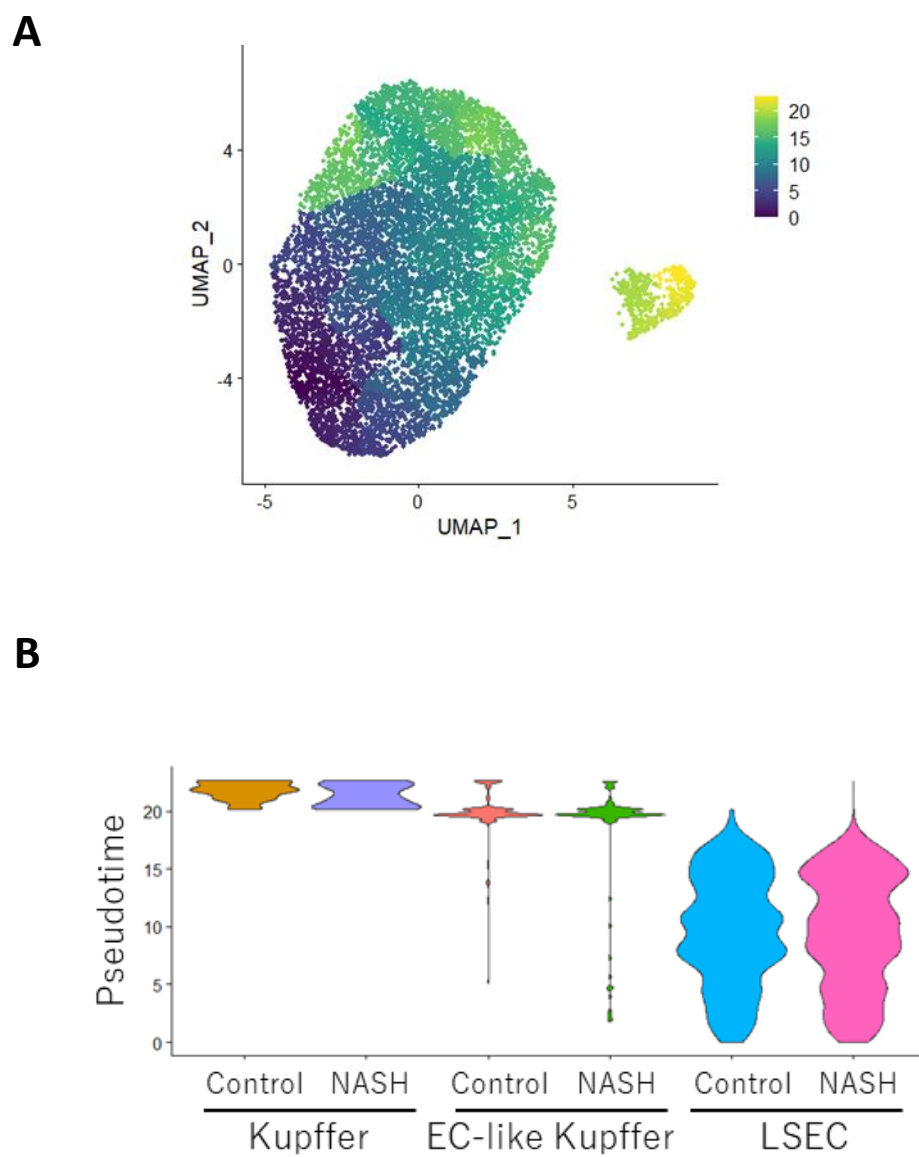


Figure 38. Pseudotime analysis of Kupffer cells and LSECs integrated with normal and NASH liver.

- (A) The graph layout for pseudotime in trajectory inference.
 (B) The violin plot of pseudotime.

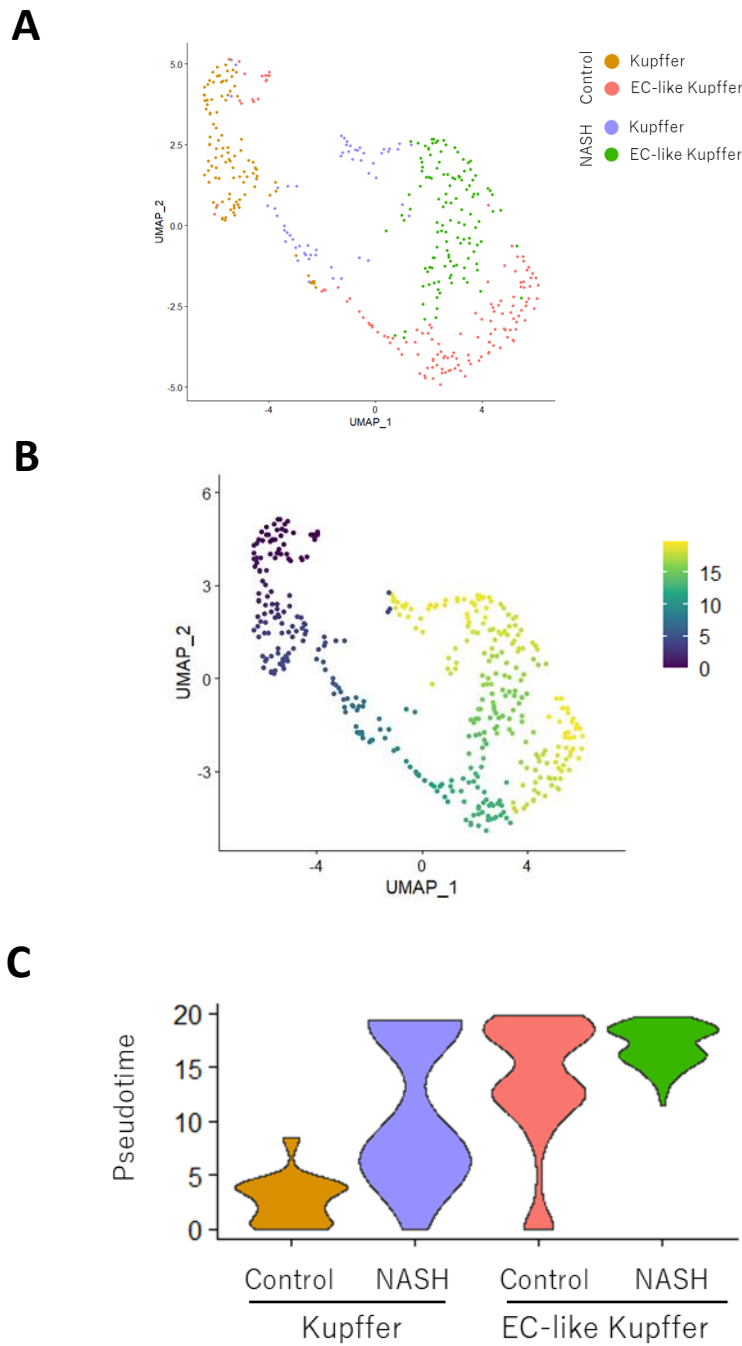
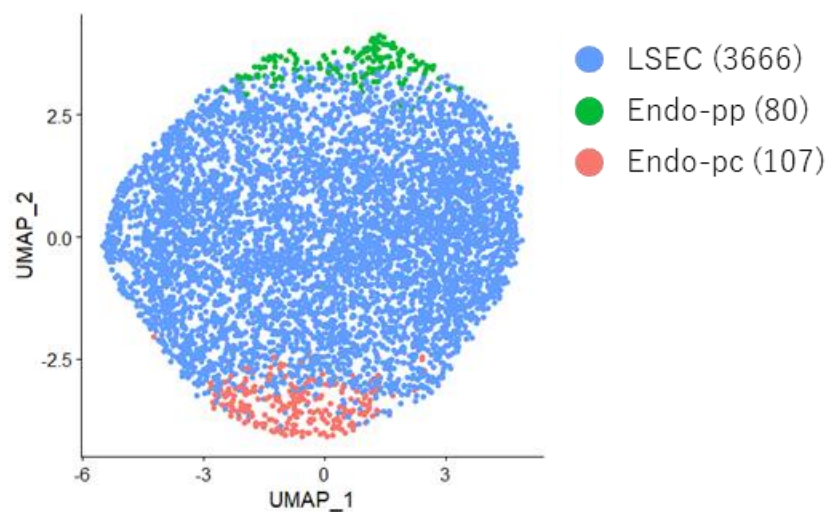


Figure 39. Pseudotime analysis of Kupffer cells integrated with normal and NASH liver data.

- (A) UMAP for cell subtypes of Kupffer cells.
- (B) The graph layout for pseudotime in trajectory inference.
- (C) The violin plot of pseudotime.

A



B

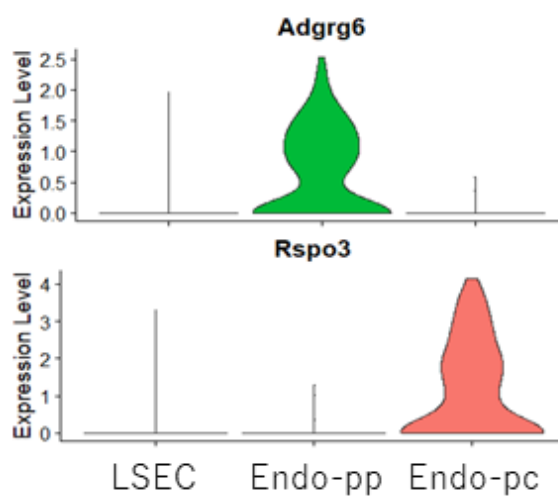


Figure 40. Clustering of endothelial cells in NASH liver.

(A) UMAP of endothelial cells in NASH liver.

(B) The violin plot for the expression level of representative genes in each subtype.

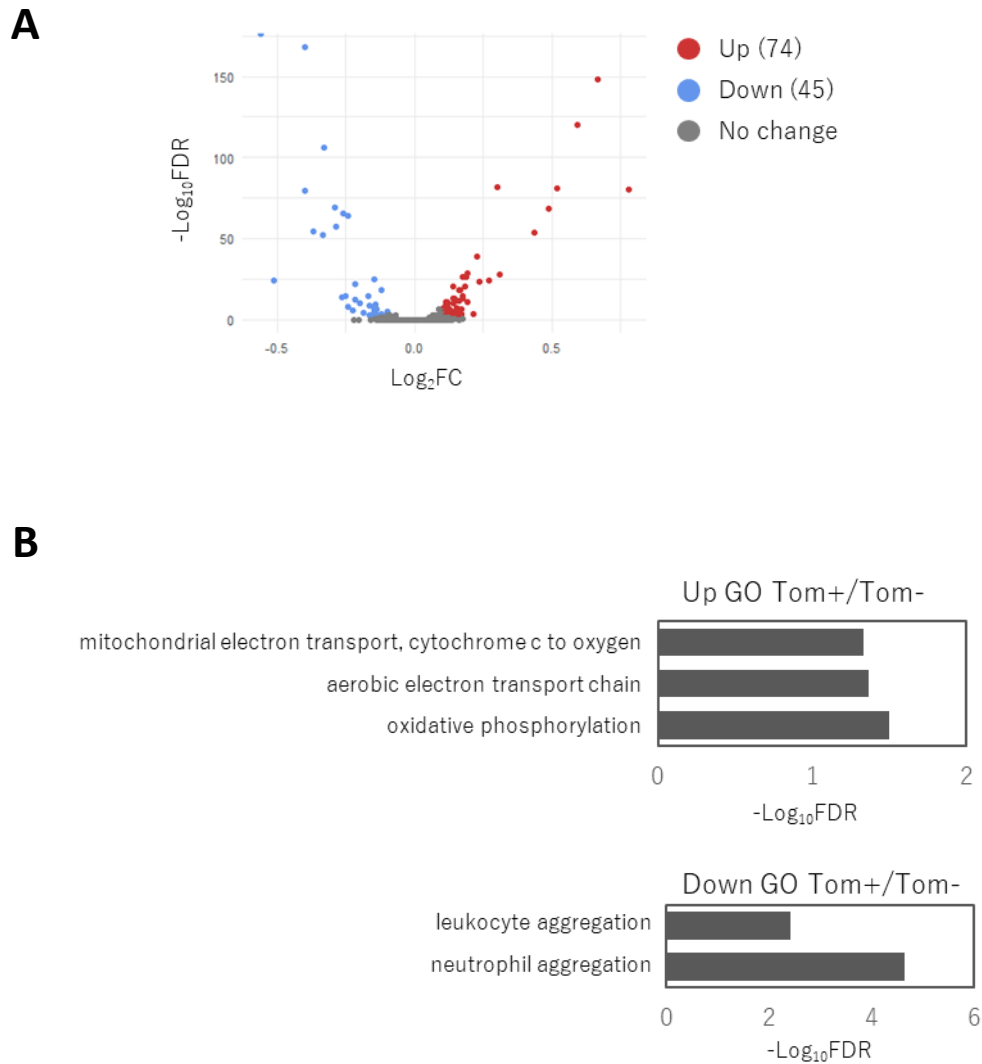


Figure 41. Validation of Tom⁺ and Tom⁻ LSECs in NASH liver.

- (A) DEGs of Tom⁺ compared with Tom⁻ LSECs using volcano map. Red dots represent upregulated DEGs, blue dots represent downregulated DEGs, and gray dots represent non-DEGs. The DEGs were identified by FDR < 0.05 and Log₂FC > 0.1 or < -0.1.
- (B) The enriched GO terms in upregulated or downregulated DEGs.

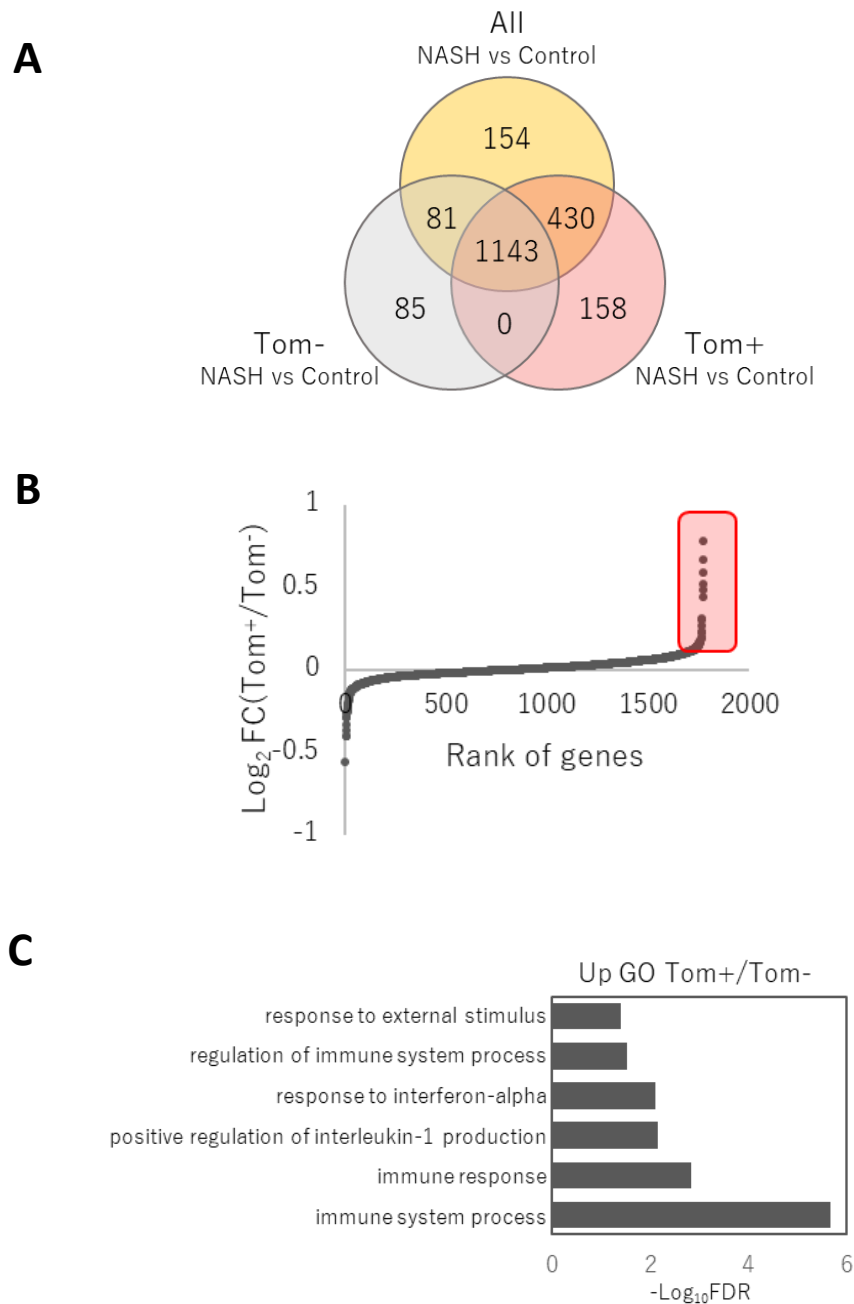


Figure 42. Clustering of Kupffer cells in NASH liver.

- (A) Venn diagram for intersection analysis of NASH-induced DEGs in the indicated comparisons.
- (B) The log₂ ratio of upregulated FCs in Tom⁺ to Tom⁻ LSECs in the total 1,808 NASH-induced genes. The red square represents genes with a log₂(FC ratio) greater than 0.1.
- (C) The enriched GO terms in upregulated DEGs.

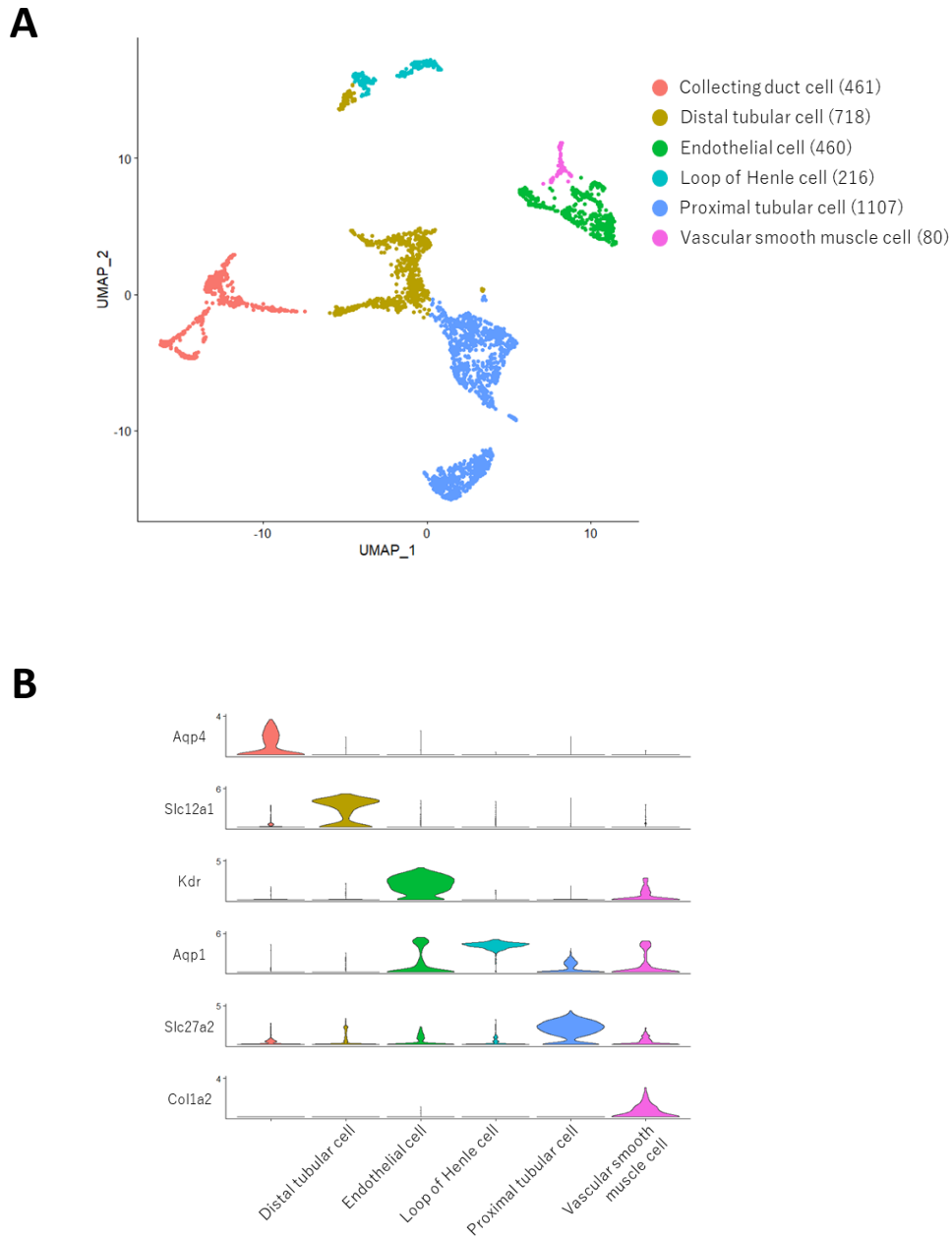


Figure 43. Clustering of kidney cells.

(A) UMAP of kidney cell clusters containing 3,042 single transcriptomes combined the non-separated sorted sample and the Tom⁺ sorted sample.

(B) The violin plot for the expression level of representative genes in each cell type.

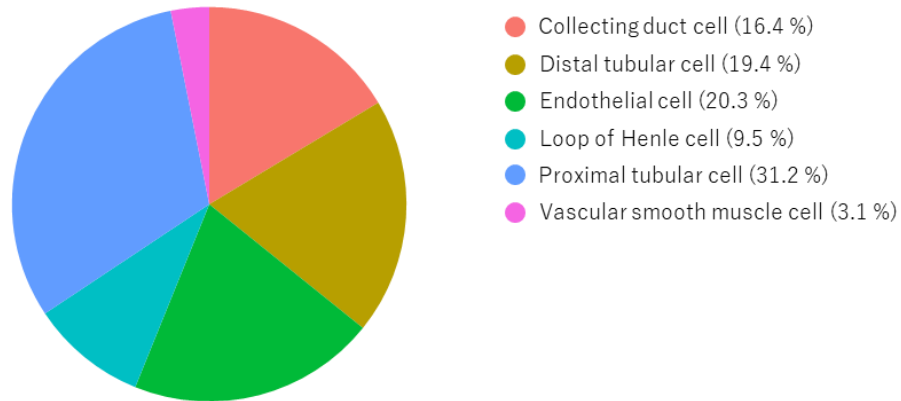
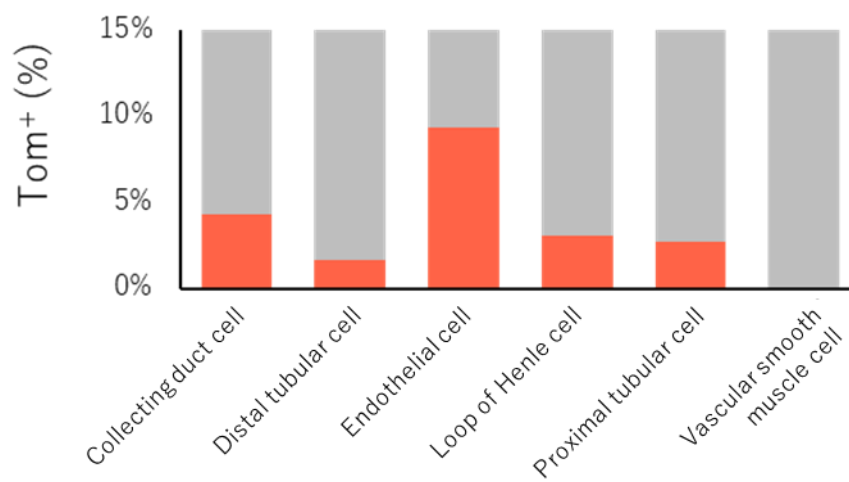
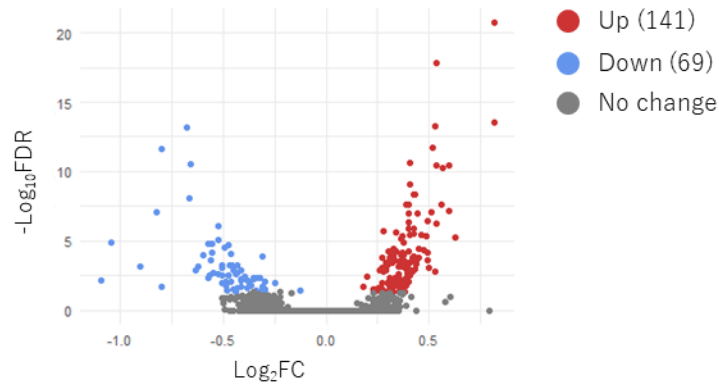
A**B**

Figure 44. Composition of Tom⁺ cells in the kidney.

(A) The cell-type composition of Tom⁺ cells sorted from kidney.

(B) The percentage of Tom⁺ cells in each cell type was calculated on a non-separated sorted sample.

A



B

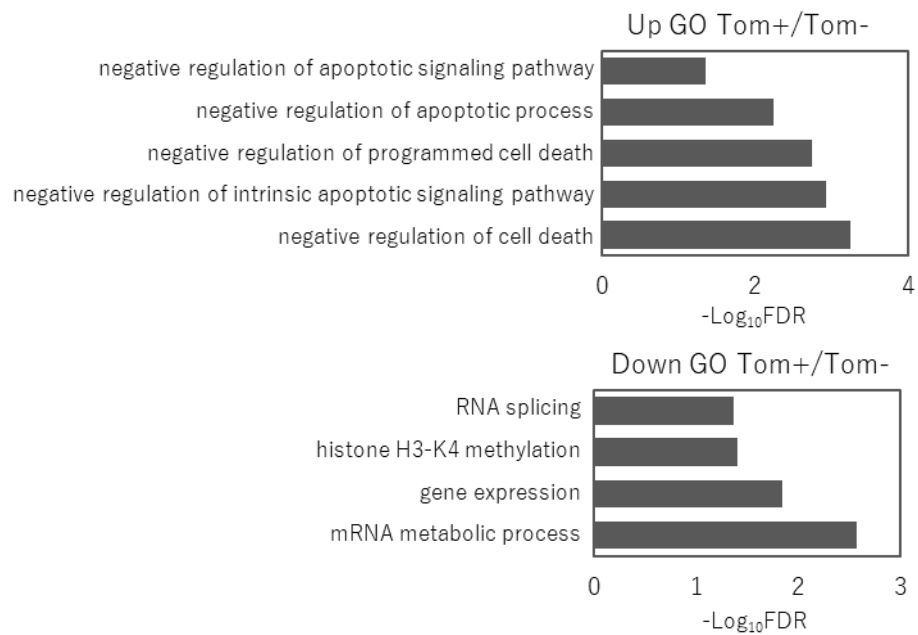
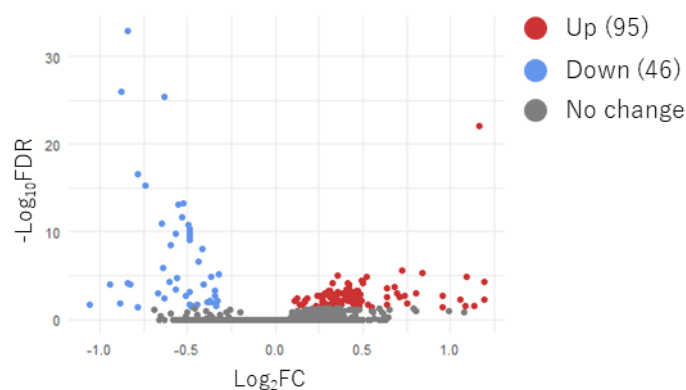


Figure 45. Validation of Tom⁺ and Tom⁻ proximal tubular cells in the kidney.

- (A) DEGs of Tom⁺ compared with Tom⁻ proximal tubular cells using volcano map. Red dots represent upregulated DEGs, blue dots represent downregulated DEGs, and gray dots represent non-DEGs. The DEGs were identified by FDR < 0.05 and Log₂FC > 0.1 or < -0.1.
- (B) The enriched GO terms in upregulated or downregulated DEGs.

A



B

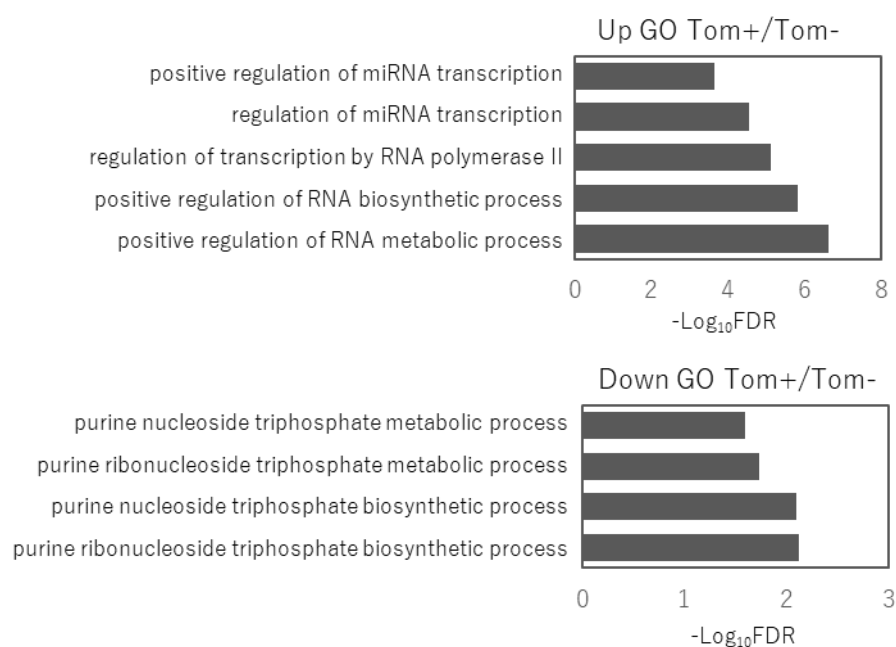
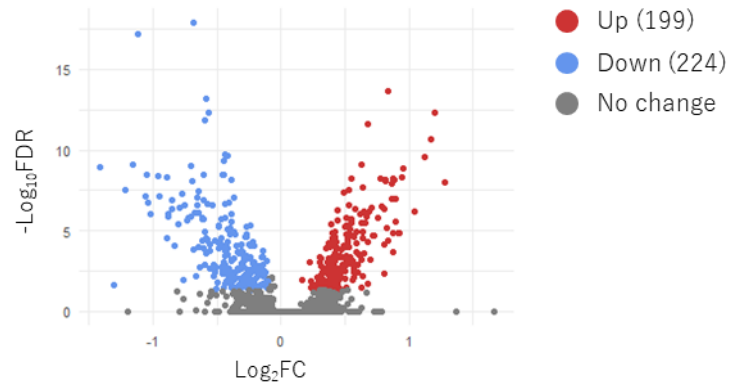


Figure 46. Validation of Tom⁺ and Tom⁻ distal tubular cells in the kidney.

- (A) DEGs of Tom⁺ compared with Tom⁻ distal tubular cells using volcano map. Red dots represent upregulated DEGs, blue dots represent downregulated DEGs, and gray dots represent non-DEGs. The DEGs were identified by FDR < 0.05 and Log₂FC > 0.1 or < -0.1.
- (B) The enriched GO terms in upregulated or downregulated DEGs.

A



B

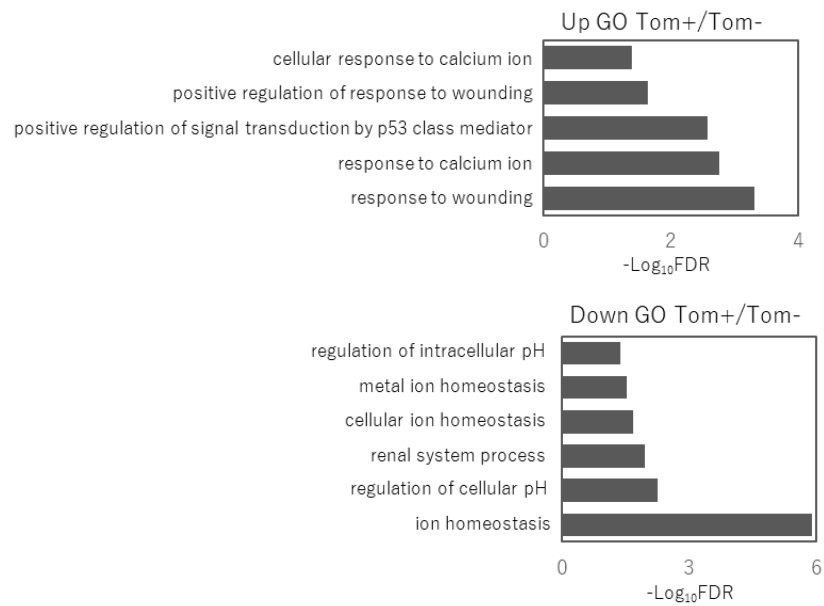


Figure 47. Validation of Tom⁺ and Tom⁻ collecting duct cells in the kidney.

(A) DEGs of Tom⁺ compared with Tom⁻ collecting duct cells using volcano map. Red dots represent upregulated DEGs, blue dots represent downregulated DEGs, and gray dots represent non-DEGs. The DEGs were identified by FDR < 0.05 and Log₂FC > 0.1 or < -0.1.

(B) The enriched GO terms in upregulated or downregulated DEGs.

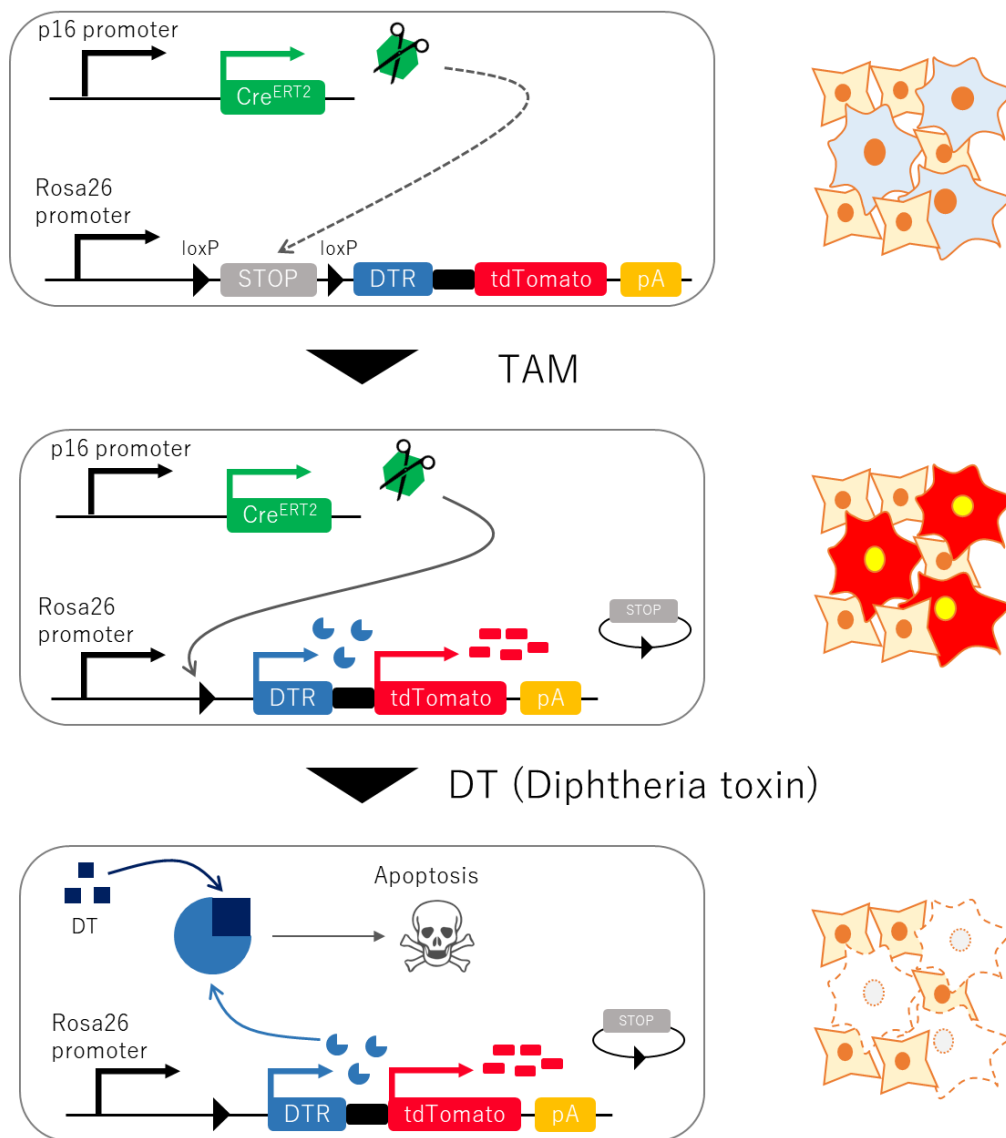


Figure 48. Scheme of p16-Cre^{ERT2}-DTR-tdTomato mice.

Tamoxifen treatment causes Cre^{ERT2} to be transported into the nucleus, where it recognizes the loxP sequence and removes the STOP sequence. This allows DTR and tdTomato to be expressed. These cells are induced apoptosis with DT administration.

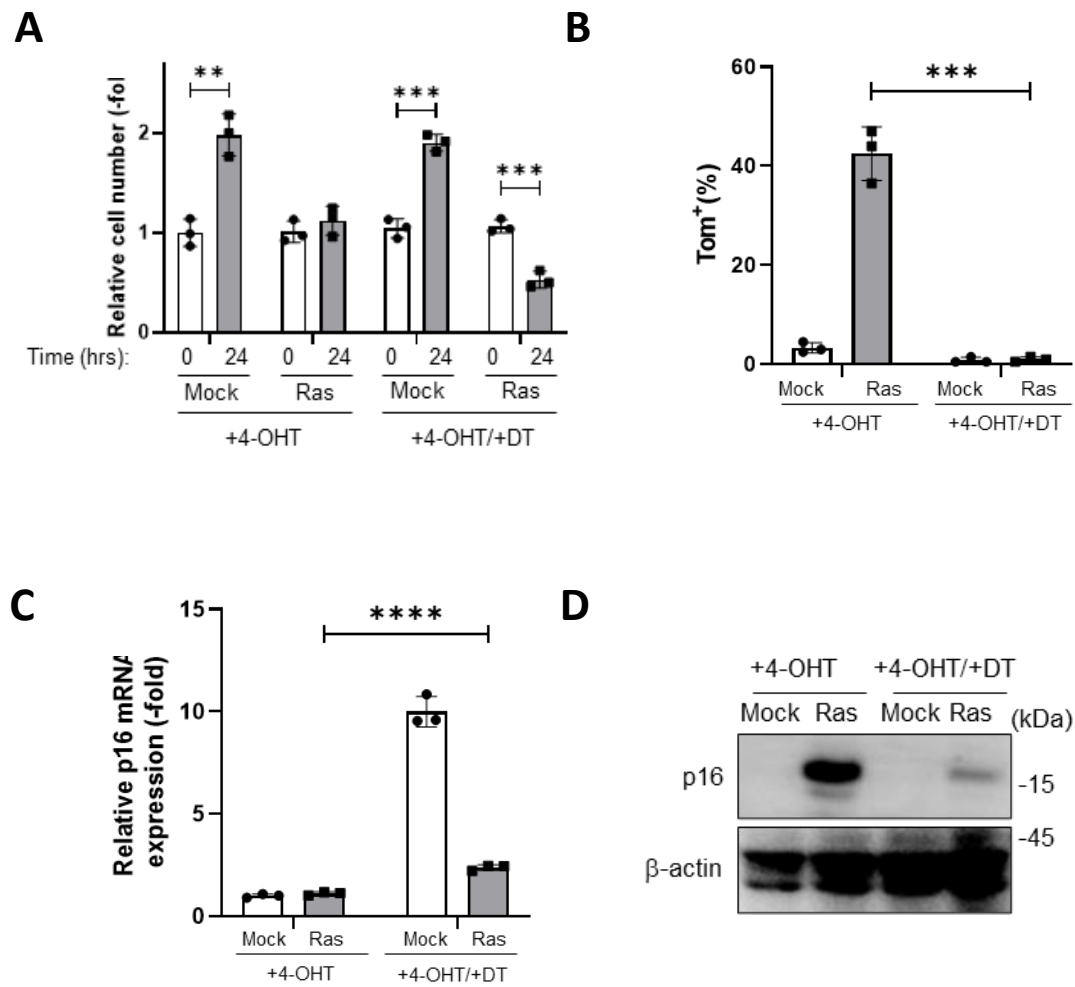


Figure 49. Removal of Tom⁺ cells in MEFs from p16-Cre^{ERT2}-DTR-tdTomato mice *in vitro*.

(A) Relative cell number of mock-treated (Mock) or oncogenic RAS (RAS) p16^{Ink4a}-DTR MEFs treated with 4-OHT (500 nM) for 3 days followed by the treatment with or without DT (1 mg/ml) for 0 and 24 hr.

(B) Proportions of Tom⁺ cells treated for 24 hrs as in (A).

(C) qPCR with the indicated primers of cells treated as in (B).

(D) Immunoblotting with the indicated antibodies of cells treated as in (B).

Data are presented as means \pm SD of independent experiments and analyzed with an Unpaired two-tailed Student's t-test. **p < 0.01, ***p < 0.001, ****p < 0.0001.

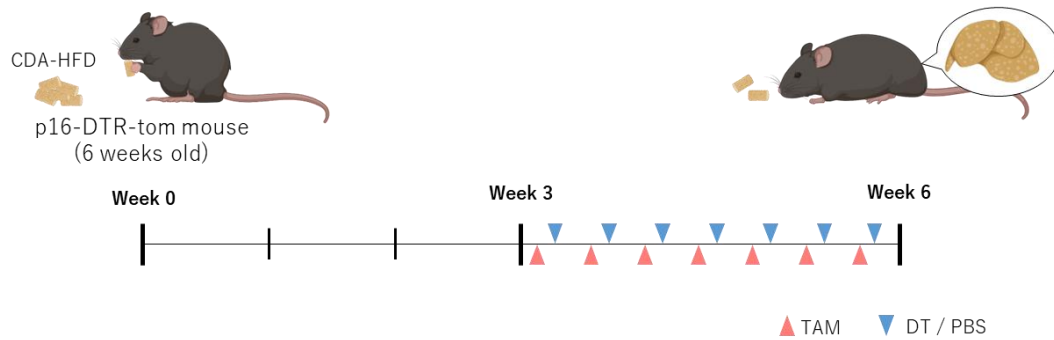
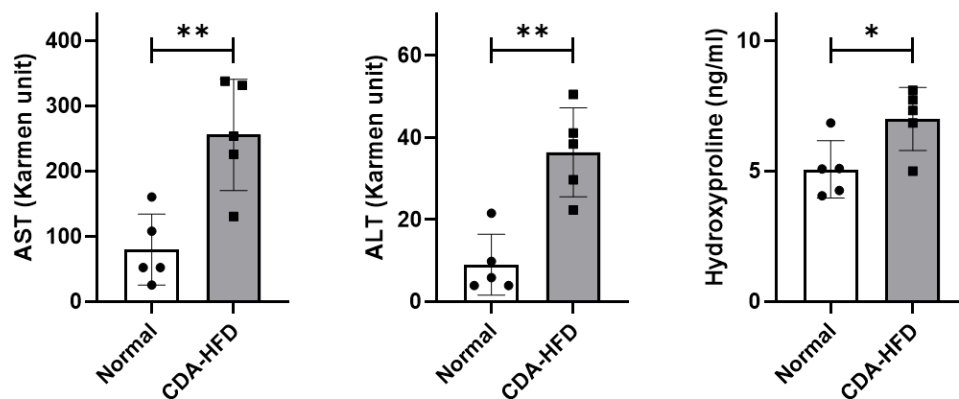
A**B**

Figure 50. Inducing NASH model in p16-Cre^{ERT2}-DTR-tdTomato mice.

- (A) Schematic representation of a removal protocol of Tom⁺ cells in p16-Cre^{ERT2}-DTR-tdTomato mice fed on CDA-HFD plus vehicle (n = 3) or diphtheria toxin (DT) (n = 3).
- (B) Levels of serum AST, ALT, and liver hydroxyproline in the indicated unit for normal diet or CDA-HFD treated mice for 6 weeks. (Karmen unit=0.482 IU/L). Data are presented as means ± SD of independent experiments and analyzed with an Unpaired two-tailed Student's t-test. *p < 0.05, **p < 0.01.

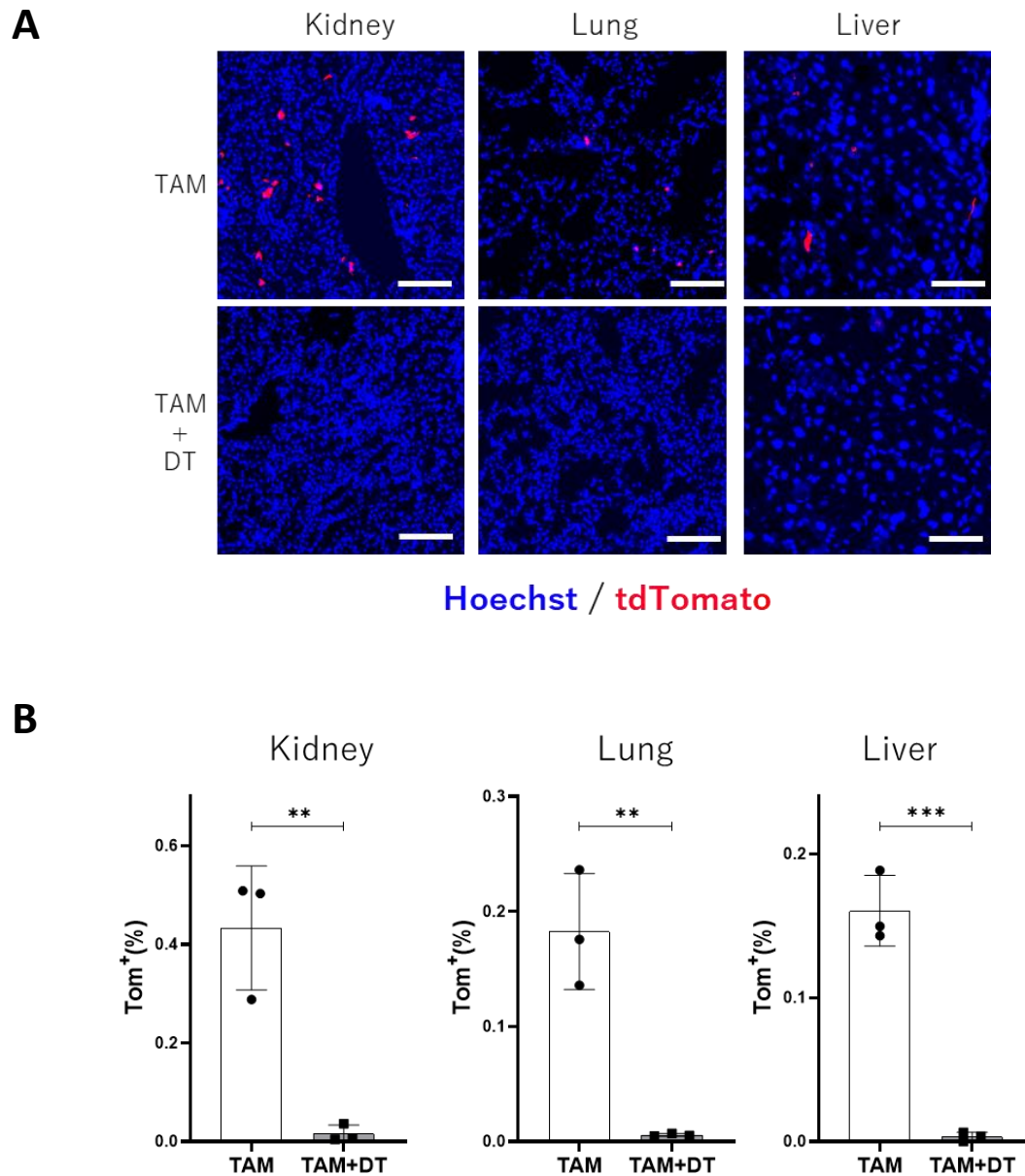
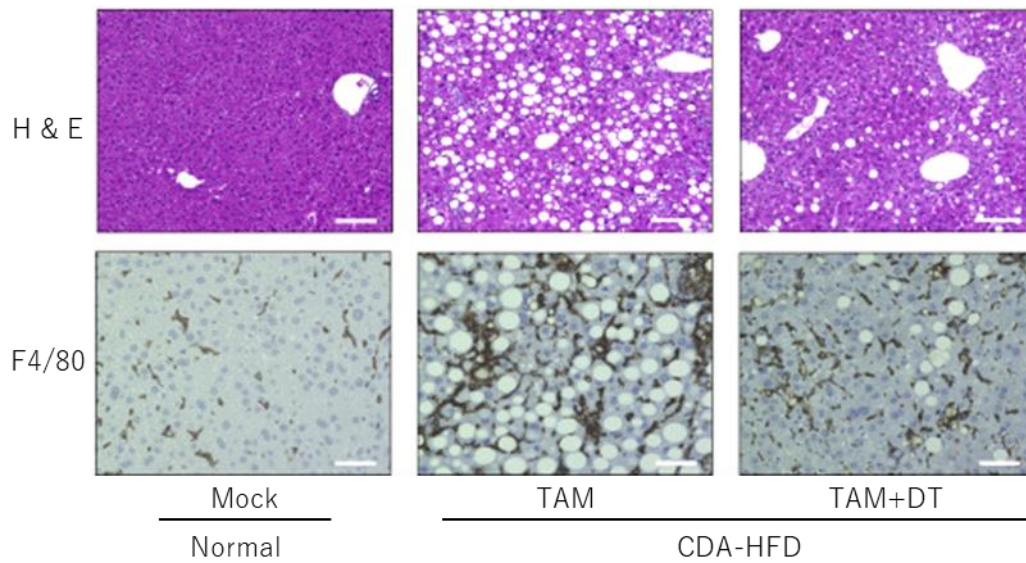


Figure 51. Validation of removal Tom⁺ cells in p16-Cre^{ERT2}-DTR-tdTomato mice.

- (A) Fluorescent image of p16-Cre^{ERT2}-DTR-tdTomato mice in the indicated organs administrated TAM with or without DT. The scheme followed as Figure 50 (A). Scale bars, 100 μ m.
- (B) Percentage of Tom⁺ cells determined in the indicated organs. Data are presented as means \pm SD of independent experiments and analyzed with an Unpaired two-tailed Student's t-test. **p < 0.01, ***p < 0.001.

A



B

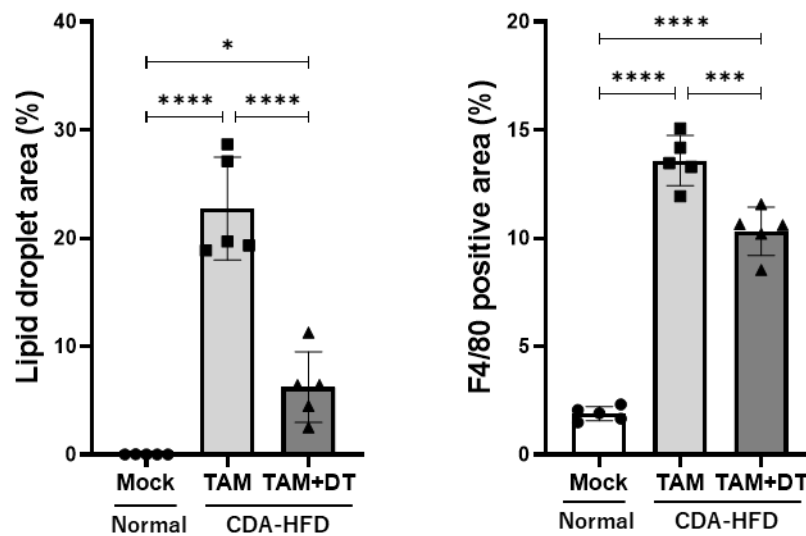


Figure 52. Effect of removal p16^{high} cells in NASH model.

(A) H&E (upper panel) and F4/80 IHC (lower panel) staining for liver sections with the indicated treatment. Scale bars, 100 μ m (H&E) and 50 μ m (F4/80).

The percentage of lipid droplets (left) and F4/80 staining (right) of positive areas in liver sections with the indicated treatment. Data are presented as means \pm SD of independent experiments and analyzed with one-way ANOVA with Tukey's multiple comparisons post hoc test. * $p < 0.05$, *** $p < 0.001$, **** $p < 0.0001$.

Table 1. Top 10 genes upregulated in kidney Tom⁺ cells.

| | Proximal tubular cell | Distal tubular cell | Collecting duct cell | Endothelial cell |
|----|-----------------------|---------------------|----------------------|------------------|
| 1 | Lars2 | Lars2 | Lars2 | Lars2 |
| 2 | Chchd2 | Clic4 | Tmsb4x | - |
| 3 | Spp2 | Bst1 | Cdh16 | - |
| 4 | Hint1 | Ldlr | Fxyd4 | - |
| 5 | Gatm | Parm1 | Aqp2 | - |
| 6 | Ftl1 | Aqp1 | Mal | - |
| 7 | Uqcrh | Zfp36 | Igfbp7 | - |
| 8 | Nme1 | Spon1 | Npnt | - |
| 9 | Cyba | Akap12 | Dbndd2 | - |
| 10 | Cox4i1 | Lypd2 | Ahnak | - |

Chapter 6. Reference

- Aguayo-Mazzucato, C., et al. (2019). "Acceleration of β cell aging determines diabetes and senolysis improves disease outcomes." Cell Metabolism **30**(1): 129-142. e124.
- Aravinthan, A. D. and G. J. Alexander (2016). "Senescence in chronic liver disease: Is the future in aging?" Journal of hepatology **65**(4): 825-834.
- Baar, M. P., et al. (2017). "Targeted apoptosis of senescent cells restores tissue homeostasis in response to chemotoxicity and aging." Cell **169**(1): 132-147. e116.
- Baker, D. J., et al. (2016). "Naturally occurring p16^{Ink4a}-positive cells shorten healthy lifespan." Nature **530**(7589): 184-189.
- Baker, D. J., et al. (2011). "Clearance of p16^{Ink4a}-positive senescent cells delays ageing-associated disorders." Nature **479**(7372): 232-236.
- Baumer, S., et al. (2006). "Vascular endothelial cell-specific phosphotyrosine phosphatase (VE-PTP) activity is required for blood vessel development." Blood **107**(12): 4754-4762.
- Bonnardel, J., et al. (2019). "Stellate cells, hepatocytes, and endothelial cells imprint the Kupffer cell identity on monocytes colonizing the liver macrophage

niche." Immunity **51**(4): 638-654. e639.

- Boone, P. G., et al. (2019). "A cancer rainbow mouse for visualizing the functional genomics of oncogenic clonal expansion." Nature Communications **10**(1): 1-15.
- Buch, T., et al. (2005). "A Cre-inducible diphtheria toxin receptor mediates cell lineage ablation after toxin administration." Nature Methods **2**(6): 419-426.
- Burd, C. E., et al. (2013). "Monitoring tumorigenesis and senescence *in vivo* with a p16^{Ink4a}-luciferase model." Cell **152**(1-2): 340-351.
- Calvente, C. J., et al. (2019). "Neutrophils contribute to spontaneous resolution of liver inflammation and fibrosis via microRNA-223." The Journal of clinical investigation **129**(10): 4091-4109.
- Campisi, J. and F. d'Adda di Fagagna (2007). "Cellular senescence: when bad things happen to good cells." Nature Reviews Molecular Cell Biology **8**(9): 729-740.
- Cao, J., et al. (2019). "The single-cell transcriptional landscape of mammalian organogenesis." Nature **566**(7745): 496-502.
- Chang, J., et al. (2016). "Clearance of senescent cells by ABT263 rejuvenates aged hematopoietic stem cells in mice." Nature Medicine **22**(1): 78-83.
- Childs, B. G., et al. (2015). "Cellular senescence in aging and age-related disease: from mechanisms to therapy." Nature Medicine **21**(12): 1424-1435.

- Clausen, B., et al. (1999). "Conditional gene targeting in macrophages and granulocytes using LysMcre mice." Transgenic research 8(4): 265-277.
- Collado, M., et al. (2007). "Cellular senescence in cancer and aging." Cell 130(2): 223-233.
- Coppé, J.-P., et al. (2010). "The senescence-associated secretory phenotype: the dark side of tumor suppression." Annual review of pathology 5: 99.
- Correia-Melo, C. and J. F. Passos (2015). "Mitochondria: are they causal players in cellular senescence?" Biochimica et Biophysica Acta (BBA)-Bioenergetics 1847(11): 1373-1379.
- De Cecco, M., et al. (2019). "L1 drives IFN in senescent cells and promotes age-associated inflammation." Nature 566(7742): 73-78.
- de Mochel, N. R., et al. (2020). "Sentinel p16^{Ink4a} cells in the basement membrane form a reparative niche in the lung." bioRxiv.
- Delfarah, A., et al. (2019). "Inhibition of nucleotide synthesis promotes replicative senescence of human mammary epithelial cells." Journal of Biological Chemistry 294(27): 10564-10578.
- Demaria, M., et al. (2014). "An essential role for senescent cells in optimal wound healing through secretion of PDGF-AA." Developmental cell 31(6): 722-733.
- Dimri, G. P., et al. (1995). "A biomarker that identifies senescent human cells in

- culture and in aging skin *in vivo*." Proceedings of the National Academy of Sciences **92**(20): 9363-9367.
- Docherty, M.-H., et al. (2019). "Cellular senescence in the kidney." Journal of the American Society of Nephrology **30**(5): 726-736.
 - El-Nachef, D., et al. (2020). "A rainbow reporter tracks single cells and reveals heterogeneous cellular dynamics among pluripotent stem cells and their differentiated derivatives." Stem cell reports **15**(1): 226-241.
 - Faure-André, G., et al. (2008). "Regulation of dendritic cell migration by CD74, the MHC class II-associated invariant chain." Science **322**(5908): 1705-1710.
 - Fernandez-Marcos, P. J. and M. Serrano (2016). "Mitochondrial damage induces senescence with a twisted arm." Cell Metabolism **23**(2): 229-230.
 - Freund, A., et al. (2012). "Lamin B1 loss is a senescence-associated biomarker." Molecular biology of the cell **23**(11): 2066-2075.
 - Gorenne, I., et al. (2006). "Vascular smooth muscle cell senescence in atherosclerosis." Cardiovascular research **72**(1): 9-17.
 - Gorgoulis, V., et al. (2019). "Cellular senescence: defining a path forward." Cell **179**(4): 813-827.
 - Grün, D. and A. van Oudenaarden (2015). "Design and analysis of single-cell sequencing experiments." Cell **163**(4): 799-810.

- Grosse, L., et al. (2020). "Defined p16^{High} senescent cell types are indispensable for mouse healthspan." Cell Metabolism **32**(1): 87-99. e86.
- Hao, Y., et al. (2021). "Integrated analysis of multimodal single-cell data." Cell **184**(13): 3573-3587. e3529.
- He, S. and N. E. Sharpless (2017). "Senescence in health and disease." Cell **169**(6): 1000-1011.
- Huang, X., et al. (2021). "Single-cell transcriptional profiling reveals sex and age diversity of gene expression in mouse endothelial cells." Frontiers in Genetics **12**: 590377.
- Iwasaki, K., et al. (2018). "Ablation of central serotonergic neurons decreased REM sleep and attenuated arousal response." Frontiers in neuroscience **12**: 535.
- Johmura, Y., et al. (2014). "Necessary and sufficient role for a mitosis skip in senescence induction." Molecular Cell **55**(1): 73-84.
- Johmura, Y., et al. (2021). "Senolysis by glutaminolysis inhibition ameliorates various age-associated disorders." Science **371**(6526): 265-270.
- Johnson, S. C., et al. (2013). "mTOR is a key modulator of ageing and age-related disease." Nature **493**(7432): 338-345.
- Kamimoto, K., et al. (2020). "Multidimensional imaging of liver injury repair in mice reveals fundamental role of the ductular reaction." Communications biology

3(1): 1-10.

- Kan, C., et al. (2012). "Endothelial cell dysfunction and cytoskeletal changes associated with repression of p16^{Ink4a} during immortalization." Oncogene **31**(46): 4815-4827.
- Kang, H. M., et al. (2015). "Defective fatty acid oxidation in renal tubular epithelial cells has a key role in kidney fibrosis development." Nature Medicine **21**(1): 37-46.
- Kaplon, J., et al. (2013). "A key role for mitochondrial gatekeeper pyruvate dehydrogenase in oncogene-induced senescence." Nature **498**(7452): 109-112.
- Karin, O., et al. (2019). Senescent cell turnover slows with age providing an explanation for the Gompertz law. Nat Commun **10**: 5495.
- Kazankov, K., et al. (2019). "The role of macrophages in nonalcoholic fatty liver disease and nonalcoholic steatohepatitis." Nature Reviews Gastroenterology & Hepatology **16**(3): 145-159.
- Kester, L. and A. van Oudenaarden (2018). "Single-cell transcriptomics meets lineage tracing." Cell stem cell **23**(2): 166-179.
- Krizhanovsky, V., et al. (2008). "Senescence of activated stellate cells limits liver fibrosis." Cell **134**(4): 657-667.
- Kubota, S. I., et al. (2017). "Whole-body profiling of cancer metastasis with single-

cell resolution." Cell Reports **20**(1): 236-250.

- Kuilman, T., et al. (2010). "The essence of senescence." Genes & development **24**(22): 2463-2479.
- Le, O. N., et al. (2010). "Ionizing radiation-induced long-term expression of senescence markers in mice is independent of p53 and immune status." Aging Cell **9**(3): 398-409.
- Leon, K. E. and K. M. Aird (2019). "Jumonji C demethylases in cellular senescence." Genes **10**(1): 33.
- Liu, J.-Y., et al. (2019). "Cells exhibiting strong p16^{Ink4a} promoter activation *in vivo* display features of senescence." Proceedings of the National Academy of Sciences **116**(7): 2603-2611.
- Lujambio, A., et al. (2013). "Non-cell-autonomous tumor suppression by p53." Cell **153**(2): 449-460.
- Marongiu, F., et al. (2016). "Aging promotes neoplastic disease through effects on the tissue microenvironment." Aging **8**(12): 3390-3399.
- Martínez-Zamudio, R. I., et al. (2020). "AP-1 imprints a reversible transcriptional programme of senescent cells." Nature Cell Biology **22**(7): 842-855.
- Matsumoto, K., et al. (2019). "Advanced CUBIC tissue clearing for whole-organ cell profiling." Nature protocols **14**(12): 3506-3537.

- Matsumoto, M., et al. (2013). "An improved mouse model that rapidly develops fibrosis in non-alcoholic steatohepatitis." International journal of experimental pathology **94**(2): 93-103.
- McInnes, L., et al. (2018). "Umap: Uniform manifold approximation and projection for dimension reduction." arXiv preprint arXiv:1802.03426.
- Megquier, K., et al. (2019). "Comparative Genomics Reveals Shared Mutational Landscape in Canine Hemangiosarcoma and Human AngiosarcomaGenomics of Canine Hemangiosarcoma and Human Angiosarcoma." Molecular Cancer Research **17**(12): 2410-2421.
- Min, K. W., et al. (2018). "Profiling of m6A RNA modifications identified an age-associated regulation of AGO 2 mRNA stability." Aging Cell **17**(3): e12753.
- Minamino, T. and I. Komuro (2007). "Vascular cell senescence: contribution to atherosclerosis." Circulation Research **100**(1): 15-26.
- Minamino, T., et al. (2009). "A crucial role for adipose tissue p53 in the regulation of insulin resistance." Nature Medicine **15**(9): 1082-1087.
- Nakamura, T., et al. (2019). "Iron homeostasis and iron-regulated ROS in cell death, senescence and human diseases." Biochimica et Biophysica Acta (BBA)-General Subjects **1863**(9): 1398-1409.
- Ogrodnik, M., et al. (2017). "Cellular senescence drives age-dependent hepatic

steatosis." Nature Communications 8(1): 1-12.

- Oishi, Y. and I. Manabe (2016). "Macrophages in age-related chronic inflammatory diseases." NPJ aging and mechanisms of disease 2(1): 1-8.
- Ouelle, D. E., et al. (1995). "Alternative reading frames of the ^{Ink4a} tumor suppressor gene encode two unrelated proteins capable of inducing cell cycle arrest." Cell 83(6): 993-1000.
- Paolillo, C., et al. (2019). "Single-cell genomics." Clinical Chemistry 65(8): 972-985.
- Papatheodoridi, A. M., et al. (2020). "The role of senescence in the development of nonalcoholic fatty liver disease and progression to nonalcoholic steatohepatitis." Hepatology 71(1): 363-374.
- Picelli, S. (2017). "Single-cell RNA-sequencing: the future of genome biology is now." RNA biology 14(5): 637-650.
- Pluquet, O., et al. (2015). "The unfolded protein response and cellular senescence. A review in the theme: cellular mechanisms of endoplasmic reticulum stress signaling in health and disease." American Journal of Physiology-Cell Physiology 308(6): C415-C425.
- Ransick, A., et al. (2019). "Single-cell profiling reveals sex, lineage, and regional diversity in the mouse kidney." Developmental cell 51(3): 399-413. e397.
- Rufini, A., et al. (2013). "Senescence and aging: the critical roles of p53." Oncogene

32(43): 5129-5143.

- Sasaki, M., et al. (2001). "Senescent cells are resistant to death despite low Bcl-2 level." Mechanisms of ageing and development **122**(15): 1695-1706.
- Scarff, K. L., et al. (2003). "A retained selection cassette increases reporter gene expression without affecting tissue distribution in SPI3 knockout/GFP knock-in mice." Genesis **36**(3): 149-157.
- Schmidt-Supprian, M., et al. (2007). "Excision of the Frt-flanked neo R cassette from the CD19cre knock-in transgene reduces Cre-mediated recombination." Transgenic research **16**(5): 657-660.
- Scholzen, T. and J. Gerdes (2000). "The Ki-67 protein: from the known and the unknown." Journal of cellular physiology **182**(3): 311-322.
- Sessions, G. A., et al. (2019). "Controlled induction and targeted elimination of p16^{Ink4a}-expressing chondrocytes in cartilage explant culture." The FASEB Journal **33**(11): 12364.
- Sharpless, N. E., et al. (2002). "p16^{Ink4a} and p53 deficiency cooperate in tumorigenesis." Cancer research **62**(10): 2761-2765.
- Sharpless, N. E. and C. J. Sherr (2015). "Forging a signature of *in vivo* senescence." Nature Reviews Cancer **15**(7): 397-408.
- Smith, J. R. and O. M. Pereira-Smith (1996). "Replicative senescence: implications

for *in vivo* aging and tumor suppression." Science **273**(5271): 63-67.

- Solana, R., et al. (2012). Innate immunosenescence: effect of aging on cells and receptors of the innate immune system in humans. Seminars in immunology, Elsevier.
- Stegle, O., et al. (2015). "Computational and analytical challenges in single-cell transcriptomics." Nature Reviews Genetics **16**(3): 133-145.
- Susaki, E. A., et al. (2014). "Whole-brain imaging with single-cell resolution using chemical cocktails and computational analysis." Cell **157**(3): 726-739.
- Tainaka, K., et al. (2018). "Chemical landscape for tissue clearing based on hydrophilic reagents." Cell Reports **24**(8): 2196-2210. e2199.
- Tchkonina, T., et al. (2010). "Fat tissue, aging, and cellular senescence." Aging Cell **9**(5): 667-684.
- Ueno, H. and I. L. Weissman (2006). "Clonal analysis of mouse development reveals a polyclonal origin for yolk sac blood islands." Developmental cell **11**(4): 519-533.
- Van Deursen, J. M. (2014). "The role of senescent cells in ageing." Nature **509**(7501): 439-446.
- Wang, X., et al. (2009). "The regulation of proximal tubular salt transport in hypertension: an update." Current opinion in nephrology and hypertension **18**(5):

412.

- Wolf, M. J., et al. (2014). "Metabolic activation of intrahepatic CD8+ T cells and NKT cells causes nonalcoholic steatohepatitis and liver cancer via cross-talk with hepatocytes." Cancer cell **26**(4): 549-564.
- Xiong, X., et al. (2019). "Landscape of intercellular crosstalk in healthy and NASH liver revealed by single-cell secretome gene analysis." Molecular Cell **75**(3): 644-660. e645.
- Xu, M., et al. (2018). "Senolytics improve physical function and increase lifespan in old age." Nature Medicine **24**(8): 1246-1256.
- Yamakoshi, K., et al. (2009). "Real-time *in vivo* imaging of p16^{Ink4a} reveals cross talk with p53." Journal of Cell Biology **186**(3): 393-407.
- Yosef, R., et al. (2016). Directed elimination of senescent cells by inhibition of BCL-W and BCL-XL. Nat Commun **7**: 11190.
- Yoshimoto, S., et al. (2013). "Obesity-induced gut microbial metabolite promotes liver cancer through senescence secretome." Nature **499**(7456): 97-101.

Acknowledgements

The thesis study was performed under the supervision of Prof. Makoto Nakanishi. I would like to express my sincere gratitude for his keen mentorship and considerable support, which made it possible for this study to be accomplished. I am deeply grateful to Dr. Yoshikazu Johmura and Dr. Teh-Wei Wang. Without their advice and valuable discussions, I could not have completed this research successfully. They also educated me to become a scientist and the chance to meet both of them was the most valuable part of my Ph.D. experience. I also thank Dr. Astuya Nishiyama for his helpful comments and meaningful discussion. I learned scientific thinking skills from him. I am grateful to the graduated and current students in the Nakanishi lab, especially Ms. Tomomi Kanai and Dr. Koji Nishikawa, who kindly and honestly helped with the experiments of this study. They also made my days enjoyable. I am indebted to Mrs. Miho Ishiura and Mrs. Tomoko Ando for making sections. They were willing to take on many tasks. I thank the almost 20 collaborators in the Institute of Medical Science and other universities. I am grateful to the members of Collins lab at Massachusetts Institute of Technology where I studied during my 3rd year Ph.D. and my friends in Boston for improving my English skill and supporting my life. Finally, I would like to thank my family for all their love, support, and encouragement.